Characterization of Fullerenes for Electrostatic Propulsion Applications

Thesis by

Stephanie D. Leifer

In Partial Fulfillment of the Requirements

for the Degree of

Doctor of Philosophy

California Institute of Technology

Pasadena, California

1995

(Defended May 26, 1995)

To Pete

Acknowledgments

The research described in this dissertation has been made possible by grants from the Air Force Office of Scientific Research, grant #F49620-92-J-0453, the California Institute of Technology President's Fund, and the Jet Propulsion Laboratory, California Institute of Technology, under contract with the National Aeronautics and Space Administration.

To my advisor, David Goodwin, I am very grateful. Despite the immense level of responsibility and amount of work undertaken by Dave, he still found time to be my advisor. Also appreciated are the efforts of Fred Culick who was a co-advisor for this research, and Robert Whetten who provided my first window into the world of fullerenes, and was a co-principal investigator on the Caltech grant.

Special thanks to John Anderson who spent many long hours in the lab working with both DC and RF C_{60} discharge chambers. John provided much needed reality checks through the course of these experiments as well as his own unique form of comic relief. Deep appreciation goes to John Brophy whose leadership in the Electric Propulsion Group at JPL and knowledge of ion propulsion is unsurpassed. Heartfelt appreciation especially goes to Winston Saunders whose bright and imaginative insights into applied technology helped to form the C_{60} ion thruster concept, and whose tutelage guided me through many aspects of the graduate program at Caltech. I owe a life-long debt of gratitude to Mark Anderson whose love of science and playful creativity have provided many hours of fruitful research and just plain fun.

Many other individuals have contributed significantly to this work. Santosh Srivastava, Gwo Jong, Jim Kulleck, Keith Goodfellow, Juergen Mueller, Dennis Fitzgerald, Raoul Perez, Warren Dowler, Gerry Voekes, Andre Yavrouian, Gary Plett, and Don Rapp all

played active roles in the research described here. Valuable technical support was provided by Bill Thogmartin, Al Owens, Bob Toomath, and Lew Pless. Carol Garland, Channing Ahn, Axel Scherer, and Reynold Johnson were a tremendous help by allowing me access to and guidance in their facilities. At some time or another, just about every member of the Goodwin group at Caltech and the Electric Propulsion Group at JPL has provided some assistance. I am deeply indebted to them all for their help.

My time at Caltech and JPL would not have been nearly so rewarding without the friendships of John Blandino, Bill Thogmartin, Juergen Mueller, Selmer Wong, and Tom Teilhet. They are always willing to lend a sympathetic ear, offer sage advice, or tell interesting stories. Per-Olov Peterson, besides being a wonderful friend, is a terrific classmate; we spent many occasions working out problem sets together, often into the wee hours of the morning.

Finally, I thank my family: Mom and Dad who are always supportive of my endeavors and instilled in me the discipline necessary to complete a task such as this one, and Joel, Cindy, Alex, and Christopher for welcoming me into their lives. Most of all, I thank my husband, Pete Sercel, whose love, infinite patience, understanding, good humor, and strength have been unwavering. To you, Pete, I dedicate this work. Thanks for waiting for me.

Abstract

C_{60}, also known as Buckminsterfullerene, possesses a remarkable resilience, high mass, and low ionization potential which indicate that it could make an excellent ion engine propellant. The development of an efficient, reliable C_{60} ion thruster for space flight requires a knowledge of many of the properties of this new molecule. The research described here focusses on the determination of some of these properties and their effects on the behavior of C_{60} in a plasma environment. Investigations of fullerene thermal stability, polarizability, electron-impact ionization and fragmentation phenomena, vibrational spectra, and plasma discharges are reported.

The electron-impact ionization and fragmentation experiments were conducted using a time-of-flight mass spectrometer. Ionization efficiency curves for the production of both C_{60}^{+} and C_{60}^{++} ions were obtained, and appearance potentials of 7.8 ± 0.5 eV and 16.4 ± 0.5 eV for C_{60}^{+} and C_{60}^{++}, respectively were identifed. Fullerene cracking patterns showed only even-numbered fragments, and only at electron energies above 70 eV. Multiply charged fullerene ions through C_{60}^{4+} were observed, revealing the remarkable resistance of C_{60} to coulomb explosion.

Experiments to determine the polarizability of C_{60} using a Mach-Zehnder interferometer and the Clausius-Mossotti relation were performed. The data yielded a polarizability value near 85×10^{-24} cm^3.

Although previous experiments performed by other researchers with filament cathode discharge chambers successfully demonstrated the production of C_{60} plasma at a minimum discharge voltage of 22 V, difficulty with severe erosion of the tungsten filament cathode was encountered. Also, decomposition of the fullerenes at temperatures above 1073 K was observed.

In light of these observations, the thermal stability of a fullerene mix was examined. Decay constants were obtained and used to find an Arrhenius plot for the thermal decomposition. The Arrhenius activation energy was found to be 265.6± 8.9 kJ/mol. The disintegration of C_{60} occurs at significantly lower temperatures than those predicted by molecular dynamics simulations. A mechanism for fullerene disintegration different than C_2 elimination, possibily involving ring-rearrangement in the fullerene cage, may be responsible.

Because the determination of the purity of fullerene samples is vital when investigating their degradation at elevated temperatures, a study of fullerene contaminants and adsorbates using Fourier Transform Infrared (FTIR) spectroscopy was conducted. For solid fullerene samples, Diffuse Reflectance Infrared Fourier Transform (DRIFT) spectroscopy was employed. Features in the 2350, 2330, and 1540 cm^{-1} region of the spectrum were found to be intrinisic to C_{60} and did not result from CO_2 or O_2 contamination. By increasing the CO_2 content of solid C_{60}, new features could be observed at 2377, 2330 and 2316 cm^{-1}. The peak observed at 1539 cm^{-1} in the solid vanished when fullerenes were placed in solution, but reappeared when the sample was dried under N_2. The strength of this peak may be due to a Fermi resonance or crystal field effect, both of which could be destroyed by solvent interactions in solution.

To avoid the presence of high temperature metal surfaces, a RF discharge chamber was constructed to maintain a fullerene plasma inductively, eliminating the presence of hot electrode surfaces. A xenon plasma was successfully generated in the thruster. The maximum extractable beam current was approximately 45 mA. Ion production cost for a pure xenon plasma was 1400 eV/ion. When C_{60} vapor was added to the xenon plasma, the discharge quenched when the ratio of C_{60} molecules to xenon atoms exceeded 1:16. A pure fullerene RF discharge could not be initiated.

The cause of this phenomenon can be found in the electron attachment cross section of C_{60}; this cross section is very large for electron energies up to 14 eV. It would be necessary to maintain an electron temperature of 10 eV or greater for positive fullerene ion production rates to exceed that of negative ion production rates.

In summary, this research has been an investigation of some fundamental properties of C_{60} relevant to fullerene ion thruster development. It was found that although fragmentation by electron impact of C_{60} does not pose a significant problem, the thermal stability of fullerenes is not as great as had been anticipated. As a result, use of conventional hollow cathode configurations in fullerene ion thrusters is precluded. A RF fullerene ion thruster configuration was pursued instead, but proved difficult to operate because electron attachment cross sections for C_{60} remain large up to 14 eV electron energy. Therefore, the use of other ionization mechanisms may prove more successful for fullerene ion thruster development, and should be pursued in future work.

Contents

List of Figures

List of Tables

Chapter 1

Introduction

1.1 Background and Motivation

In 1985, Harold Kroto, Jim Heath, Scott O'Brien, Robert Curl, and Richard Smalley performed an experiment [1] intended to elucidate the formation mechanism of long chain carbon molecules that may be formed in interstellar space, and to explore whether carbon clusters could be associated with diffuse interstellar bands. The experiment involved laser vaporization of carbon from a graphite disk into a helium flow. What the team from Rice University and the University of Sussex observed in their mass spectrometer surprised them — an anomolously high peak corresponding to clusters of 60 carbon atoms. Just one year prior, researchers at Exxon Corporation [2] had generated clusters of carbon atoms, C_n for values of n from 1 to 190, and also noted that clusters of 60 carbon atoms occurred most frequently for clusters composed of more than 40 atoms. However, the team from Rice and Sussex realized they had made a significant discovery because, by adjusting the vaporization conditions in their apparatus, they could make the C_{60} peak 40 times larger than any other peak in the mass spectrum. Shortly thereafter, Kroto *et al.* [1] suggested the now well-known structure of the C_{60} molecule. The molecule, named Buckminsterfullerene after the designer of the geodesic dome, R. Buckminster Fuller, consists of 60 carbon atoms arranged in a truncated icosahedron (see Figure 1.1). In addition to C_{60}, an entire family of hollow, even-numbered carbon molecules, called fullerenes, has been found. C_{70} is the next-most abundant of these.

Many researchers remained skeptical of the proposed highly symmetric structure of C_{60} until 1990 when Wolfgang Krätschmer, Lowell Lamb, Konstantinos Fostiropoulos and Donald Huffman announced that they had found a method of producing macroscopic quantities of C_{60} [4]. The technique was a surprisingly simple and elegant one; a carbon arc was formed between two graphite electrodes in a helium environment. A grey-white soot emanated from the arc region, and deposited on cool surfaces in the vacuum chamber. When mixed with a solvent such as toluene or benzene, some of the material in the soot dissolved, creating a magenta-colored solution. Amorphous and graphitic carbon, which are the primary constituents of the soot, are insoluble in these solvents; the dissolved material was fullerene. When formed under certain helium pressures, the soot contained as much as 15% fullerene. It was after the discovery of this production technique that the explosion in fullerene research began. Single-line nuclear magnetic resonance measurements [3] provided the final proof that all 60 carbon atom in the molecule were equivalent. In the five years since Krätschmer and Huffman's technique was announced, a completely new branch of chemistry has evolved. The number of articles about C_{60} and fullerene related topics that have appeared in refereed journals has grown to well over three thousand.

Huffman's technique also led to the discovery of hollow carbon tube-like structures which deposit on the negative carbon electrode. These helical carbon microtubules [5] are now popularly referred to as buckytubes, and have promising applications in many fields. Bucky-onions, or concentric spherical shells of carbon, have been observed as well [6].

C_{60} has been found to occur naturally. It has been identified in samples of a coal-like mineral called shungite found in Russia [7], and in specimens of a glassy rock called fulgurite which is formed from lightening strikes to the ground [8]. Fullerene deposites have been discovered in Sudbury crater in Canada [9], and in samples from New Zealand [10]. Both regions are the sites of meteor impacts. There have been claims that there is spectroscopic evidence for C_{60} in frozen gas matrices in diffuse interstellar material [11], and fullerenes have been found in the impact crater of a micrometeorite on the Long Duration Exposure Facility (LDEF) spacecraft [12].

When dried from solution, C_{60} is a powdered solid with a brown-black color. It forms a remarkably strong van der Waals solid — strong enough to form free standing films [3]. C_{60} crystals, called fullerite, possess a primarily face-centered-cubic (FCC) structure (see Figure 1.2), but coexist with a hexagonal-closest-packed (HCP) phase which can comprise roughly 20% of the solid. The HCP phase readily converts to FCC by thermal annealing. Pure C_{70}, on the otherhand, is most stable as an HCP solid. The density of solid C_{60} is 1.7 g/cc [14]. In both solid and solution, C_{70} has a deep red appearance. C_{60} appears yellow as a film, but looks purple in solution. The diameter of the C_{60} cage is 7.1 Å, but has a van der Waals diameter of 10.04 Å[14]. In the solid, fullerene molecules rapidly rotate in their positions in the lattice. At 250 K, C_{60} undergoes an orientational order/disorder phase transition [15] in which the rotations are frozen; the crystal structure then converts to simple cubic. The order/disorder transition temperature is dependent upon the level of

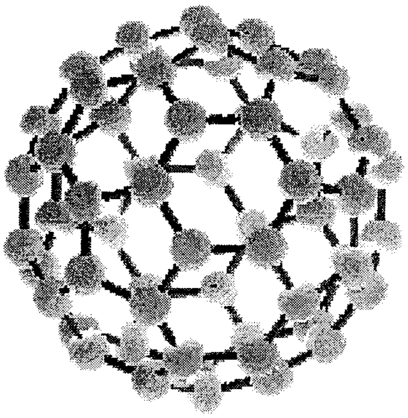

Figure 1.1: C_{60}:Buckminsterfullerene

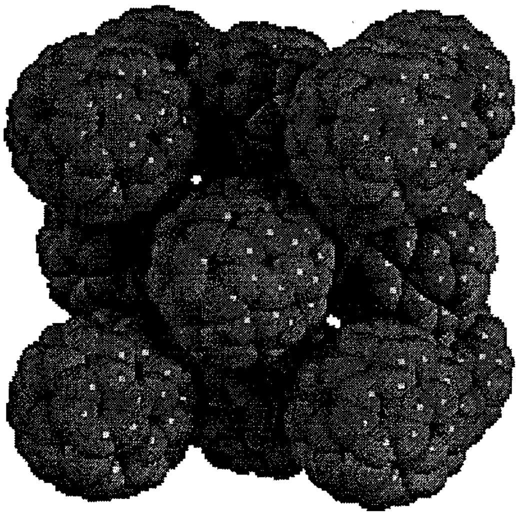

Figure 1.2: C_{60} molecules arranged in a face-centered-cubic lattice.

impurities present at the octahedral and tetrahedral voids of the crystal lattice, which may serve to anchor the molecules and promote a ratchet-type motion.

Unlike other carbon allotropes, fullerenes sublimate at relatively low temperatures, making them useful for applications that require a gas-phase carbonaceous material. The vapor pressure of C_{60} at 800 K is approximately 2 mTorr, and its heat of sublimation, ΔH_s, is 7.9 kJ/mol [16].

Fullerenes are soluble in chemicals similar to it [20]; it is highly soluble in naphthalenes, moderately soluble in benzenes and haloalkanes, and virtually insoluble in polar solvents. In general, C_{60} solubility increases with the number of carbon atoms in the solvent molecules.

The remarkable properties demonstrated by fullerenes and other carbon nanostructures have enticed researchers to find applications which would be enabled or improved by their use. A partial list of suggestions for applications include nanoscale electronic devices, high strength materials components [18], non-linear optical materials [19], and pharmaceutical uses [20,21]. In 1991 it was found that alkali-metal-doped C_{60} is a superconductor. The highest superconducting transition temperature found thus far is 42.5 K for $Rb_{2.7}Tl_{2.2}C_{60}$ [14]. Fullerenes have also been considered for use as a molecular sieve material [22]. One possible use suggested for C_{60}, and the theme of this work, is as the propellant for electrostatic ion engines [23].

Electrostatic ion engines have been developed since the 1960's for space propulsion. Thrusters have been operated with mercury, cesium, and noble gas propellants, though testing of the liquid metal thrusters was abandoned due to concerns over spacecraft contamination and toxicity issues associated with ground-based tests. Xenon has since become the propellant of choice for ion thrusters. Current plans to use xenon ion thrusters are underway at Hughes Space and Communications with their 13 cm Xenon Ion Propulsion Subsystem (XIPS) thruster, and at NASA with a 30 cm xenon ion thruster for the NASA Solar-Electric-Propulsion Technology Applications Readiness (NSTAR) mission.

Ion thrusters operate by ionizing a propellant gas and accelerating the resulting positive ions electrostatically to produce thrust. The expelled ion beam is injected with electrons to maintain charge neutrality of the spacecraft and to prevent large beam divergence due to coulomb repulsion in the exhaust.

Developers of ion propulsion for space flight have long sought a high mass propellant molecule or cluster that will not fragment when ionized. Use of a heavy propellant in an electric thruster results in higher efficiency at moderate specific impulse and allows higher achievable thrust and power handling capabilty.

With propellants of light ion mass, high thruster power efficiencies are achieved only when large potential differences are applied to the thruster extraction grids. The large potential differences result in high propellant exhaust velocities. However, there are applications of electric propulsion, such as orbit transfer missions and North-South station keeping for geosynchronous satellites, in which it is desirable to operate at a low-to-moderate specific impulse (1000 to 2000 lbf-s/lbm). In this range, electric thrusters utilizing conventional propellants such as xenon become less efficient. Figure 1.3 shows the efficiency of several electric propulsion devices as a function of specific impulse. Arcjet efficiency decreases with increasing specific impulse, while xenon ion thrusters require high exhaust velocities for efficient performance. The Russian-built Stationary Plasma Thruster (SPT) delivers the highest performance in the 1500 lbf-s/lbm specific impulse regime [25], yet is only on the order of 50% efficient.

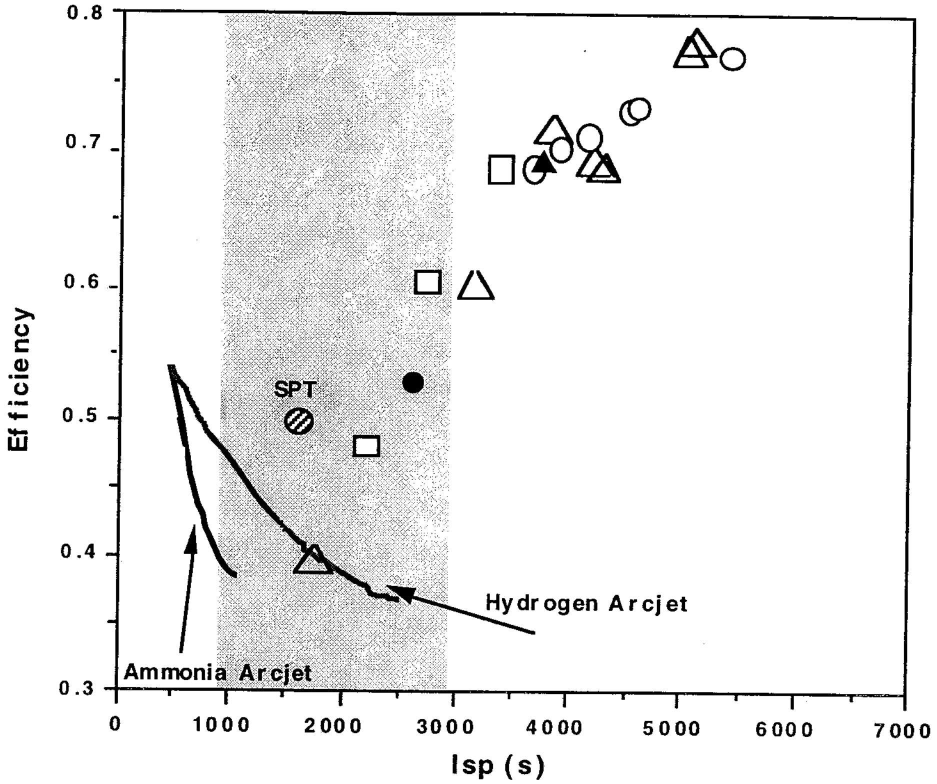

Figure 1.3: Efficiencies of xenon ion engine, hydrogen and ammonia arcjets, and Stationary Plasma Thruster (SPT) as a function of specific impulse. Data are experimental [25]-[28]. Arcjet efficiency decreases with increasing specific impulse, while xenon ion thrusters require high exhaust velocities for efficient performance. The Russian-built SPT delivers the highest performance in the 1500 lbf-s/lbm specific impulse regime, yet is only on the order of 50% efficient.

State-of-the-art ion propulsion is also limited to relatively low thrust levels. This limitation results from the fact that thrusters operating with low molecular weight propellants require high beam currents to achieve high thrust. To achieve high beam currents, a large thruster aspect ratio (ratio of accelerator grid diameter to spacing between grids) is required. The use of heavy propellants allows for a smaller engine diameter at a given specific power, thrust, and exhaust velocity [29]. This is a vital property of heavy ion propulsion because present ion thrusters have been limited in achievable aspect ratios.

Since early in ion thruster development, researchers have investigated the production of clusters bound by van der Waals forces in an effort to obtain heavy ion propellants [30]. There are several different methods for producing these clusters, one of which is condensation from the gas phase resulting from expansion through a supersonic nozzle. The possibility of using such a system as a propellant source in an electric thruster was pursued because the resulting clusters were expected to have the desired high mass. However, the performance of a cluster ion engine ultimately depends on the clustering efficiency of the atoms, and the production of clusters having a narrow charge-to-mass ratio distribution. Early attempts at developing cluster ion engines met with difficulty in achieving high (greater than 70% [31]) clustering efficiency and narrow cluster mass distributions. In addition, van der Waals clusters are fragile (the binding energies per atom are tenths of an electron-volt), making them susceptible to fragmentation during ionization [32]. Various molecular propellants were also considered. A discussion of possible molecular ion propellants is given by Dugan [33] who concludes that aromatic organic molecules offer the most promise. His treatment of the topic focusses on the risk of fragmentation due to ionization, excitation, and thermal decomposition of the molecules.

C_{60} possesses a remarkable resilience, high mass, and low ionization potential that indicate it could make an excellent ion thruster propellant. It has an ionization potential of 7.6 eV [34], compared to 12.1 eV for xenon. A C_{60} molecule is also 5.5 times heavier than a xenon atom, and has a cross section for ionization by electron impact that is larger by an order of magnitude. C_{60} has proven to be resistant to collisionally-induced fragmentation. When it does dissociate, fragmentation proceeds through successive losses of C_2 groups [4].

Ion thrusters operating with C_{60} would be important for satellite station keeping, orbit transfer, or long duration robotic exploration missions. The higher efficiency at moderate specific impulse can result in either longer mission life or increased available payload.

Characteristics of several different ion thruster propellants are shown in Table 1.1. Listed are the propellant atomic or molecular mass, the first ionization potential, the cross section for ionization at 40 eV electron energy, the ion production cost in eV/amu, and the thruster efficiency at a fixed exhaust velocity. The thruster data are experimental and are taken from tests of electron bombardment ion engines [26]-[28]. Data for light propellants (argon and krypton) are unavailable below the specific impulse shown.

Because the properties of C_{60} appear so promising for ion propulsion applications, it is possible that C_{60} ion thrusters could fill the gap in high efficiency propulsion capability in the 1000-2000 s specific impulse range.

1.2 The Present Study

The development of an efficient, reliable ion thruster which utilizes a fullerene propellant requires knowledge of many of the properties of these new molecules. At the time this research began, very little was known about C_{60}. The studies reported here were conducted

Propellant	Mass (amu)	I.P. (eV)	σ^+(40 eV) (cm^2)	Ion Cost eV/amu	I_{sp} (s)	Efficiency (%)	Ref.
Xenon	131.3	12.13	5.1×10^{-16}	1.22	2585	51.3	[28]
Krypton	83.8	13.99	4.0×10^{-16}	.38	4280	67.9	[36]
Argon	40.0	15.76	2.7×10^{-16}	.81	4680	50.8	[36]
Mercury	200.6	10.44	5.5×10^{-16}	.72	2430	69.4	[36]
C_{60}	720.0	7.61 [34]	54×10^{-16}	—	—	—	—

Table 1.1: Properties of Ion Thruster Propellants. The ionization potential is labeled I.P., and the references refer to the ion cost, specific impulse (I_{sp}), and efficiency. The values for noble gas ionization cross section are from Reference [24].

to determine some of these properties and to assess their effect on the fundamental feasibility of the C_{60} ion thruster concept. The experiments fall into several distinct categories: time-of-flight mass spectrometry, Fourier transform infrared spectroscopy, thermal stability, polarizability, and discharge chamber experiments.

The time-of-flight mass spectrometer was used to determine fragmentation patterns of C_{60}, and to measure its ionization cross section by electron impact. Such properties are necessary for predicting C_{60} ion thruster performance. As the research progressed, it became evident that the thermal stability of fullerenes had not been adequately investigated. It was not even known whether C_{60} has a liquid phase, though one was theoretically predicted to exist at 1700 K [37,38]. Thermal stability of fullerenes is vital for ion propulsion applications because of the high operating temperatures attained by some thruster components.

Fourier transform infrared spectroscopy was used for an investigation of the infrared spectrum of C_{60}. These investigations have enabled the observation of interesting behavior of some C_{60} combination modes, and rule out the possibility that these peaks result from carbon dioxide contamination as had been reported elsewhere in the literature. These findings also support observations of fullerene thermal stability, indicating that C_{60} decomposition is unimolecular, and not a stoichiometric or catalytic reaction with impurities.

The discharge chamber experiments were carried out with both DC and RF ion thruster configurations. The goals of this work were to demonstrate fullerene sublimation, ionization, and acceleration with minimal fragmentation of the molecules, and to identify other potential feasibility issues of the C_{60} ion thruster concept.

1.3 Outline of This Report

The next chapter details fullerene ion thruster performance projections based on a model for electron-bombardment ion thrusters developed by Brophy [39]. The potential impact of C_{60} fragmentation and multiple ionization is investigated. Chapter 3 explores the thermal stability of C_{60} and reports an activation energy for thermal disintegration of C_{60}. Studies of the infrared spectrum of fullerenes in both the solid state and solution is reported in Chapter 4.

Chapter 5 is an account of investigations of fullerene ionization and fragmentation by electron impact. A description of the experimental apparatus is provided along with the experimental results. The findings were compared with values for ionization cross section derived from an additivity rule and correlation with molecular polarizability.

The instability of fullerenes at high temperature precludes their use with a conventional hollow cathode ion thruster. As a result, the use of an RF fullerene ion source is explored in Chapter 6. The RF plasma experiments were conducted with a mixture of fullerene vapor and xenon. An explanation of how negative ion formation affects thruster operation is given. In the first part of this chapter, the results of experiments which use DC fullerene discharge devices are described.

Detailed experimental data from the thermal stability investigation is provided in Appendix A. Appendix B contains data on the infrared spectrum of C_{60}. The polarizability experiment detailed in Appendix C was conducted with the use of a Mach-Zehnder interferometer and the Clausius-Mossotti relation.

References

[1] H. Kroto, J. Heath, S. O'Brien, R. Curl, And R. Smalley, "C_{60}: Buckminsterfullerene," *Nature* **318**, 162 (1985).

[2] E.A. Rohlfing, D.M. Cox, and A. Kaldor, "Production and Characterization of Supersonic Carbon Cluster Beams," *Journal of Chemical Physics* **81(7)**, 3322 (1984).

[3] R. Taylor, J. Hare, A. Abdul-Sada, and H. Kroto, "Isolation, Separation and Characterization of the Fullerenes C_{60} and C_{70} – the 3rd Form of Carbon," *Journal of the Chemical Society Chemical Communications* **20** 1423, (1990).

[4] W. Krätschmer, L. Lamb, K. Fostiropoulos, and D. Huffman, "Solid C_{60}: a New Form of Carbon," *Nature* **347**, 354 (1990).

[5] S. Iijima, "Helical Microtubules of Graphitic Carbon," *Nature* **354**, 56 (1991).

[6] D. Ugarte, "Curling and Closure of Gaphitic Networks Under Electron Beam Irradiation," *Nature* **359**, 707 (1992).

[7] P. Buseck, S. Tsipursky, and R. Hettich,"Fullerenes from the Geological Environment," *Science* **257(5067)**, 215 (1992).

[8] T. Daly, P. Buseck, P. Williams, and C. Lewis, "Fullerenes from a Fulgurite," *Science* **259(5101)**, 1599 (1993).

[9] L. Becker, J. Bada, R. Winans, J. Hunt, and T. Bunch, "Fullerenes in the 1.85-Billion-Year-Old Sudbury Impact Structure," *Science* **265(5172)**, 642 (1994).

[10] D. Heymann, L. Chibante, R. Brooks, W. Wolbach, and R. Smalley, "Fullerenes in the Cretacious-Tertiary Boundary-Layer," *Science* **265**, 645 (1994).

[11] B. Foing, P. Ehrenfreund, "Detection of 2 Interstellar Absorption-Bands Coincident With Spectral Features of C_{60}^{+}," *Nature* **369**, 296 (1994).

[12] F. Brozolo, T. Bunch, R. Fleming, and J. Macklin, "Fullerenes in an Impact Crater on the LDEF Spacecraft," *Nature* **369**, 37 (1994).

[13] A. Hebard, L. Trimble, G. Celler, and R. Haddon, "Fabrication and Properties of Freestanding C_{60} Membranes," *Science* **259(5103)**, 1887 (1993).

[14] D. Huffman, "Solid C_{60}," *Physics Today*, 22 November (1991).

[15] P. Heiney, J. Fischer, A. McGhie, W. Romanow, A. Denenstein, J. McCauley, and A. Smith, "Orientational Ordering Transition in Solid C_{60}," *Physical Review Letters* **66(22)**, 2911 (1991).

[16] A. Tokmakoff, D.R. Haynes, S.M. George, "Desorption Kinetics of C_{60} Multilayers from Al_2O_3(0001)," *Chemical Physics Letters* **186(4,5)**, 450 (1991).

[17] R. Ruoff, D. Tse, R. Malhotra, D. Lorents, "Solubility of C_{60} in a Variety of Solvents," *Journal of Physical Chemistry* **97**, 3379 (1993).

[18] E. Barrera, J. Simms, D. Callahan, V. Provenzano, J. Milliken, and R. Holtz, "Processing of Fullerene-Reinforced Composites," *Journal of Materials Research* **9(10)**, 2662 (1994).

[19] L. Tutt and A. Kost, " Optical Limiting Performance of C_{60} and C_{70} Solutions," *Nature* **356**, 225 (1992).

[20] S. Friedman, D. Decamp, and R. Sijbesma, "Inhibition of the HIV-1 Protease by Fullerene Derivatives – Model-Building Studies and Experimental Verification," *Journal of the American Chemical Society* **115**, 6506 (1993).

[21] R. Sijbesma, G. Srdanov, and F. Wudl, "Synthesis of a Fullerene Derivative for the Inhibition of HIV Enzymes," *Journal of the American Chemical Society* **115**, 6510 (1993).

[22] I.M.K. Ismail and S.L. Rodgers, "Comparison Between Fullerene and Forms of Well-Known Carbon," *Carbon* **30(2)**, 229 (1992).

[23] S.D. Leifer, D. Rapp, and W.A. Saunders, "Electrostatic Propulsion Using C_{60} Molecules," *AIAA Journal of Propulsion and Power* **8(6)**, 1297 (1992).

[24] D. Rapp and P. Englander-Golden, "Total Cross Sections for Ionization and Attachment in Gases by Electron Impact," *Journal of Chemical Physics* **43(5)**, 1464 (1965).

[25] J. Brophy, "Stationary Plasma Thruster Evaluation in Russia," JPL Publication **92-4**, (1992).

[26] V. Rawlin, "Performance of a Large Area Xenon Ion Thruster for Orbit Transfer Missions," NASA **TM102049**, (1989).

[27] M.J. Patterson, T.R. Verhey, "5kW Xenon Ion Thruster Lifetest," **AIAA 90-2543** Orlando, Florida, July (1990).

[28] J.R. Beattie, R.R. Robson, and J.D. Williams, "18-mN Xenon Ion Propulsion Subsystem," *AIDAA/AIAA/DGLR/JSASS 22nd International Electric Propulsion Conference* **IEPC-91-010**, Viareggio, Italy, October (1991).

[29] E. Stuhlinger, "Ion Propulsion for Space Flight," McGraw-Hill, New York, 248 (1964).

[30] C. Norgren, "Progress in Aeronautics and Astronautics," *Electric Propulsion Development*, Academic Press, 407 (1963)

[31] D. Goldin and G. Kvitek, "An Analysis of Particle Formation Efficiency in a Colloid Thruster," NASA **TM X-52172**, (1966).

[32] R. Jahn, "Physics of Electric Propulsion," McGraw-Hill, New York, 188 (1968).

[33] J. Dugan, "Some Theoretical Basis for the Selection of Molecular Ion Propellants and a Survey of Molecular Plasma Collision Processes," NASA **TM D-1185**, (1964).

[34] J. Zimmerman, J. Eyler, S. Bach, and S. McElvany, "Magic Number Carbon Clusters: Ionization Potentials and Selective Reactivity," *Journal of Chemical Physics* **94(5)**, 3556 (1991).

[35] S. O'Brien, J. Heath, R. Curl, and R. Smalley, "Photophysics of Buckminsterfullerene and Other Carbon Cluster Ions," *Journal of Chemical Physics* **88**, 220 (1988).

[36] V. Rawlin, "Operation of the J-Series Thruster Using Inert Gas," NASA **TM-82977**, (1982).

[37] A. Cheng, M. Klein, C. Caccamo, "Prediction of the Phase-Diagram of Rigid C_{60} Molecules," *Physical Review Letters* **71(8)**, 1200 (1993).

[38] M. Hagen, E. Meijer, G. Mooij, D. Frenkel, H. Lekkerkerker,"Does C_{60} Have a Liquid Phase," *Nature* **365(6445)**, 425 (1993).

[39] J. Brophy, "Ion Thruster Performance Model," NASA **CR-174810**, (1984).

Chapter 2

Performance Projections

The ideal propellant for ion propulsion has a high molecular mass, a low ionization potential, and a large ionization cross section. In the following pages, it is shown how these properties help to maximize the efficiency of an ion thruster, and enable thruster operation at thrust and power levels which are prohibitively high for noble gas ion propulsion.

Two predictions of fullerene ion thruster performance have been published [1,2]. Both of these works model a hollow cathode electron bombardment ion thruster for calculation of thruster efficiency.

2.1 Thruster Efficiency

A simple electron bombardment ion engine consists of a cathode for the production of electrons, a discharge chamber where the propellant gas is ionized, an anode, a screen grid, and an accelerator grid. A propellant gas is introduced to the discharge chamber. A magnetic field, which constrains electrons to move in cyclotron orbits, is applied to the discharge chamber by the presence of either permanent magnets or a solenoid. Electrons

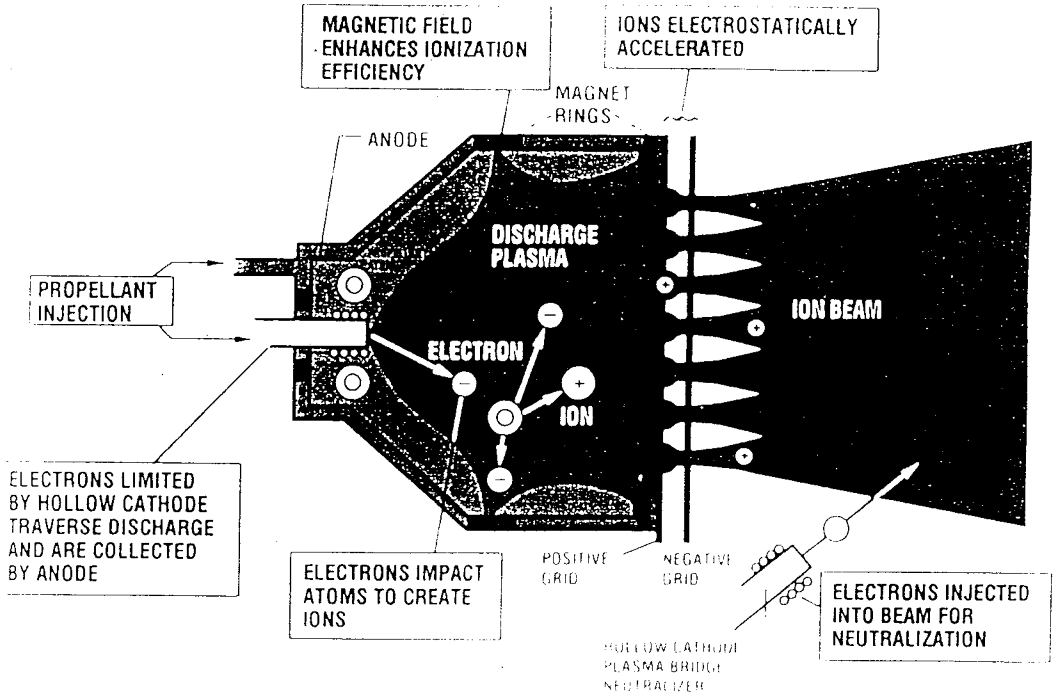

Figure 2.1: Diagram of an electron bombardment ion thruster.

emitted by the cathode are accelerated toward the anode which is held at a potential above that of the cathode. The electrons undergo ionizing collisions with the propellant molecules in the discharge chamber. The presence of the magnetic field increases the residence time of the electrons in the discharge chamber, increasing the probability that an ionizing collision will occur. Ions from the discharge chamber plasma are accelerated through the potential between the screen and accelerator grids, thereby producing thrust. Figure 2.1 shows a schematic diagram of an electron-bombardment ion thruster. The total efficiency of an ion thruster (product of the propellant utilization efficiency and power efficiency) may be approximated with the equation

$$\eta_t = \frac{\gamma^2 \eta_u}{1 + \frac{2e}{m_i}\left(\frac{\gamma \eta_u}{g I_{sp}}\right)^2 (\varepsilon_b + V_{nc})} \tag{2.1}$$

where γ is a thrust loss factor due to beam divergence and double ionization, η_u is the propellant utilization efficiency, m_i is the ion mass, I_{sp} is the specific impulse, e is the electron charge, g is the acceleration due to gravity at sea level, V_{nc} is the neutralizer coupling voltage, and ε_b is the ion production cost.

There are many mechanisms for energy loss involved in ion engine operation. These loss mechanisms include recombination of ions and electrons at the discharge chamber walls, creation and acceleration of electrons from the cathode, propellant ionization, excitation of the propellant molecules or atoms, neutralization of the exhausted ion beam, and acceleration of ions from the thruster. All of these mechanisms, except for the last two, contribute energy loss terms which can be summed together in an expression for the energy needed to create the ions which are expelled from the thruster. This energy is called the ion production cost (ε_b) and is expressed in units of eV/ion. The ion production cost is an important figure of merit because energy which is used to create ions can not be recovered. Hence, it plays an important role in determining the efficiency of an electric propulsion system.

However, from inspection, one can see that a principal driver of the efficiency at low specific impulse is the ion mass. Therefore, even if ε_b did not vary for different propellants, a higher mass propellant would still yield performance at higher efficiency.

Typical values for η_u, γ, and V_{nc} can be found in the literature (for example, References [3,4]), and are typically 0.8 - 0.9, 0.95, and 10 - 20 volts, respectively. The mass ratio of C_{60} to xenon, the current propellant of choice for ion propulsion, is approximately 5.5. If ε_b were the same for both C_{60} and xenon, a significant improvement in efficiency at low specific impulse (over a 28% increase at 1500 s, $\eta_u = 0.9$ and $(\varepsilon_b + V_{nc})$=200 V) would result from the use of C_{60}.

However, ε_b does vary for different propellants. This quantity will now be estimated for C_{60} and xenon so that more refined comparisons of efficiency can be made. The ion production cost may be found by using the expression derived by Brophy [5]

$$\varepsilon_b = \frac{\varepsilon_p^*}{f_b[1 - \exp(-C_0 \dot{m}(1-\eta_u))]} + \frac{f_c V_D}{f_b}. \tag{2.2}$$

The second term on the right-hand side of Equation 2.2 is only a few eV, and therefore is small compared to the first term. The factor ε_p^* is called the baseline plasma ion energy cost [5]. It is dependent on the average plasma ion energy cost due ionization and excitation of C_{60}, ε_0, and the average energy of the Maxwellian electrons leaving the plasma at the anode, ε_M. It is also a function of V_C, the plasma potential from which electrons emitted at the cathode are accelerated, and V_D, the discharge voltage. The relationship is

$$\varepsilon_p^* = \frac{\varepsilon_0 + \varepsilon_M}{1 - \frac{V_C + \varepsilon_M}{V_D}}. \tag{2.3}$$

Because some of the inelastic collision cross sections of C_{60} are unknown, an estimate of ε_p^* will not be attempted. Qualitatively, ε_p^* is expected to be lower for C_{60} than for xenon because the ionization potential of C_{60} is lower than xenon, and therefore the discharge voltage for C_{60} need not be as high. For xenon, ε_p^* is typically about 50 eV/ion.

C_0, the primary electron utilization factor, represents the efficiency with which primary electrons undergo inelastic collisions with propellant molecules. It is a function of the total inelastic collision cross section σ_{in}, the molecular mass m_i, the neutral particle velocity v, the area through which the beam is extracted $A_g\phi_o$, and the discharge voltage which affects the value of the cross section by determining the primary electron energy:

$$C_0 = \frac{4\sigma_{in} l_e}{v A_g \phi_o m_i}. \tag{2.4}$$

In this expression, l_e is the average distance a primary electron travels before reaching the anode. Large values of C_0 are desirable because they indicate more efficient ion production.

If one assumes that the ratio of σ_{in} of C_{60} to σ_{in} of xenon is proportional to the ratio of their ionization cross sections, then a value of the ionization cross section of C_{60} provides a means for comparing C_0 for the two propellants. When the ionization cross section of 54.5×10^{-20} m^2 at 41.3 eV is used (see Chapter 5), σ_{in} of C_{60} is found to be approximately 10.7 times that of xenon (where a value of 5.1×10^{-20} m^2 was used for the ionization cross section of xenon [6]). Also, the velocity of C_{60} neutrals will be inversely proportional to the square root of the molecular mass, m:

$$v = \sqrt{\frac{8k_BT}{\pi m}}, \tag{2.5}$$

where k_B is Boltzmann's constant and T is the temperature. The ratio of the neutral particle velocity of C_{60} molecules to that of xenon atoms is 0.43. Hence, the primary electron utilization factor of C_{60} is expected to be about 4.6 times that of xenon for the same thruster conditions.

Using typical values of the above variables for xenon of $\dot{m}$= 1.36×10^{-6} kg/s, $f_b = 0.6$, $f_c = 0.1$, $V_D = 30$ V, $C_0 = 3.68\times10^6$ (kg/s)$^{-1}$, and $\varepsilon_p^* = 50$ eV, the energy cost per xenon beam ion is found to be 217 eV for a propellant utilization efficiency of 0.9. If the energy cost per C_{60} ion is estimated by using the primary electron utilization factor calculated above, a cost of 98 eV for the same propellant utilization efficiency and flow rate is found. After dividing the energy cost per ion by the ion masses, the energy cost per atomic mass unit (amu) for C_{60} molecules is found to be only 8.2 percent of that required for xenon.

For a xenon ion engine operating at 1500 s and an ion production cost of 217 eV per ion, the efficiency would be approximately 37.7 percent (assuming values of g = 0.95, $\eta_u = 0.9$,

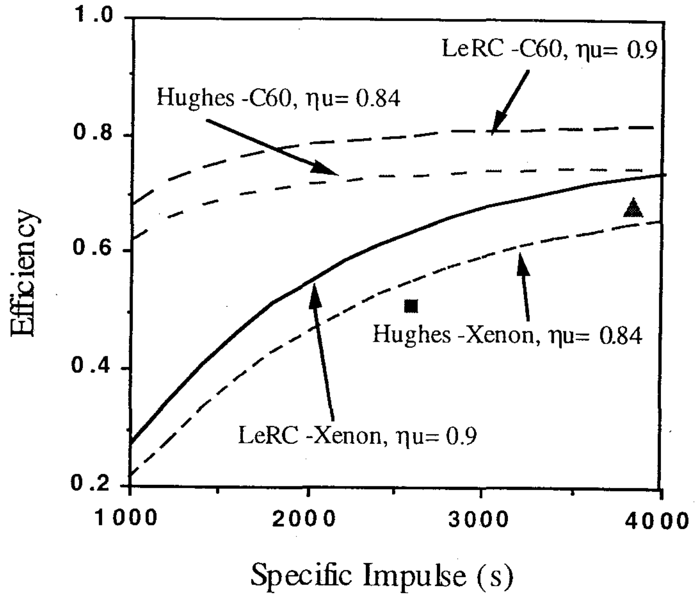

Figure 2.2: Efficiency as a function of specific impulse calculated for xenon and C_{60} ion thrusters. Data points are experimental [3,4].

and $V_{nc} = 15$, and using Equation 2.1). However, because of the higher accelerating voltage and lower ion production cost, a C_{60} ion engine has a calculated efficiency of about 73.7 percent at the same specific impulse of 1500 s. Thus, the potential improvement in efficiency at low specific impulse is evident. For comparison with experimental data, Table 2.1 shows the average performance of a 5 kW xenon ion thruster tested at NASA Lewis Research Center [3] and the Xenon Ion Propulsion (XIPS) subsystem [4] developed at Hughes Research Center. The values of C_0 were calculated from the measured ion production cost and used to make performance estimates for a comparable C_{60} thruster under the identical operating conditions. The experimental points, along with curves generated from the above equations, have been plotted in Figure 2.2. In the above calculations, the thermal energy required for the sublimation of C_{60} molecules has been neglected. The heat of sublimation of C_{60}

	η_t	ε_b^a eV/ion	Isp s	V_D V	η_u	T N	g	$\dot{m}$ kg/s $\times 10^{-6}$	C_0^b $(\text{kg/s})^{-1} \times 10^6$
XIPS actual	.51	240	2585	30.0	.84	0.0178	.95[c]	.654	2.3
XIPS theory	.55[d]								
C_{60} XIPS theory	.74	105							17.1
LeRC actual	.68	158	3840	26.9	.90	0.20	.96	4.65	1.68
LeRC theory	.73[e]								
C_{60} LeRC theory	.82	88							12.6

[a] f_c=0.1, f_b=0.6ε_p^*=50 eV for all

[b] xenon values calculated using actual ion production cost

[c] assumed

[d] assumed V_{nc}=15.0 V

[e] V_{nc}=15.4 V

Table 2.1: Performance of xenon ion thrusters and calculated performance of comparable C_{60} thrusters.

has been found to be just $(2.4 \pm 0.07) \times 10^{-3}$ eV/amu from a polycrystalline mixture of C_{60} and C_{70} [7], and $(2.0 \pm 0.05) \times 10^{-3}$ eV/amu from multilayers of pure C_{60} [31]. However, an upper limit to the amount of thermal energy the C_{60} molecules may contain can be found from

$$E_T = (3n - 6) k_B T, \tag{2.6}$$

where E_T is the thermal energy and n is the number of atoms in the molecule. For C_{60} molecules at a sublimation temperature of 873 K, this energy would be 13.1 eV, or about 13.6% of the total energy cost per C_{60} ion.

It is possible that the thruster will have to be maintained at a high temperature to prevent condensation of C_{60} on thruster surfaces. Radiation from these surfaces may be a loss mechanism of importance if the thruster is operated at low power levels. A 13 cm, 500 W xenon ion thruster typically operates with a wall temperature of approximately 550 K. At this temperature, if only radiation through the grids is considered, approximately 35 W (or 7% of the power) will be radiated away. At the same power level, a thruster operating at 850 K would lose over 190 W (38%). However, at high power levels (several kW regime), the thermal loss becomes insignificant.

2.2 Thrust and Power Level

It can be shown that the total thrust *density* attainable by an ion thruster is a function only of the electric field maintained between the grid optics. Beginning with the relation for the thrust-per-unit-area, T/A in terms of the Child's law limited current density, i

$$\frac{T}{A} = \frac{im}{q} c, \tag{2.7}$$

where m is the particle mass, q is the charge, and c is the exhaust velocity. Substituting the expressions for i and c yields

$$\frac{T}{A} = \frac{4}{9}\varepsilon_0 \frac{V^{3/2}}{s^2}\sqrt{\frac{2q}{m}}\frac{m}{q}\sqrt{\frac{2qV}{m}}, \tag{2.8}$$

where V is the accelerating potential, s is the gap between the grids, and ε_0 is the permittivity of free space. By simplifying Equation 2.8, it is found that

$$T = \frac{8\varepsilon_0}{9}E^2. \tag{2.9}$$

Here, E is the electric field. However, the use of heavy ion propellants does allow for thruster operation at high thrust and power levels. This can be demonstrated by considering an ion thruster operating at a specific impulse of 7500 s. The thrust may be expressed in terms of the specific impulse and the span-to-gap ratio:

$$T = \frac{\pi\varepsilon_0}{18}R^2\frac{m_i}{e}^2(gI_{sp})^4. \tag{2.10}$$

For a span-to-gap ratio of 114 and an electric field of 2.3×10^6 V/m, a C_{60} engine would have a thrust of about 32.7 N with an engine diameter of 1.0 m and an accelerating potential of 20.18 kV. To obtain the same total thrust from a xenon ion thruster, the span-to-gap ratio would have to be increased to 627 (accelerating potential = 3.67 kV). This high span-to-gap ratio is the limiting factor in the operation of light ion thrusters at high thrust levels, as state-of-the-art ion thrusters have values of R which do not greatly exceed 500.

Though it may seem that larger propellant mass results in improved engine efficiency and greater thrust and power handling capability, it is necessary to understand why extremely large particulates are not used as propellants. Primarily, this is because excessively high voltages would be required for ion acceleration. Such high voltages may result in corona discharges and arcing between thruster components.

2.3 The Effect of Double Ionization and Fragmentation on Ion Thruster Performance

Multiply-charged and fragment ion formation pose a problem for ion thruster operation regardless of propellant choice. An investigation of the impact of these two processes in C_{60} ion thrusters is reported in Reference [9]. Below, the origin of reduced ion thruster performance resulting from a non-uniform charge-to-mass distribution of propellant particles is explored.

2.3.1 Double Ionization

A propellant with a high second ionization potential is desirable for ion thruster operation in order to limit the number of double ions produced in the plasma. In xenon ion thrusters, double ions typically constitute no more than 10% of the total ion density in the thruster. The second ionization potential for xenon is 21.2 eV; this appearance potential is only a few volts below the discharge voltage of most electron bombardment ion thrusters. For Buckminsterfullerene, the second ionization potential by electron impact ionization is approximately 16.4 eV (see Chapter 5).

The effect of double ion formation on total thruster efficiency may be examined by considering two cases: one in which a thruster expells only singly-charged ions, and one in which it expells some fraction f_1 of singly-charged and $f_2 = 1 - f_1$ of doubly-charged ions. To compare the thrusters under equivalent conditions, the two systems are restricted to operate with the same total mass flow rate, the same specific impulse (average exit velocity), and therefore, the same thrust. The difference between the two systems will clearly be the accelerating voltage. The ion velocities for the two cases are related by,

$$v_1 = (f_1 + \sqrt{2} f_2) v_2. \tag{2.11}$$

The power efficiency, η_{pw}, is defined to be the ratio of the power required to accelerate only single ions to the power necessary to accelerate single and double ions to the same average exhaust velocity:

$$\eta_{pw} = \frac{P_1}{P_2} = \frac{v_1^2}{(f_1 + 2f_2)v_2^2} = \frac{\kappa^2}{k}, \tag{2.12}$$

where $\kappa = (f_1 + \sqrt{2} f_2)$, and $k = (f_1 + 2f_2)$. The total thruster efficiency is the product of the power efficency found in Equation 2.12, the propellant utilization efficiency, and the electrical efficiency of the thruster, which is dependent upon the energy required to produce, accelerate, and neutralize the ions. The latter is

$$\eta_{ac} = \frac{\gamma^2 (V_+)_2 \sum_{i=1}^{2} f_i q_i}{[(V_+)_2 + (V_{nc})_2] \sum_{i=1}^{2} f_i q_i + \sum_{i=1}^{2} f_i \varepsilon_{bi}}. \tag{2.13}$$

This expression may be re-written as

$$\eta_{ac} = \frac{\gamma^2}{1 + \left[\frac{\kappa^2}{(V_+)_1}\right] \left[(V_{nc})_2 + \frac{\sum_{i=1}^{2} f_i \varepsilon_{bi}}{\sum_{i=1}^{2} f_i q_i}\right]}. \tag{2.14}$$

Using the relation $k = \sum_{i=1}^{2} f_i q_i$ and multiplying by the propellant utilization efficiency η_u, the total thruster efficiency can be found:

$$(\eta_t)_2 = \frac{\gamma^2 \eta_u \frac{\kappa^2}{k}}{1 + \left[\frac{\kappa^2}{(V_+)_1}\right] \left[(V_{nc})_2 + \frac{\sum_{i=1}^{2} f_i \varepsilon_{bi}}{k}\right]}. \tag{2.15}$$

Though it is not known how the ion production cost ε_b will differ for single and double C_{60} ions, for the purpose of this analysis, one may arbitrarily assuming that $\varepsilon_{b2} = 2\varepsilon_{b1}$. Also, it is reasonable to assume that $(V_{nc})_2 = (V_{nc})_1$. Equation 2.15 can then be simplified further:

$$(\eta_t)_2 = \frac{\gamma^2 \eta_u \frac{\kappa^2}{k}}{1 + \kappa^2 \frac{2e}{m_i} \left(\frac{\gamma \eta_u}{g I_{sp}}\right)^2 (\varepsilon_b + V_{nc})}. \tag{2.16}$$

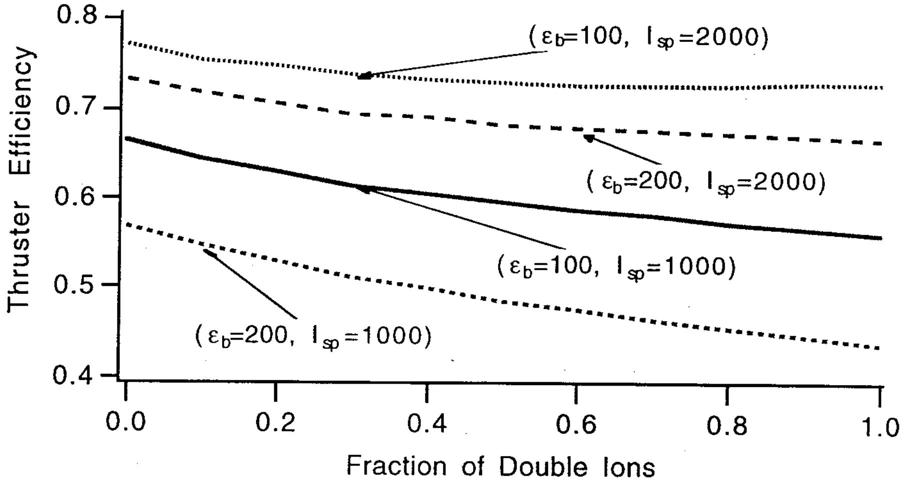

Figure 2.3: Efficiency of a C_{60} ion thruster as a function of fraction of extracted double ions. The four curves correspond to different values for ion production cost and specific impulse.

Equation 2.16 may then be compared with Equation 2.1 which is just the expression for total efficiency when only single ions are formed. The two equations are very similar, but differ by a correction factor κ^2/k in the numerator, and κ^2 in the denominator. Figure 2.3 shows the overall effect of double ion formation on thruster efficiency. The values used for V_{nc}, γ, and η_u were 10 V, 0.95, and 0.9, respectively. Note that the effect is rather small at higher specific impulse. In the above analysis, it was assumed that the propellant utilization efficiency was the same for both doubly and singly-charged species. Generally, this will not be the case, nor will the simplifying assumption $\varepsilon_{b2} = 2\varepsilon_{b1}$ hold. Also, the thrust-loss factor, γ already partially compensates for double ionization. However, the trend displayed in Figure 2.3 is correct. Double ionization does not appear to result in a large reduction in thruster efficiency at higher specific impulse. This may have been anticipated because the mass-to-charge ratio of C_{60}^{++} is nearly 2.75 times than that of singly charged xenon.

2.3.2 Fragmentation

An analysis similar to the one performed for multiple ionization can be performed for fragmentation of fullerene propellant molecules. There are many possible scenarios for the fragmentation process;

$$e^- + C_{60} \rightarrow C_n^+ + C_{60-n} + 2e^- \tag{2.17}$$

or

$$e^- + C_{60} \rightarrow C_n + C_{60-n}^+ + 2e^- \tag{2.18}$$

are two examples.

Carbon fragments may be ionized and accelerated, or may remain neutral and deposit on a thruster surface. Multiple fragments may be formed from a single C_{60} molecule, or there may be other higher-mass fullerenes present. There are many possibilities, so the analysis will be made by considering three fractions, f_1, f_2, and f_3, corresponding to the fraction of unfragmented C_{60}^+, another ionized fullerene molecules of mass n, and dissociatively ionized C_k^+ with the fragment C_{60-k}^+, respectively. The fraction of the fragment species that is ionized can be built into the propellant utilization efficiency for that particular species.

As before, the same mass flow rate, specific impulse, and thrust is assumed for both case 1, in which only unfragmented single ions are formed, and case 2, where fragments and other ions are formed in fractions given by f_1, f_2, and f_3. By equating the momenta of the exhaust in both cases, it is found that

$$(V_+)_1 = (V_+)_2 \left[f_1 + f_2\sqrt{\frac{n}{60}} + f_3\left(\sqrt{\frac{k}{60}} + \sqrt{\frac{60-k}{60}}\right)\right]^2 . \tag{2.19}$$

The beam currents in the two cases are

$$(J_B)_1 = \dot{m}\frac{q}{m}\eta_{u1} \tag{2.20}$$

and

$$(J_B)_2 = \dot{m}\frac{q}{m(f_1+f_3)+nf_2}\sum_i f_i(\eta_u)_i \tag{2.21}$$

where $(\eta_u)_i$ is the propellant utilization efficiency for the ith fragment species and η_{u1} is the propellant utilization efficiency of unfragmented C_{60}. Because the power is just the product of the beam current and beam voltage, the efficiency due to the presence of fragment ions can be expressed as

$$\eta_{pw} = \frac{P_1}{P_2} = \frac{\eta_{u1}\delta^2(f_1+f_3+f_2(n/m))}{\sum_i f_i(\eta_u)_i} \tag{2.22}$$

where $\delta = \left(f_1 + f_2\sqrt{\frac{n}{60}} + f_3\left[\sqrt{\frac{k}{60}} + \sqrt{\frac{60-k}{60}}\right]\right)$.

The electrical efficiency of the thruster is given by

$$\eta_{ac} = \frac{\gamma^2}{1+\frac{V_{nc}}{(V_+)_2}+\left[\frac{\sum_i f_i\eta_{ui}\varepsilon_{bi}}{(V_+)_2\sum_i f_i\eta_{ui}}\right]} \tag{2.23}$$

which simplifies to

$$\eta_{ac} = \frac{\gamma^2}{1+\frac{\delta^2}{(V_+)_1}\left[V_{nc}+\frac{\sum_i f_i(\eta_u)_i(\varepsilon_b)_i}{\sum_i f_i(\eta_u)_i}\right]}. \tag{2.24}$$

The total efficiency is then

$$(\eta_t)_2 = \frac{\gamma^2\eta_{u1}\delta^2 d/\sum_i f_i(\eta_u)_i}{1+\left(\frac{\delta\gamma\eta_u}{gI_{sp}}\right)^2\frac{2e}{m}\left[V_{nc}+\frac{\sum_i f_i(\eta_u)_i(\varepsilon_b)_i}{\sum_i f_i(\eta_u)_i}\right]} \tag{2.25}$$

where $d = (f_1 + f_3 + f_2(n/m))$. Note that equivalent neutralizer coupling voltages were assumed for the two cases, but no assumption has been made about the propellant utilization efficiencies for each species.

An example of particular interest is the case where the propellant is composed of 85% C_{60} and 15% C_{70}. Also, it will be assumed that 75% of the C_{60} is unfragmented, while 25%

Particle	f_i	η_i	ε_b (eV)
C_{60}	.63	.9	100
C_{70}	.15	.9	100
C_{58}	.11	.9	200
C_2	.11	.1/.9	200

Table 2.2: Parameters used to evaluate the effect of fragmentation on thruster performance.

dissociates into C_{58} and C_2. An assumption must also be made about the quantity ε_b for each species. Table 2.2 shows the values used to evaluate Equation 2.25 for this example. As with the example of the last section, V_{nc}, γ, and η_{u1} are 10 V, 0.95, and 0.9, respectively. Two different values for η_i were used for C_2. Figure 2.4 shows efficiency as a function of specific impulse for a pure C_{60} beam, a fragmented C_{60} beam with 90% of the C_2 fragments ionized and extracted, and a fragmented C_{60} beam with 10% of the C_2 fragments ionized and extracted. It is clear that the presence of a large number of carbon fragments in the ion beam greatly reduce the efficiency of the thruster.

2.4 Feasibility Issues

Although C_{60} appears to have many desirable characteristics as an ion thruster propellant, there are several issues which impact the feasibility of this concept. The first of these issues is the fragmentation of multiples of diatomic carbon from the C_{60} molecule. The carbon fragments present several difficulties: (1) their presence in the expelled ion beam represents a mass distribution which decreases the efficiency of the engine as shown above, (2) small fragment ions could result in sputter erosion of thruster components, resulting in decreased

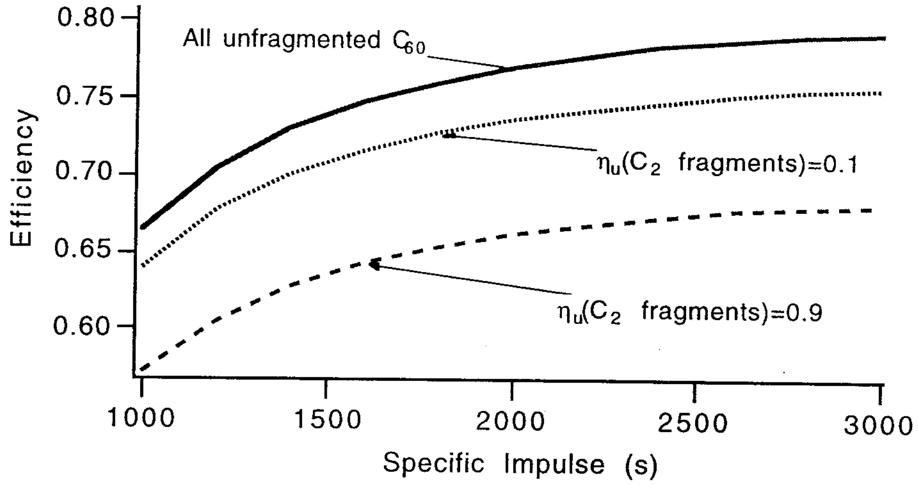

Figure 2.4: Efficiency of a C_{60} ion thruster as a function of specific impulse when fragmented ions are present. The curve corresponding to the highest efficiency is for entirely unfragmented C_{60}, and the two lower curves correspond to different extracted fractions of C_2 fragments.

engine lifetime, and (3) neutral carbon fragments could deposit on thruster surfaces, clog thruster components, and reduce overall propellant utilization efficiency.

A second issue of relevance is condensation of C_{60} within the discharge chamber. The potential difficulty presented by this issue is that C_{60} is a semiconductor (the conductivity at room temperature is approximately 1×10^{-14} $(\Omega\ \mathrm{cm})^{-1}$ [10]). Excessive condensation of the material could affect electrode operation in addition to clogging the propellant feed system. It will be necessary to heat the discharge chamber to maintain the C_{60} in vapor phase.

In the performance calculations, the neutral particle velocity of C_{60} was assumed to be the average thermal velocity of the molecules. However, if C_{60} ions are neutralized and reintroduced to the plasma following collisions with internal engine surfaces, a higher neutral particle velocity may result due to the tendency of fullerenes to recoil from surfaces [11]. The effect would be a decrease in propellant utilization efficiency and an increase in the ion production cost. Further, it is likely that there will be a large number of C_{60} anions in the discharge chamber because C_{60} forms stable negative ions [12] and will have an ample supply of Maxwellian electrons with which to do so. One possibility is that C_{60} anions will be accelerated into anode potential surfaces, lose their electrons, and be reintroduced as fast-moving neutrals. Another is that the presence of a large number of anions will increase propellant utilization efficiency because they will be repelled by the screen grid sheath, thereby containing the anions in the discharge chamber. Quantifying the effects of either positive or negative ion neutralization or anion formation requires a knowledge of the cross sections for these events.

2.5 Summary and Conclusions

A model for electron bombardment ion thrusters [5] was used to estimate the performance of fullerene ion thrusters relative to xenon ion thrusters. The large mass of C_{60} alone would indicate that fullerene ion thrusters could deliver high efficiency at moderate specific impulse. The impact of double ionization and fragmentation on thruster performance was also investigated. Double ionization does not appear to result in a large reduction in thruster efficiency. This result may have been anticipated because the mass-to-charge ratio of C_{60}^{++} is nearly 2.75 times than that of singly charged xenon. However, fragmentation of fullerene molecules could pose a problem for thruster operation, resulting in reduced propellant utilization efficiency and thruster lifetime.

References

[1] S. Leifer, D. Rapp, and W. Saunders "Electrostatic Propulsion Using C_{60} Molecules," *AIAA Journal of Propulsion and Power* **8(6)**, 1297 (1993).

[2] E. Torres, J. Matossian, J. Williams, and M. Martinez-Sanchez, "Prediction of the Performance of an Ion Thruster Using Buckminsterfullerene as the Propellant," *AIAA/SAE/ASME/ASEE 29th Joint Propulsion Conference* **AIAA 93-2494**, Monterey, California, (1993).

[3] M.J. Patterson, T.R. Verhey, "5kW Xenon Ion Thruster Lifetest," **AIAA 90-2543**, Orlando, FL, (1990).

[4] Beattie, J.R., Robson, R.R., Williams, J.D., "18-mN Xenon Ion Propulsion Subsystem," *AIDAA/AIAA/DGLR/JSASS 22nd International Electric Propulsion Conference* **IEPC-91-010**, Viareggio, Italy (1991).

[5] Brophy, J. R., "Ion Thruster Performance Model," NASA **CR-174810** (1984).

[6] D. Rapp and P. Englander-Golden, "Total Cross Sections for Ionization and Attachment in Gases by Electron Impact," *Journal of Chemical Physics* **43(5)**, 1464 (1965).

[7] C. Pan, M.P. Sampson, Y. Chai, R.H. Hauge, and J.L. Margrave, "Heats of Sublimation from a Polycrystalline Mixture of C_{60} and C_{70}," *Journal of Physical Chemistry* **95**, 2944 (1991).

[8] A. Tokmakoff, D.R. Haynes, and S.M. George, "Desorption Kinetics of C_{60} Multilayers from $Al_2O_3(0001)$," *Chemical Physics Letters* **186**, 450 (1991).

[9] D. Rapp and S. Leifer, "Effect of the Use of C_{60} as a Propellant in Ion Thrusters," *JPL Report* **D-10169**, Pasadena, CA, (1992).

[10] J. Mort, R. Ziolo, M. Machonkin, D. Huffman, and M. Ferguson, "Electrical Conductivity Studies of Undoped Solid Films of C_{60}/C_{70}," *Chemical Physics Letters* **186(2,3)**, 284 (1991).

[11] R. Beck, P. St. John, M. Alvarez, F. Diederich, and R. Whetten, "Resilience of All-Carbon Molecules C_{60}, C_{70}, and C_{84}: A Surface Scattering Time-of-Flight Investigation," *Journal of Physical Chemistry* **95(21)**, 8402 (1991).

[12] P.A. Limbach, L. Schweikhard, K.A. Cowen, M.T. McDermott, A.G. Marshall, J.V. Coe, "Observation of the Doubly Charged, Gas-Phase Fullerene Anions C_{60}^{2-} and C_{70}^{2-}," *Journal of the American Chemical Society* **113**, 6795 (1991).

Chapter 3

Thermal Stability of Fullerenes

3.1 Introduction

Since 1991, three groups [1]-[3] have reported the development of ion thrusters which utilize fullerene propellant. Two of the groups [1,2] successfully sustained DC fullerene plasma discharges using tungsten filament cathode ion sources. However, both of these groups reported substantial erosion of the filament cathodes used in their devices. In addition, the presence of a significant quantity of toluene-insoluble carbonaceous material was observed in the effusion cells of both groups after heating.

These observations led to concern that fullerenes were either thermally unstable at the operating temperatures of the thruster, or were reacting either catalytically or stoichiometrically with contaminants or metal surfaces in the thruster at elevated temperatures. Because this concern impacts the fundamental feasibility of the development of fullerene ion thrusters, a study of fullerene decomposition kinetics was conducted.

In addition to practical applications such as effusive fullerene sources for ion thruster operation, investigations of fullerene decomposition kinetics can provide insights into the chemistry of fullerene formation because ring-rearrangement steps are believed to be involved in both processes [4,5].

Since fullerenes became available in macroscopic quantities in 1991 [7], there have been several experimental studies of the thermal stability of C_{60} [8]-[10]. Frum *et al.* [11] observed thermal degradation of C_{60} heated to 1223 K while studying its infrared emission spectrum, while Sundar *et al.* [10] observed that solid C_{60} decomposes into amorphous carbon upon heat treatment beyond 993 K for 24 hours. However, neither of these studies attempted to quantify the decomposition kinetics.

Two studies have reported rate constants for thermal decomposition of gas-phase C_{60} at higher temperatures [8,9]. Von Gersum, Kruse, and Roth [8] studied pyrolysis of shock-heated C_{60} dispersed in argon over the temperature range from 2370 K to 3500 K. They report an activation energy of 120 kJ/mol for the decay of broad-band emission near 490 nm which they attribute to C_{60}, and a value of 190 kJ/mol for the appearance of C_2 spectral emission features. Kolodney, Tsipinyuk, and Budrevich [9] used a two-stage effusive source of C_{60} to study thermal decomposition in the temperature range between 1720 K and 1970 K. They report an Arrhenius activation energy of 385±30 kJ/mol for unimolecular decay. At higher energies, there are numerous reports of electron-impact-induced [12] and laser-induced fragmentation [13,14] of C_{60}. The primary decomposition channel at high excitation energy is believed to be:

$$C_{60} \rightarrow C_{58} + C_2 \tag{3.1}$$

which is endothermic by 6-13 eV [12]-[15].

Thermal decomposition has also been the subject of several theoretical studies [5], [16]-

[18]. Molecular dynamics simulations show that C_{60} decomposes within a few hundred vibrational periods when heated to a temperature of 4900 K – 5500 K [16]-[18]. In at least one study [5], simulations show the C_{60} decaying via reaction (1) without the cage opening. In this chapter, measurements of the thermal decomposition of a solid fullerene mix over the temperature range from 973 K to 1273 K is reported. This is the first experimental investigation of solid state fullerene decomposition kinetics [6].

3.2 Experimental Procedure

3.2.1 Sample Preparation

A method similar to that of Sundar *et al.* [10] was employed to determine the thermal stability of fullerene mix. Quartz ampoules were each filled with approximately 10 mg of fullerene extract containing C_{60} and C_{70} in a ratio of approximately 85% to 15%. The fullerene mix was Soxhlet extracted with toluene from soot produced by Ulvick Industries. Pure C_{60} from MER Corporation and pure C_{70} from Term Ltd. were used as standards for compositional analysis. The fullerene-containing ampoules were placed under dynamic vacuum in the mid 10^{-6} Torr range and heated to temperatures between 473 K and 523 K to eliminate solvent and hydrocarbon impurities [19]. Partial pressures of monatomic and diatomic oxygen, CO and N_2, CO_2, OH, H_2O, toluene, and benzene were monitored using a MKS model 600A PPT Residual Gas Analyzer. The preheating of the samples lasted anywhere from 6 to 16 hours, depending on the concentration of solvent impurities in the powder. Upon initial heating, there was a rapid and significant increase in toluene partial pressure, with moderate increases in O_2 and H_2O. Some of the observed oxygen may have come from C_{60} epoxide. Figure 3.1 shows RGA partial pressure traces of the outgassing species for C_{60}, C_{70} and mixed fullerene samples. The ampoules were then vacuum sealed and placed in a tube furnace for durations of 5 minutes to 6 hours. Sets of samples were prepared and heated to 873 K, 973 K, 1073 K, 1098 K, 1123 K, 1148 K, 1173 K, and 1273 K. After removing the samples from the tube furnace, it was noted that in most cases, the fullerene powder had remained at one end of the ampoule with only a slight coating of soot on the walls. However, samples heated to 1273 K for a few minutes or to 1173 K for one hour formed a thick black coating on the entire inner surface of the ampoules.

3.2.2 UV-VIS Absorption Spectroscopy

Remaining fullerene content was determined by UV absorption spectroscopy using a Cary 5E UV-VIS-NIR spectrophotometer and a Hewlett-Packard model HPUV 8452A spectrometer. A 1.0 cm path length was used with blank solvent as the reference. The powder samples were placed in 200 ml of methylene chloride or toluene and sonicated. A further dilution of 1:10 was made for analysis. The concentrations of C_{60} and C_{70} were determined by monitoring the 336 nm and 384 nm absorption features, respectively.

The 260 nm peak of C_{60} was also monitored in the methylene-chloride-dissolved samples, but was obscured by the strong absorption by toluene at this wavelength. Significant quantities of seemingly insoluble material were observed in the methylene chloride solutions after sonicating for several hours, even though the solubility of C_{60} in methylene chloride has been reported as 0.26 mg/ml [20]. Some of the residual solid was found to be soluble in toluene. Subsequently, all remaining samples were analyzed in toluene. Peak intensities were corrected for initial sample weight, then correlated to remaining fullerene material. Data are shown in Appendix A. Repeatability of dilution preparation and inhomogeneity

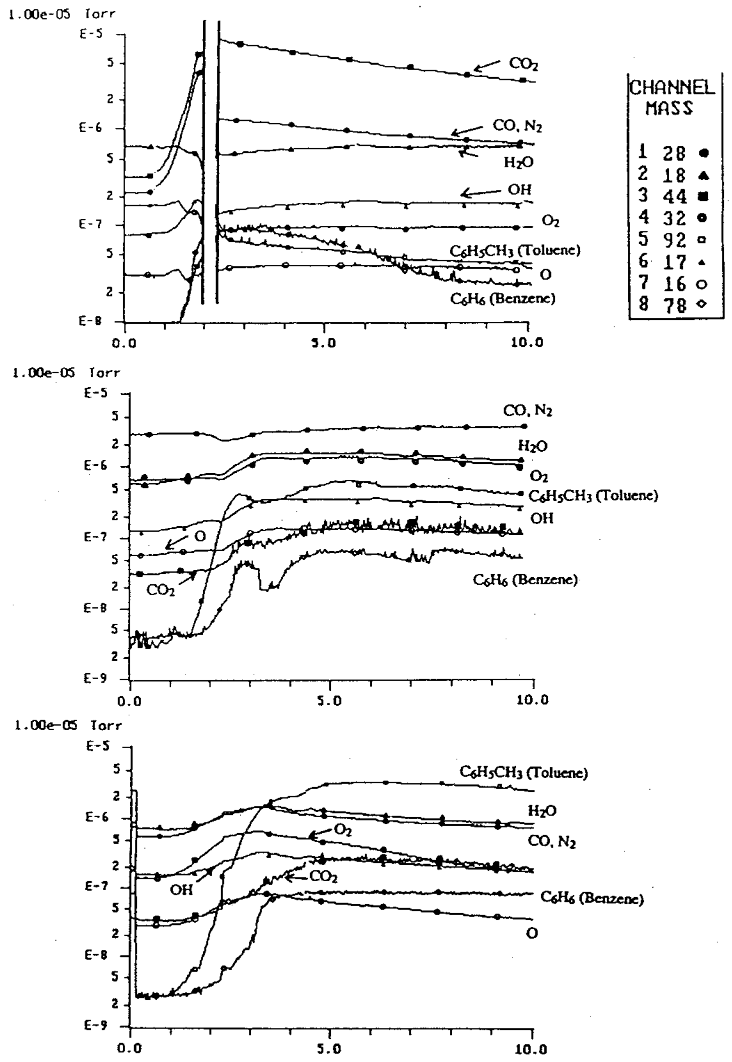

Figure 3.1: Residual Gas Analyzer traces of the partial pressures of various adsorbates and co-crystallized solvents outgassing from fullerene samples. Top: C_{70}, center: C_{60}, and bottom: mixed fullerenes.

of the fullerene mix were the main sources of error. As a result, the peak height of the 336 nm absorption feature exhibited sample-to-sample variations of 3.7%. The contribution to absorption at this wavelength by a 15% C_{70} content is approximately 12%. The amount of higher fullerenes (C_n for $n > 70$) contained in the samples was not determined.

3.3 Results and Discussion

3.3.1 Diffuse Reflectance FTIR Spectroscopy

To verify that decomposition was not a result of reaction or catalysis with impurities, diffuse reflectance Fourier transform infrared spectroscopy was used to analyze the decomposed material. Figures 3.2, 3.3,and 3.4 show spectra of untreated fullerene mix, a sample heated to 1073 K in vacuum for 1 hour, and a sample heated for 18 hours at 523 K in nitrogen and air, respectively. Note the appearance of cyclic anhydride features in the 1800 to 1000 cm^{-1} region of Figure 3.4 similar to those reported elsewhere [21]. However, no oxidation products are evident in the sample heated to 1073 K, although only 50% of the material remained as fullerene. The high concentration of carbon black in the sample heated to 1073 K resulted in the relatively low transmittance seen in Figure 3.3. Small amounts of hydrocarbon impurities are evident in all of the samples. Also, there is a possibility that at these temperatures, any intermediate compounds will have decomposed, leaving only CO_2 and CO as reaction products and catalysts. It was not determined whether these gases were present in the sealed ampoules after heating.

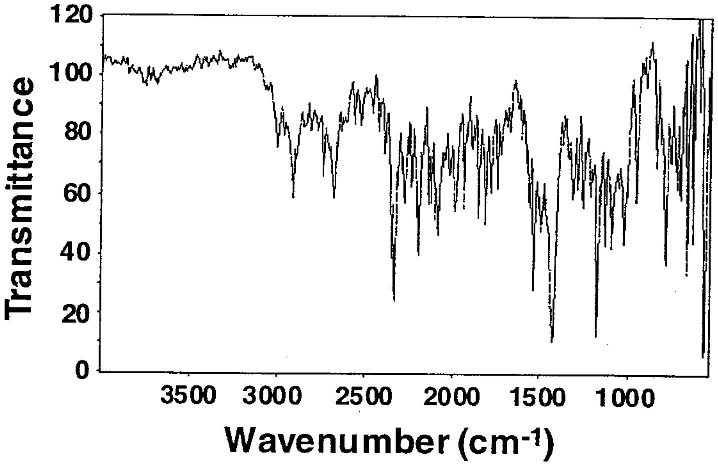

Figure 3.2: FTIR spectrum of fullerene mix annealed in vacuo at 523 K for 18 hours to remove solvents and adsorbed gases.

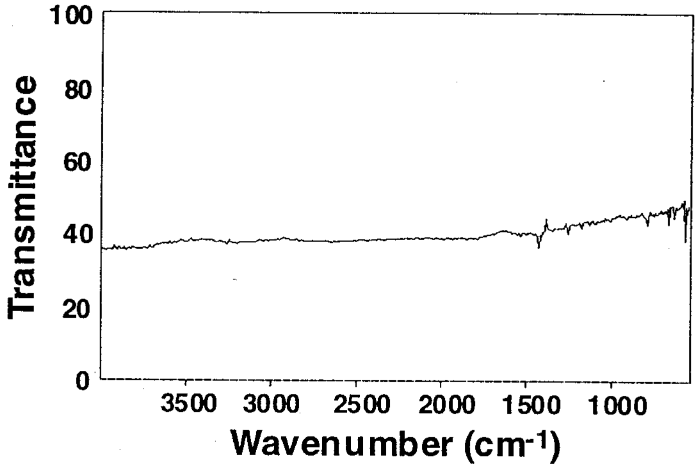

Figure 3.3: FTIR spectrum of a fullerene sample heated to 1073 K for 1 hour. The small trasmittance results from strong absorption by the amorphous and graphitic carbon.

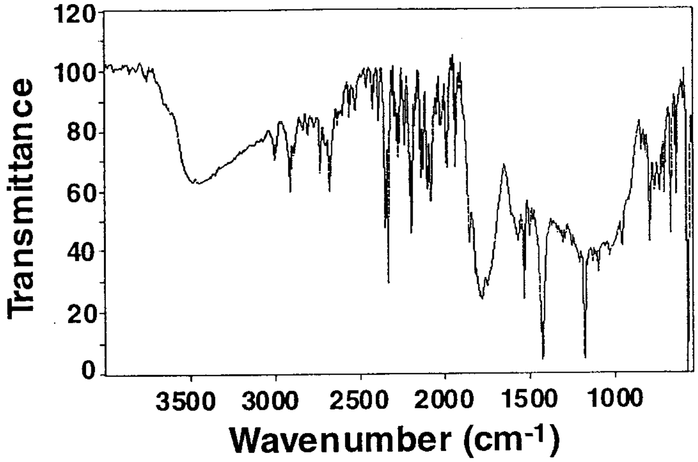

Figure 3.4: FTIR spectrum of fullerene sample baked in nitrogen and air at 523 K for 18 hours.

3.3.2 Microscopy

Samples that had been heated to temperatures greater than 1273 K were completely insoluble in toluene. This material was examined with an X-ray diffractometer, which showed no diffraction peaks. Raman spectroscopy also failed to show evidence of an ordered structure (see Figure 3.5); only two broad peaks around 1350 and 1580 cm^{-1} characteristic of graphitic carbon were evident. Although all indications were that the fullerenes had decomposed into amorphous carbon, the material appeared distinctly faceted. Scanning-electron-microscope images of this material are shown in Figures 3.6 and 3.7. A selected area diffraction pattern of one of the structures in a Phillips 301 transmission electron microscope produced only rings (Figure 3.8) from graphite polycrystals. Figure 3.9 is a bright field image of the faceted structure. The fullerite appears to have pyrolyzed without destroying the crystal shape.

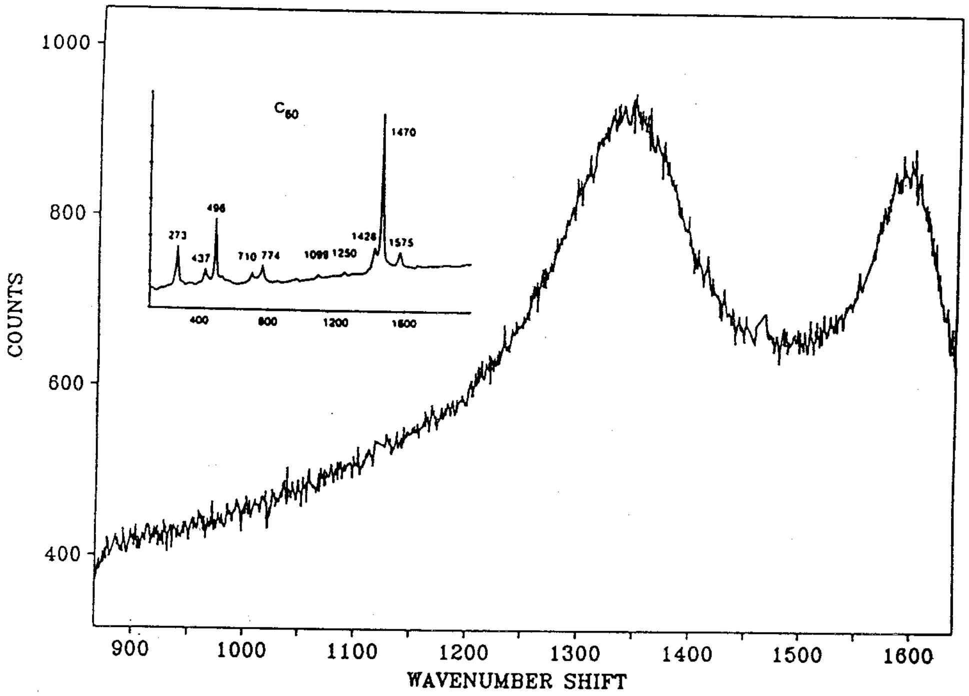

Figure 3.5: Raman spectrum of toluene-insoluble carbon material showing no peaks corresponding to fullerenes, only two broad signals around 1350 and 1580 cm^{-1} characteristic of graphite. The inset shows the location of peaks in a Raman spectrum of C_{60} taken from Reference [22].

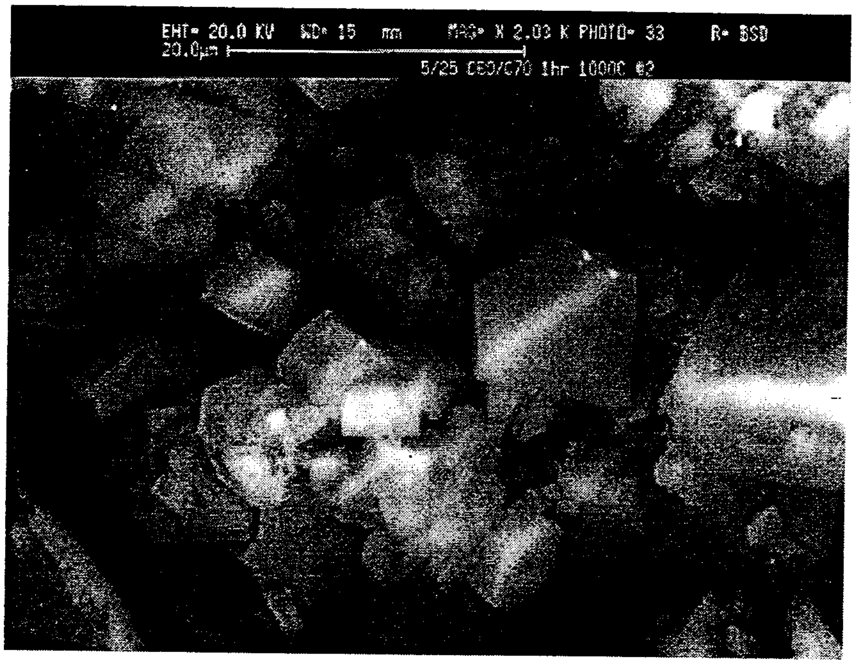

Figure 3.6: Scanning-electron-micrograph of toluene-insoluble carbon material. The magnification is ×2030. Although the material appears crystalline, it shows no x-ray diffraction peaks.

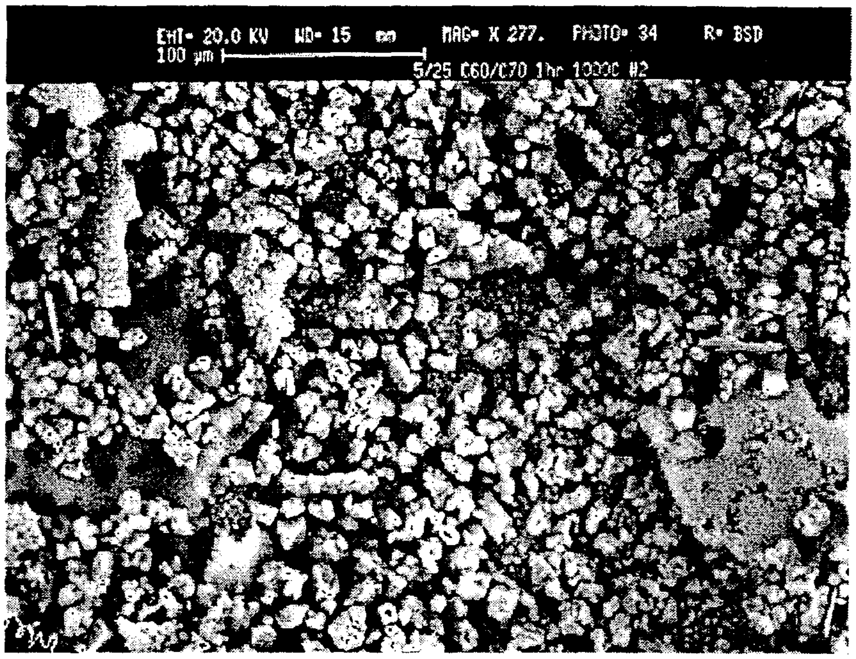

Figure 3.7: Scanning-electron-micrograph of toluene-insoluble carbon material. The magnification is ×277.

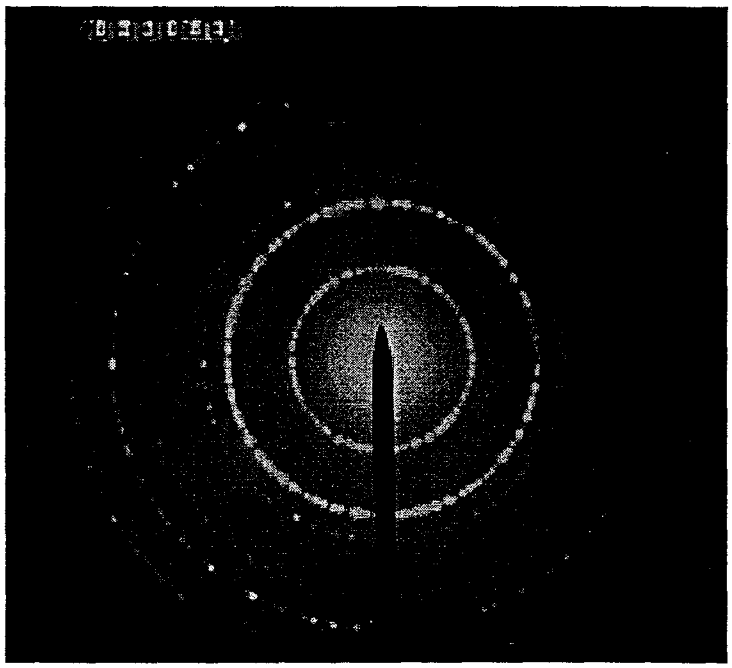

Figure 3.8: Diffraction rings from decomposed fullerenes. The rings can be indexed as graphite polycrystals.

Figure 3.9: Bright-field transmission-electron-micrograph of fullerite-shaped carbon structure.

3.3.3 Decomposition Kinetics

Figure 3.10 shows the UV absorption spectrum of mixed fullerene samples heated at 1073 K for 20, 60, 180, and 360 minutes. The solutions were prepared with methylene chloride. Figure 3.11 shows the decay of the 336 nm peak height of the toluene-dissolved samples heated to 1098 K, 1123 K, 1148 K, and 1173 K. There were no discernable changes in the ratio of C_{60} to C_{70}. Therefore, it was concluded that the difference in their decay rates is within the uncertainty of this experiment. By assuming the fullerene decay data shown in Figure 3.11 may be described by unimolecular decomposition, decay constants $k(T)$ were obtained such that the remaining fullerene concentration was proportional to $\exp(-k(T)t)$. The exponential curves which yielded the best fit to the data are also shown in Figure 3.11.

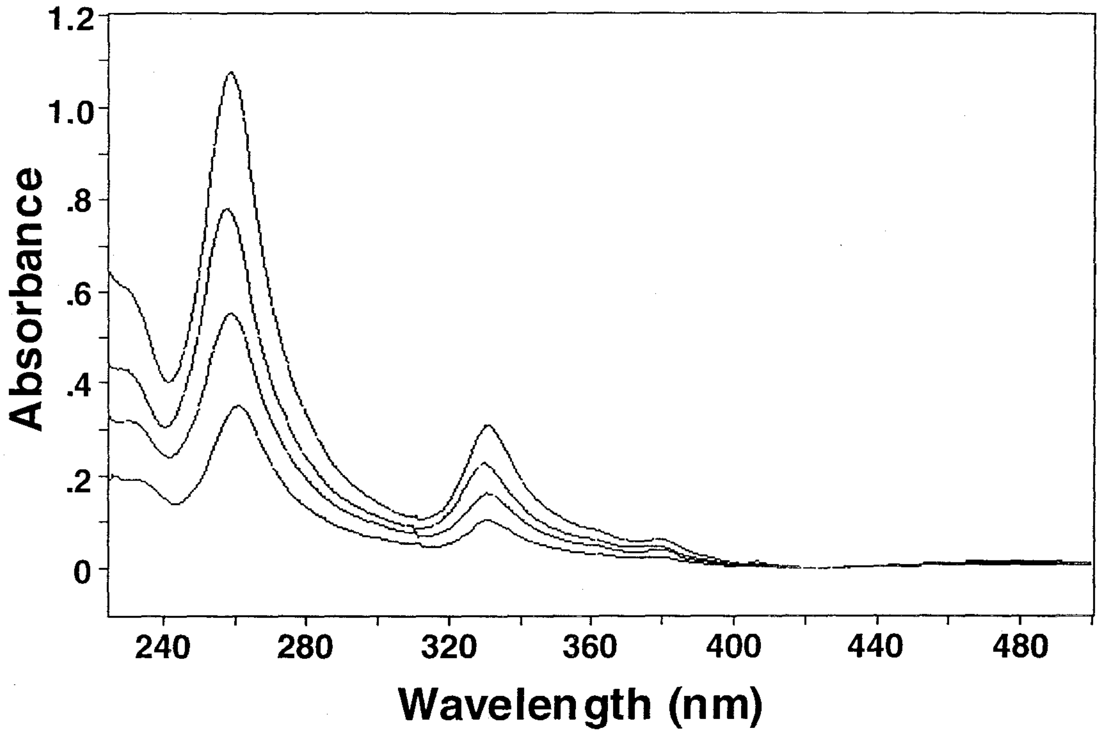

Figure 3.10: UV-visible spectrum of fullerene heated for 0.3, 1.0, 3.0, and 6.0 hours. Decreasing peak intensity reflects lower fullerene content in the solutions. The solvent was methylene chloride.

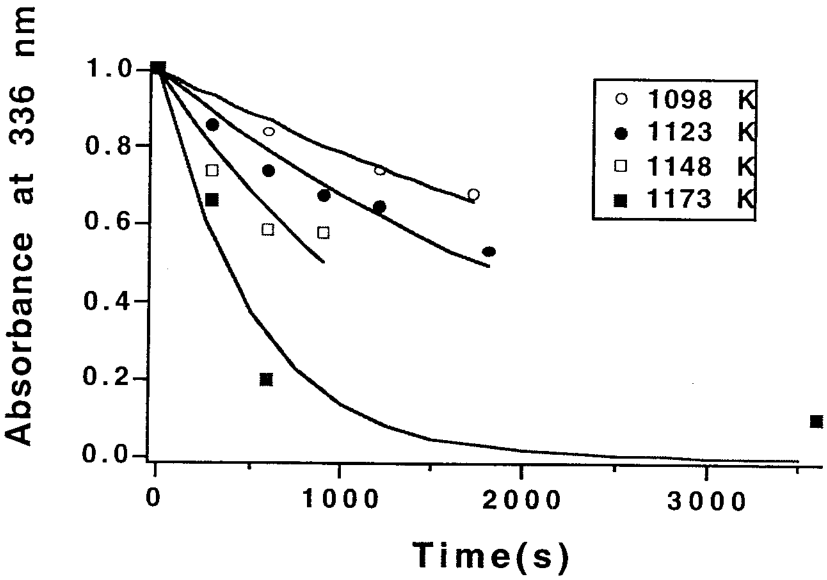

Figure 3.11: Data points and exponential curve fits to the peak intensity of the 336 nm peak of C_{60} seen in the UV-visible spectrum. The decay constants, k(T), were determined from these curve fits.

An Arrhenius plot of the rate constants determined from the curve fits of Figure 3.11 is shown in Figure 3.12. The best-fit line gives a rate constant of:

$$k(T) = 1.24 \times 10^9 \exp(E_a/RT)s^{-1} \tag{3.2}$$

where $E_a = 266\pm9$ kJ/mol.

This activation energy is more than twice as high as the 120 kJ/mol, and approximately 30 percent smaller than the 385±30 kJ/mol previously reported for the thermal decomposition of pure C_{60} in the gas phase [8,9]. A comparison of these results with the previously published data is shown in Figure 3.13. Remarkably, all three sets of data can be described by a single Arrhenius fit to within an order-of-magnitude uncertainty over 8 orders-of-magnitude variation. A best-fit line to the combined data gives an activation

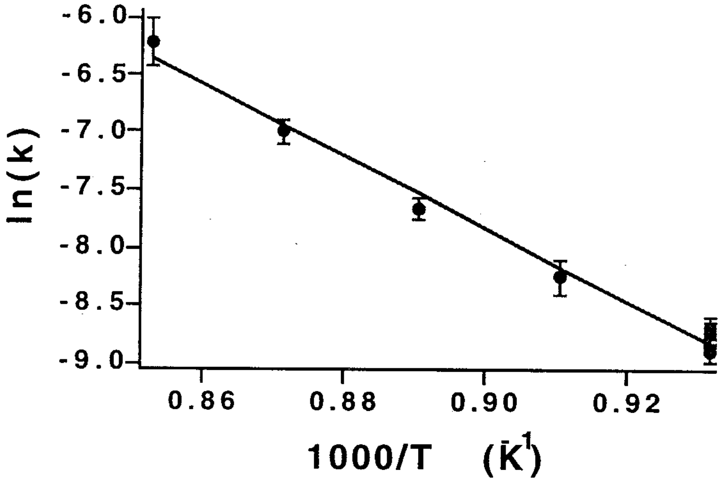

Figure 3.12: Arrhenius plot of the thermal disintegration of a C_{60}/C_{70} mix.

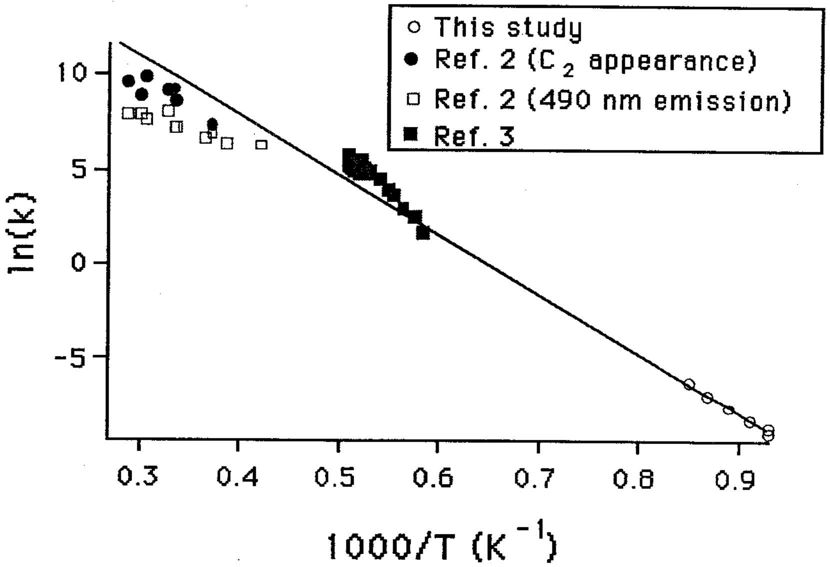

Figure 3.13: A combined Arrhenius plot showing the data from Figure 3.12 and that of References [9,8].

energy of 228 kJ/mol.

All three sets of experimental data indicate thermal decomposition rates for C_{60} at low temperature which are much higher than one would predict for a single step C_2 ejection process. For example, if it is assumed that this process has a rate of 10^{11} s^{-1} at 5000 K and an activation energy of 675 kJ/mol (consistent with the endothermicity of reaction [1]), then the rate at 1000 K would be 6×10^{-18} s^{-1} — orders of magnitude below the experimental value of 2×10^{-5} s^{-1}.

Further examination of the applicability of the molecular dynamics studies of fullerene decomposition can be made by finding a rate equation for C, the amount of material present:

$$\frac{dC}{dt} = ae^mT^m\exp(-E_a/RT)C \tag{3.3}$$

and integrating:

$$ln(\frac{C}{C_0}) = ae^m\int_0^t T^m\exp(-E_a/RT)dt'. \tag{3.4}$$

Allowing the temperature to scale as a function of time, $T = bt$, gives

$$ln(\frac{C(T)}{C_0}) = -\frac{a}{b}e^m\int_{T_i}^{T_f} T^m\exp(-E_a/RT)dT. \tag{3.5}$$

Setting $u = T_f/T$ yields

$$ln(\frac{C}{C_0}) = -\frac{a}{b}e^mT_f^{m+1}\int_1^\infty \frac{\exp(-ku)du}{u^{m+2}} \tag{3.6}$$

where $k = E_a/RT_f$. With $m = 0$ and using the exponential integral $E_n(x)$, the expression becomes

$$ln(\frac{C}{C_0}) = -\frac{a}{b}e^mT_fE_2(\frac{E_a}{RT_f}), \tag{3.7}$$

where the exponent of u, $m + 2 = n$, has been substituted to give the exponential integral

E_2. When C/C_0 is on the order of $1/e$, the transcendental equation

$$\frac{b}{aT_f} = E_2(\frac{E_a}{RT_f}) \tag{3.8}$$

is obtained. Using a value of 3.57×10^{14} K/s for b would indeed yield a thermal disintegration temperature, T_f, of approximately 5500 K if a were on the order of 10^{13} s^{-1}. Such a value for a is typical in many unimolecular decomposition reactions; the entropy of activation,

$$a = \frac{kT}{h}\exp(\Delta S/R), \tag{3.9}$$

is large for simple molecules where there are very few ways to rearrange energy between the various degrees of freedom. However, for a large, complex molecule such as C_{60}, there is significant rearrangement of energy among the degrees of freedom, and therefore a large decrease of entropy in the formation of the transition state. It has been shown experimentally that a for C_{60} is at least four orders of magnitude smaller than that typically found for small molecules.

Figure 3.14 shows a combined Arrhenius plot derived from molecular dynamics simulations [16]-[18] and the experimental data of fullerene thermal decomposition. It clear that the Arrhenius plot derived from the theortically predicted rate constants yield a much higher activation energy than that from the experimental data. It should be noted that all of the theoretical studies of fullerene fragmentation and annealing use simulation times on the order of picoseconds for modeling the C_2 ejection process.

These results suggest that a second, low-barrier decay channel exists. This process may include one or more ring-rearrangement isomerization reactions prior to ejection of a C_2 [9,5]. However, theoretical estimates of the barriers for ring-rearrangement steps suggest the lowest barrier is still 810 kJ/mol. Clearly, more theoretical work will be required to

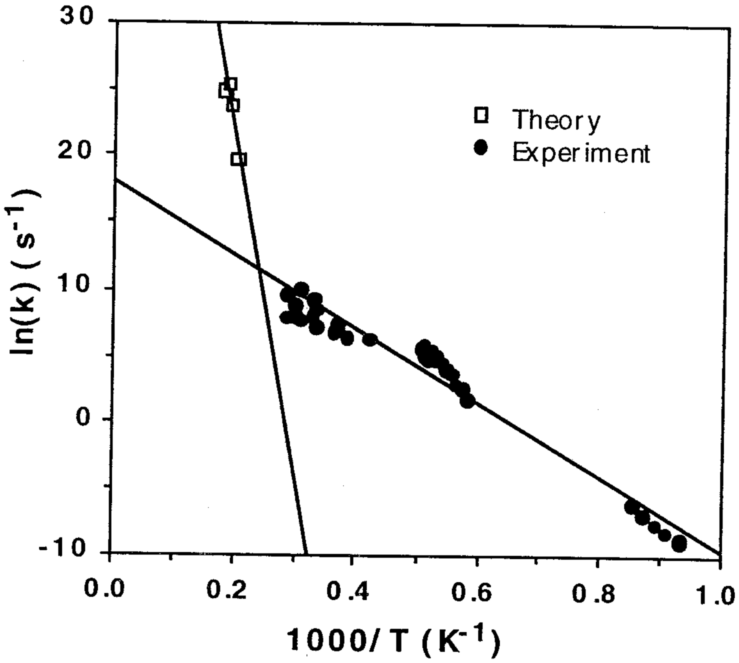

Figure 3.14: A combined Arrhenius plot showing experimentally determined decomposition of fullerenes from Figure 3.13 and theoretically determined decay constants found from molecular dynamics simulations [16]-[18].

explain the low activation energy for thermal decomposition of C_{60}.

It has been observed that even though initial sublimation of fullerene powder will result in a loss of 10 to 20% soluble material, subsequent sublimation of fullerene condensed from the vapor phase will yield smaller quantities of degraded material [23], implying that co-crystallized impurities are responsible for the decomposition. However, because the results reported here are consistent with those found for gas-phase samples, and because no spectroscopic evidence of solvents was found, it is doubtful that treating the material with consecutive sublimation steps would significantly change the results. Recently, this experiment was duplicated at the University of Pennsylvania with fullerenes contacting gold foil instead of quartz ampoule walls [24]. The results of the Penn experiment were the same as those reported here.

One possible mechanism for fullerene decomposition may involve polymerization of the solid. Both Li and coworkers [25], and Rao *et al.* [26] have observed photoinduced polymerization of C_{60} samples. In their experiments, the fullerene molecules linked together in a covalently bonded FCC structure (see Figure 3.15). Li *et al.* found that photopolymerized skins of C_{60} single crystals were accompanied by amorphous carbon. However, Rao *et al.* were able to prepare polymerized C_{60} under conditions such that the material could revert to closed C_{60} molecules in a van der Waals solid when heated. In addition, they reported that thought the polymerized fullerenes were no longer soluble in toluene, the material retained the spectroscopic character of C_{60}, though optical absorption and x-ray diffraction peaks were broadened.

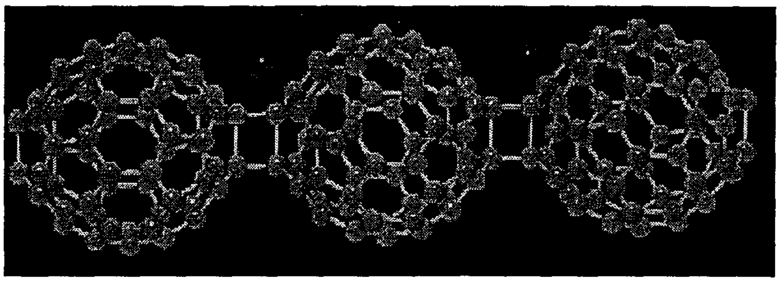

Figure 3.15: Polymerized chain of fullerene molecules.

3.4 Conclusions

An activation energy of 266±9 kJ/mol for the solid-state thermal decomposition of a fullerene mix over a temperature range from 1073 K to 1173 K has been found. The rate constant is consistent with the previously published experimental data for unimolecular decomposition of vapor phase C_{60}. SEM images of the decomposed sample show a faceted structure, though X-ray diffraction, Raman spectroscopy, and TEM all show that the material is a combination of amorphous carbon and graphite. Diffuse reflectance FTIR spectroscopy does not detect the presence of intermediate compounds. The integrity of the fullerite crystal shape after decomposition makes it unlikely that the reaction mechanism is catalysis with impurities or quartz surfaces. Hence, the degradation is attributed to solid-state unimolecular decay.

Further work to extend the experimental data to temperatures higher than those explored in this study, yet lower than that of prior investigations [8,9] will require another technique. *In situ* monitoring of Bragg peak intensity of heated fullerene samples [29] may be successful in yielding more insight into fullerene decomposition kinetics.

The result of this investigation makes the existence of a liquid phase of C_{60} [27]-[29]

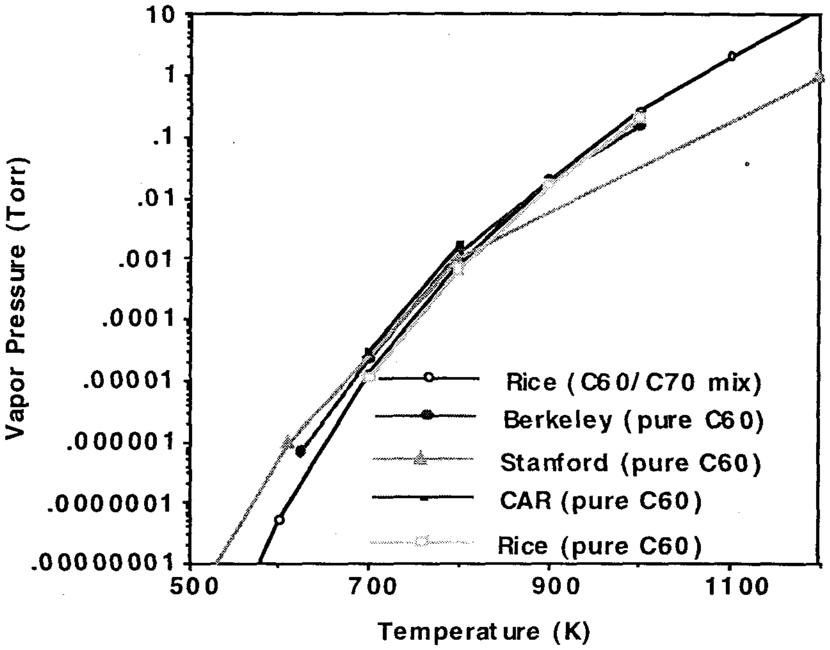

Figure 3.16: Vapor pressure of C_{60} as a function of temperature from References [30]-[33].

highly unlikely. It also places bounds on the range of operating temperatures of fullerene vapor sources and ionization techniques for producing fullerene plasmas. Thoriated tungsten hollow cathodes used in state-of-the-art ion thrusters typically operate at temperatures in excess of 1300 K. Such temperatures clearly preclude their use for extended fullerene ion thruster operation. Furthermore, the narrow window of operating temperatures for fullerene thrusters constrains the maximum achievable vapor pressure of propellant, and therefore the flow rate per unit area as well. Figure 3.16 shows the experimentally determined vapor pressure of C_{60} as a function of temperature [30]-[33]. Because thruster operating temperatures will have to be maintained below approximately 1073 K in order to avoid significant propellant degradation, the maximum vapor pressure in the system will necessarily be at or below approximately 1.0 Torr.

References

[1] J. Anderson and D. Fitzgerald, "Experimental Investigation of Fullerene Propellant for Ion Propulsion," **IEPC-93-033**, Seattle, Washington, September (1993).

[2] Hruby V., Martinez-Sanchez M., Bates S., and Lorents D., "A High Thrust Density, C_{60} Cluster Ion Thruster," *25th AIAA Plasmadynamics and Lasers Conference*, **AIAA 94-2466**, Colorado Springs, Colorado, June, (1994).

[3] H. Takegahara and Y. Nakayama, "C_{60} Molecule as a Propellant for Electric Propulsion," *23rd International Electric Propulsion Conference*, **IEPC-93-032**, Seattle, Washington, September (1993).

[4] C.I. Curl ,"On the Formation of the Fullerenes," *Philosophical Transactions of the Royal Society of London A* **343**, 19 (1993).

[5] R.L. Murry, D.L. Strout, G.K. Odom, and G.E. Scuseria, "Role of sp^3 Carbon and 7-Membered Rings in Fullerene Annealing and Fragmentation," *Nature* **366**, 665 (1993).

[6] S. Leifer, D. Goodwin, M. Anderson, and J. Anderson, "Thermal Decomposition of a Fullerene Mix," *Physical Review B* **51(15)**, 9973 (1995).

[7] W. Krätschmer, L.D. Lamb, K. Fostiropoulos, and D. Huffman, "Solid C_{60} – a New

Form of Carbon," *Nature* **347**, 354 (1990).

[8] S. von Gersum, T. Kruse, and P. Roth, "Spectral Emission During High Temperature Pyrolysis of Fullerene C_{60} in Shock Waves," *Berichte Bunsen-Gesellschaft fur Physikialische Chemie* **98(7)**, 979 (1994).

[9] E. Kolodney, B. Tsipinyuk, and A Budrevich, "The Thermal Stability and Fragmentation of C_{60} Molecules up to 2000 K on the Millisecond Timescale," *Journal of Chemical Physics* **100(11)**, 8452 (1994).

[10] C.S. Sundar, A. Bharathi, Y. Hariharan, J. Janaki, V. Sankara Sastry, T.S. Radhakrishnan, "Thermal Decomposition of C_{60}," *Solid State Communications* **84(8)**, 823 (1992).

[11] C.I. Frum, R Engleman, H.G. Hedderich, P.F. Bernath, L.D. Lamb, and D.R. Huffman, "The Infrared-Emission Spectrum of Gas-Phase C_{60} (Buckminsterfullerene)," *Chemical Physics Letters* **176(6)**, 504 (1991).

[12] a) M. Foltin, M. Lezius, P. Scheier, and T.D. Märk, "On the Unimolecular Fragmentation of C_{60}^{+} Fullerene Ions - the Comparison of Measured and Calculated Breakdown Patterns," *Journal of Chemical Physics* **98(12)**, 9624 (1993), b) M. Lezius, P. Scheier, M. Foltin, B. Dünser, T. Rauth, V.M. Akimov, W. Krätschmer, T.D. Märk, "Interaction of Free-Electrons with C_{60} - Ionization and Attachment Reactions," *International Journal of Mass Spectrometry and Ion Processes* **129**, 49 (1993).

[13] R.K. Yoo, B. Ruscic, and J. Berkowitz, "Vacuum Ultraviolet Photoionization Mass Spectrometric Study of C_{60}," *Journal of Chemical Physics* **96(2)**, 911 (1992).

[14] a) P. Wurz and K.R. Lykke, "Kinetics of Multiphoton Excitation and Fragmentation of C_{60}," *Chemical Physics* **184(1-3)**, 335 (1994), b) P. Wurz, K.R. Lykke, "Multiphoton Excitation, Dissociation, and Ionization of C_{60}," *Journal of Physical Chemistry* **96(25)**, 10129 (1992).

[15] C. Lifshitz, "Energetics and Dynamics of Ionization and Dissociation of Fullerene Carbon Clusters," *Mass Spectrometry Reviews* **12(5-6)**, 261 (1993).

[16] B.L. Zhang, C.Z. Wang, C.T. Chan, and K.M. Ho, "Thermal Disintegration of Carbon Fullerenes," *Physical Review B* **48(15)**, 1138 (1993).

[17] S. Serra, S. Sanguinetti, and L. Colombo, "Pre-fragmentation Dynamics of C_{60}. A Molecular Dynamics Investigation," *Chemical Physics Letters* **225**, 191 (1994).

[18] C. Xu and G.E. Scuseria, "Tight-Binding Molecular Dynamics Simulations of Fullerene Annealing and Fragmentation," *Physical Review B* **72(5)**, 669 (1994).

[19] J. Milliken, T.M. Keller, A.P. Baronavski, S.W. McElvany, J.H. Callahan, and H.H. Nelson, "Thermal and Oxidative Analyses of Buckminsterfullerene," *Chemistry of Materials* **3**, 386 (1991).

[20] R.S. Ruoff, D.S. Tse, R. Malhotra, and D. Lorents, "Solubility of C_{60} in a Variety of Solvents," *Journal of Physical Chemisty* **97**, 3379 (1993).

[21] A.M. Vassallo, L.S.K. Pang, P.A. Cole-Clarke, and M.A. Wilson, "Emission FTIR Study of C_{60} Thermal Stability and Oxidation," *Journal of the American Chemical Society* **113**, 7820 (1991).

[22] D. Bethune, G. Meijer, W. Tang, H. Rosen, W. Golden, H. Seki, C. Brown, and M. de Vries, "Vibrational Raman and Infrared Spectra of Chromatographically Separated C_{60} and C_{70} Fullerene Clusters," *Chemical Physics Letters* **179(1,2)**, 181 (1991).

[23] Don Bethune, IBM Almaden, Personal Communication, March, (1995).

[24] Paul Heiney, University of Pennsylvania, Personal Communication, March, (1995).

[25] J. Li, M. Ozawa, N. Kino, T. Yoshizawa, T. Mitsuki, H. Horiuchi, O. Tachikawa, K. Kishio, and K. Kitazawa, "Photopolymerized Skins of C_{60} Crystals," *Chemical Physics Letters* **227**, 572 (1994).

[26] A. Rao, P. Zhou, K. Wang, G. Hager, J. Holden, Y. Wang, W. Lee, X. Bi, P. Eklund, D. Cornett, M. Duncan, and I. Amster, "Photoinduced Polymerization of Solid C_{60} Films," *Science* **259**, 955 (1993).

[27] A. Cheng, M. Klein, and C. Caccamo, "Prediction of the Phase-Diagram of Rigid C_{60} Molecules," *Physical Review Letters* **71(8)**, 1200 (1993).

[28] M. Hagen, E. Meijer, G. Mooij, D. Frenkel, and H. Lekkerkerker, "Does C_{60} Have a Liquid Phase," *Nature* **365(6445)**, 425 (1993).

[29] J.E. Fischer and P.A. Heiney, "Order and Disorder in Fullerene and Fulleride Solids," *Journal of the Physics and Chemistry of Solids* **54(12)**, 1725 (1993).

[30] J. Abrefah, M. Balooch, W.J. Siekhaus, and D.R. Olander, "Vapor Pressure of Buckminsterfullerene," *Applied Physics Letters* **60(11)**, 1313, (1992).

[31] A. Tokmakoff, D.R. Haynes, and S.M. George, "Desorption Kinetics of C_{60} Multilayers from Al_2O_3(0001), " *Chemical Physics Letters* **186(4,5)**, 450, (1991).

[32] C.K. Mathews, M. Sai Baba, T.S. Lakshmi Narasimhan, R. Balasubramanian, N. Sivaraman, T.G. Srinivasan, and P.R. Vasudeva Rao, "Vaporization Studies on Buckminsterfullerene," *Journal of Physical Chemistry* **96**, 3566, (1992).

[33] C. Pan, M.S., Chandrasekharaiah, D. Agan, R.H. Hauge, and J.L Margrave, "Determination of Sublimation Pressures of C_{60}/C_{70} Solid Solution," *Journal of Physical Chemistry* **96(16)**, 6752, (1992).

Chapter 4

FTIR Studies of C_{60}

4.1 Introduction

Determination of the purity of fullerene samples is vital when investigating their degradation at elevated temperatures. It is important to assess whether decomposition is due to catalytic or stoichiometric reactions with contaminants, or unimolecular decomposition. The presence of contaminants also poses problems for ion thruster applications where impurities such as CO or O_2 could reduce propellant utilization efficiency, create a nonuniform mass distribution of expelled ions, and erode or react with thruster components.

One particularly sensitive technique for analyzing C_{60} purity, reaction products, and yields in crude fullerene soot extracts in the solid state is Diffuse Reflectance Infrared Fourier Transform (DRIFT) spectroscopy. The DRIFT technique is very sensitive to impurities and weak spectral features [1].

The infrared absorption spectrum of C_{60} is dominated by four dipole-active (F_{1u}) peaks located at 527, 576, 1183, and 1429 cm^{-1}. In addition, there are numerous combination modes, ^{13}C isotope-allowed, and crystal field-activated fundamental modes which appear as weaker features in the spectrum. However, a few of these weaker features at 2349, 2328, and 1539 cm^{-1} have stood out as having much higher amplitude than all of the others, and they have accordingly drawn more attention.

Krätschmer and co-workers [2] published an IR absorption spectrum of C_{60} over the 3200 to 400 cm^{-1} range in which several lower-intensity peaks were specifically noted. They stated "Weaker features at 2330 and 2190 cm^{-1} located in the vicinity of the free CO_2 and CO stretching modes, may imply some attachment of the CO_2 or CO to a small fraction of the total number of C_{60} molecules." Kamaras and coworkers also attributed the features in the 2330 cm^{-1} region to CO_2 antisymmetric stretches [3]. Since the initial assignment of these peaks to contamination, numerous studies of both the vibrational spectrum of C_{60} [4]-[10] and of various adsorbates on C_{60} [11]-[15] have been reported.

Examination of CO_2 adsorption on C_{60} at various temperatures and pressures [11,12,14] has shown consistent appearance of a CO_2 spectral feature at 2328 cm^{-1}. An additional feature at 2349 cm^{-1} was attributed to CO_2 on KBr by Heidberg *et al.* [11], though it appears in spectra of neat C_{60} samples as well (see Figure 4.1). It is not due to gas phase CO_2 which would aquire rotationally split P and R branches offset from 2349 cm^{-1}, nor could it be from frozen CO_2 which has peaks at 2345.3 and 2342.3 cm^{-1} for crystalline and amorphous CO_2, respectively [16]. Fastow *et al.* [12] and Nagano *et al.* [14] do not report the 2349 cm^{-1} peak. Heidberg also finds features at 2332, 2344, and 2380 cm^{-1} appearing at various CO_2 pressures.

Uptake of O_2 by C_{60} also has been extensively studied [15,17]. It has been suggested [3,17] that the O_2 stretching mode at 1555 cm^{-1} is made IR active by clathrate-type in-

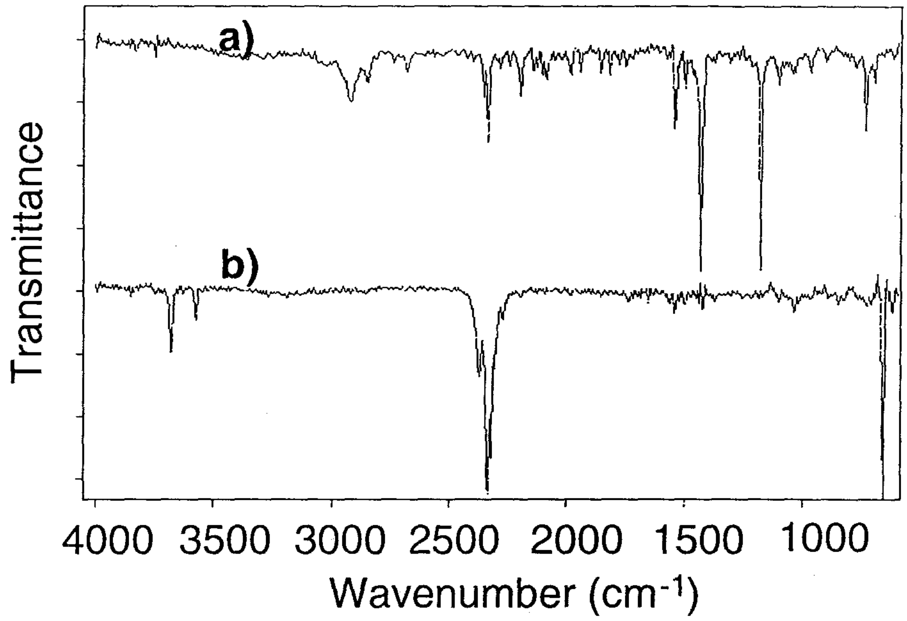

Figure 4.1: a) untreated C_{60} and b) CO_2 adsorbed on C_{60}.

tercalation in C_{60} crystals. Kamaras *et al.* [3] attributes the 1539 cm^{-1} feature in the IR spectrum to this phenomena, while Werner *et al.* [17] explains a 1385 cm^{-1} feature (not seen elsewhere) in this way. Though this explanation seems plausible, there is still the question of why the ratio of the 1539 cm^{-1} peak amplitude to that of the dipoles appears constant in all published IR spectra. Werner assigns the 1539 cm^{-1} feature to a C-H vibration of $(CH_2)_x$ derivatives — an assignment which is curious because C-H vibrational modes are not typically found in this region, and it is unlikely that the accompanying C-H stretches would be suppressed. When CO_2 is chemisorbed on metals, spectral features are found in the 2200, 1550, and 1380 cm^{-1} regions [18]. CO_2 bonded to a metal oxide (carbonate-type bond) results in the 1380 cm^{-1} feature, while the carbon atom of the CO_2 bonded to the metal results in the 1550 cm^{-1} feature. It may be hypothesized that the peak at 1385 cm^{-1} observed by Werner *et al.* [17] is attributable to the former mechanism.

Assignment of the vibrational modes of C_{60} has been made by observing the IR spectra of C_{60} films [8,4] and single crystals [5]. Spectra and peak tables of all IR spectral features found for powdered C_{60} and C_{70} are shown in Appendix B. The C_{60} peak locations are compared with those identified in other studies [4,5]. Many fundamental and combination modes appear to be made weakly IR active by crystal field effects [6]. The features at 2328, 2349, and 1539 cm^{-1} have all been assigned combination modes. The intensity of these peaks is substantially larger than the other assigned combination modes. Though the relatively high peak intensity of the 1539 and 2328 cm^{-1} features are not discussed, Wang *et al.* [4] mention that they have not considered the effect of Fermi resonance in their study.

Martin *et al.* [5] assigns the features at 1539, 2349, and 2328 cm^{-1} to the $G_g(2) \otimes H_u(2)$, $G_g(6) \otimes G_u(3)$, and $H_g(8) \otimes G_u(3)$ combinations respectively, while Wang *et al.* [4] assigns the same peaks to $F_{1g}(2) \otimes H_u(2)$, $G_u(3) \otimes H_g(7)$, and $G_g(5) \otimes G_u(4)$, respectively. The discrepancy in the assignments results from different values found for the fundamental vibrational frequencies. Table 4.1 shows seven fundamentals whose assignments are somewhat ambiguous. There is obviously some confusion surrounding the assignment of combination modes, CO_2 and O_2 contamination features of C_{60}. The presence of adsorbates which are difficult to remove, and for which C_{60} has a strong affinity, is an important issue for researchers attempting to determine properties intrinsic to *pure* C_{60}. Here, the IR spectra of both solid fullerene and C_{60} dissolved in various solvents in the 4000 to 550 cm^{-1} range are reported. The quantity and mechanism of CO_2 attachment is investigated, and a determination of whether combination modes of C_{60} or contaminants are responsible for the observed features is made.

Mode	Ref. [4]	Ref. [5]	Ref. [9]	Ref. [10]	Ref. [7]
$H_u(2)$	563	579	543	—	530
$G_g(5)$	1356	1345	1375	1441	1322
$G_u(4)$	970	1080	961	1036	975
$G_u(3)$	924	753	929	830	782
$G_g(2)$	621	961	626	617	566
$G_g(6)$	1524.5	1596	1521	—	1512
$G_u(2)$	760	739	789	—	748

Table 4.1: Seven of the fundamental modes of C_{60} and their assignments.

4.2 Solid C_{60} Spectra

For DRIFT measurements of powder samples from 4000 to 550 cm^{-1}, an Analect Rfx-40 FTIR spectrometer with a MCT (Hg-Cd-Te) LN cooled detector was used. The spectrometer was equiped with a biconical diffuse reflectance accessory. The 4.0 cm^{-1} resolution spectra were collected with 256 coadded scans relative to a powdered KBr standard. A BioRad Digilab FTS-90 infrared spectrometer for high (0.3 cm^{-1}) resolution spectra was also utilized.

Modification of the features at 2349, 2328, and 1539 cm^{-1} was first attempted by conventional thermal annealing; spectra of C_{60} samples heated to 500 K for 16 hours and to 583 K for 22 hours in vacuo showed no change in any of these features. Also, there was no evidence of the formation of cyclic anhydrides in the 1800-1000 cm^{-1} region which would be indicative of oxidation [19].

If the peaks observed at 2328 and 2349 cm^{-1} are due to CO_2 contamination, then it is possible to quantify the amount by normalizing the peak intensity to a CO_2 standard. Using the FTIR absorption spectrum of C_{60} published by Chase, Herron, and Holler for a 15 mm thick film [8], the intensity of the 2328 cm^{-1} peak was normalized to that of gaseous CO_2 in air in a 10 cm path length gas cell. A CO_2 density of 0.046% was assumed. If the feature seen in the C_{60} spectrum is due to CO_2, then its amplitude corresponds to a CO_2 content of approximately 0.7% by weight — a surprisingly large quantity which would indicate a molecular sieve effect by C_{60}.

Reports of supercritical CO_2 treatment of C_{60} showed an uptake of 5% by weight [14]. Ismail and Rodgers [15] found that the uptake of CO_2 at 298 K by C_{60} was more than three orders of magnitude higher than that of N_2 or O_2 at 77 K.

The CO_2 content in C_{60} could also be increased in the present study by exposure to a flow of CO_2. Allowing the sample to slowly degas under N_2 provided a reference. The resulting spectrum showed both adsorbed CO_2 and gas-phase CO_2 outgassing from the sample in the spectrometer, as evidenced by the apparent rotational structure (see Figure 4.2). The gas-phase CO_2 signal was then subtracted from the spectrum; the result is shown in Figure 4.1b and 4.3b. There are three distinct peaks in the CO_2 antisymmetric stretching region at 2377, 2330, and 2316 cm^{-1}, which may correspond to different bonding mechanisms of the CO_2 on C_{60}. The different mechanisms may pertain to the location of the CO_2 at either octahedral or tetrahedral voids in the FCC lattice. Note that two of these peaks occur close to the 2332 and 2380 cm^{-1} features observed by Heiberg *et al.* [11]. Also evident is the CO_2 bending mode 654 cm^{-1} and overtones at 3681 and 3576 cm^{-1}. Note that neither the bending nor the overtone modes appear in the untreated fullerene sample. To ascertain whether the 1539 cm^{-1} peak is due to O_2 intercalation, fullerenes were placed under a

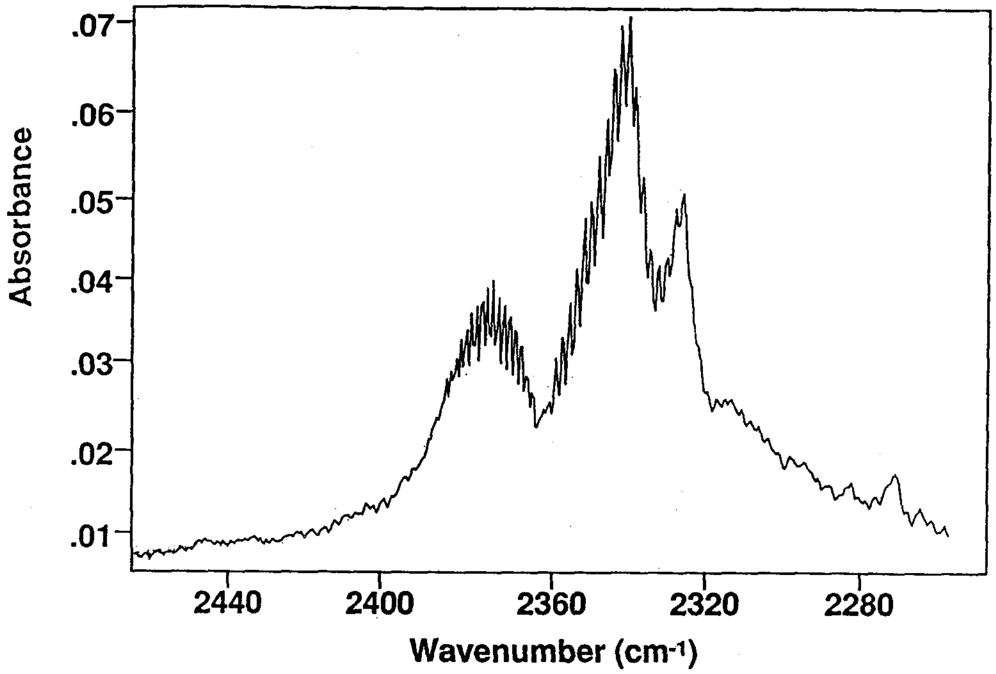

Figure 4.2: Infrared spectrum of CO_2 adsorbed on C_{60} in the CO_2 stretch region prior to subtraction of the gas-phase component. The resolution is 0.3 cm^{-1}.

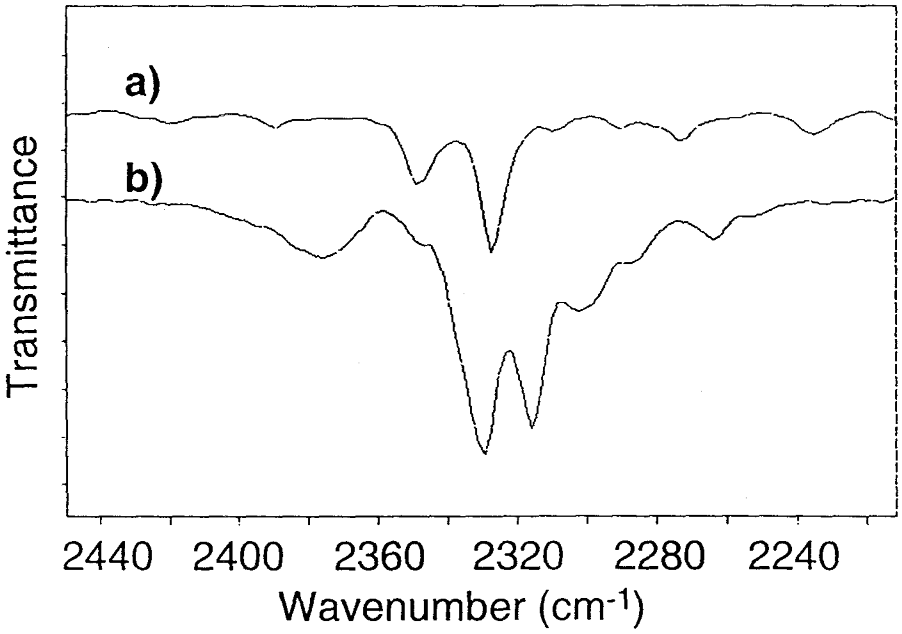

Figure 4.3: CO_2 adsorbed on C_{60} in the antisymmetric stretch region a) C_{60}, b) adsorbed CO_2.

flow of pure O_2. The spectrum of the O_2-treated material showed no change. However, it was found that subsequent treatment of the oxygen-saturated material with CO_2 showed that it did not absorb as much CO_2 as the samples that had not been exposed to oxygen, suggesting that many of the adsorption sites had been occupied.

Because of both the difference in peak locations of the adsorbed CO_2 from the peaks in question and the lack of CO_2 bending and overtone modes, it was doubtful that the fullerene samples contained nearly 1% CO_2 by weight. An examination of dissolved C_{60} was initiated to further investigate the origin of the peaks.

4.3 C_{60} in Solution

To more precisely determine the CO_2 content of fullerene samples, 0.05 N NaOH aqueous solution was extracted from C_{60} in toluene and back-titrated with 0.05 N HCl solution. A comparison was made with the back-titration of NaOH extracted from blank toluene. There was no difference in the NaOH content of the solutions within the experimental uncertainty — a number corresponding to less than 0.2% CO_2.

The mixed fullerenes were then dissolved in carbon tetrachloride and tetralin to observe the effect on the features at 2328 and 2349 cm^{-1}. The 1539 cm^{-1} peak was monitored in 1,1,2,2 tetrabromoethane in which C_{60} is highly soluble because of its similarity to 1,1,2,2 tetrachloroethane [20]. Figure 4.4 shows the IR spectrum of mixed fullerene in CCl_4 extracted 1:1 with an aqueous 0.05 N NaOH solution to scavenge the CO_2 dissolved in the CCl_4. A 5 mm path length cell was used at 4 cm^{-1} resolution. The two features at 2349 and 2328 cm^{-1} have shifted by 3 wavenumbers to higher frequency at 2352 and 2331 cm^{-1}, respectively. Chase *et al.* [8] studied fullerenes in CS_2 and reported the solvent-induced

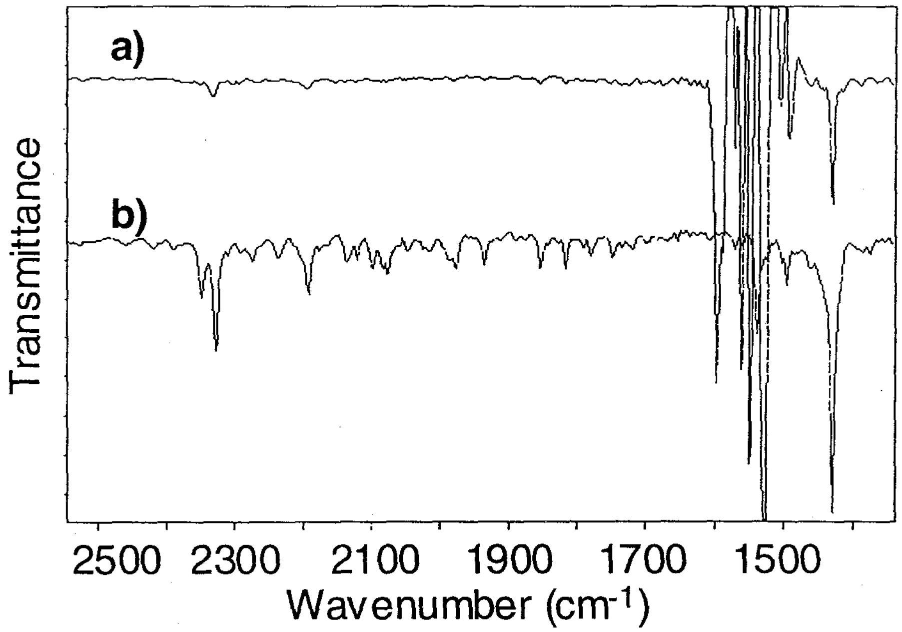

Figure 4.4: C_{60} a) solid and b) dissolved in carbon tetrachloride.

shifts of the four dipole peaks. For the 526 and 576 cm^{-1} modes, the shift was 1.7 cm^{-1} to higher frequencies in each case, and was less than 0.7 cm^{-1} to lower frequency for the 1183 and 1429 cm^{-1} modes. No shift of the 1429 cm^{-1} peak in either CCl_4 or 1,1,2,2 tetrabromoethane was observed in these experiments.

Unlike the features in the CO_2 stretching region, the peak at 1539 cm^{-1} dissappeared in the dissolved C_{60}, as noted by Werner *et al.* [17] (see Figure 4.5). Upon drying C_{60} in either methylene chloride or CCl_4 mixed with KBr in the spectrometer under dry nitrogen, all features in question reappeared with their original intensity.

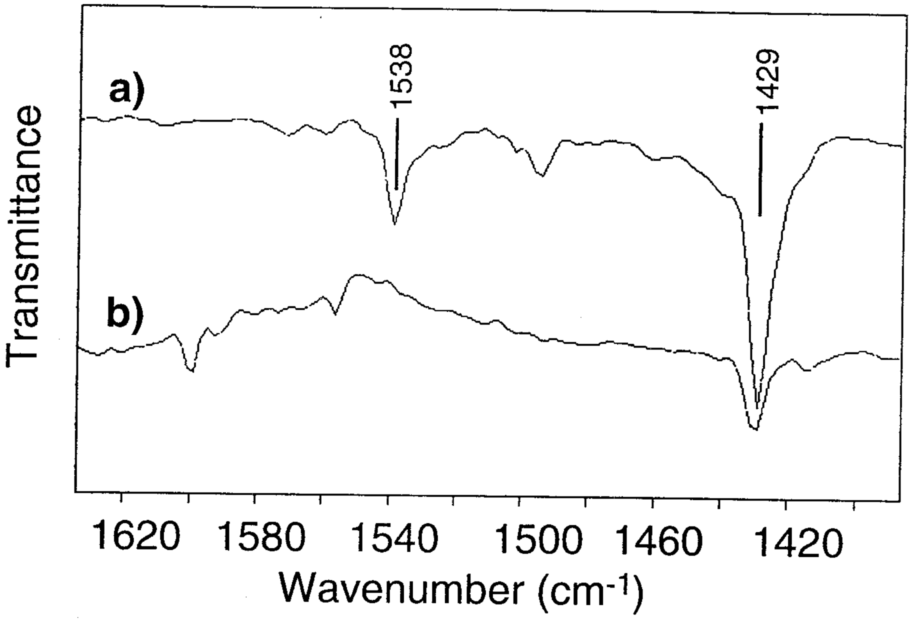

Figure 4.5: C_{60} a) solid and b) dissolved in 1,1,2,2 tetrabromoethane.

4.4 Anomolous Peak Intensities

The theory that the 1539 feature is also due to a combination mode was examined. It was noted that C_{60} has a fundamental vibration at 1526 cm^{-1} attributed to $G_u(6)$ by Martin *et al.* [5]. This assignment is supported in vibrational studies of C_{60} by other techniques [10, and references therein]. In the solid state, a Fermi resonance effect may occur if a combination contains the symmetry of a nearby fundamental. Wang *et al.* assigns the 1539 cm^{-1} feature to the $F_{1g}(2) \otimes H_u(2)$ combination, where both of these fundamentals are well known. This product has $F_{1u} \oplus F_{2u} \oplus G_u \oplus H_u$ symmetry (the direct product table for the icosahedral group, I_h is found in Appendix B), and thus contains the symmetry of the 1526 cm^{-1} fundamental. It is IR active because it contains F_{1u} symmetry.

Because there are no fundamental vibrational modes of C_{60} at wavenumbers higher than

1600 cm^{-1}, the intensity of the peaks seen in the CO_2 stretching region of the spectrum can not be explained by a Fermi resonance effect. However, these combination modes are expected to be IR active.

Both of the mechanisms which may be responsible for the appearance of the 1539 cm^{-1} feature (crystal field effects and Fermi resonance) can be destroyed by a solvent interaction. Though no change was observed in the 1539 cm^{-1} feature when the sample was cooled below the orientational order/disorder transition temperature, a crystal field effect may still be responsible, as reported by Martin *et al.* [6]. That the 2328 and 2349 cm^{-1} features remain visible (albeit shifted) in solution indicates that they are activated by a different mechanism than the 1539 cm^{-1} feature.

4.5 Conclusions

Werner [17] notes that once exposed to air, C_{60} samples are irreversibly modified. Concentrations of O_2 as low as 2 ppm in nitrogen were enough to observe O_2 intercalation in the fullerite. Other modifications of solid fullerite by photo-induced polymerization have also been reported [22]. However, the peaks discussed above appear identical in all reported spectra regardless of sample preparation, and are not modified any differently than the dipole features are in polymerized samples. The possibility of the existance of an acetylenic resonance structure of C_{60} in the solid phase was investigated by comparing the IR spectra with those of capped acetylenic carbon chains reported by Lagow and coworkers [23]. Though triple-bonded carbon displays vibrations in the 2200 and 1600 cm^{-1} range, there was no match with the C_{60} peaks. These observations lead to the conclusion that the peaks seen in the IR spectrum of C_{60} are due to either contamination or vibrational modes of the fullerenes. The findings of this study indicate that contamination is not the cause.

Two factors have probably contributed to the confusion surrounding this issue. The first is that oscillator strengths for combination modes are difficult to predict. The features discussed in this chapter are much more prominent than the other combination modes of C_{60}, and have accordingly drawn more attention. The second factor is the closeness of the 2328 and 2349 cm^{-1} features to the commonly observed CO_2 stretching mode. Few other materials show strong absorption features in this region.

In summary, it has been shown that the features commonly observed at 2328, 2349, and 1539 cm^{-1} in the IR absorption spectrum of C_{60} are intrinsic to the molecule. Further, new features corresponding to various bonding mechanisms of CO_2 on C_{60} have been identified. Further work in this area may include studies of isotopically pure ^{13}C fullerenes.

The results of this study relieve some concern over propellant contamination for fullerene ion thrusters. Though fullerenes do tenaciously hold solvents in the solid state which must be removed by thermal annealing in vacuo, their affinity for CO_2 is not so great as one may have expected from infrared spectroscopic evidence. IR spectroscopy has provided a valuable tool for confirming that the cause of fullerene thermal disintegration investigated in the last chapter is not sample contamination.

References

[1] M.P. Fuller and P.R. Griffiths, "Diffuse Reflectance Measurements for Infrared Fourier Transform Spectrometry," *Analytical Chemistry* **50(13)**, (1978).

[2] W. Krätschmer, L.D. Lamb, K. Fostiropoulos, and D. Huffman, "Solid C_{60}: a New Form of Carbon," *Nature* **347**, 354 (1990).

[3] K. Kamaras, L. Akselrod, S. Roth, A. Mittelbach, W. Honle, and H.G. von Schnering, "The Orientational Phase Transition in C_{60} Films Followed by Infrared Spectroscopy," *Chemical Physics Letters* **214(3-4)**, 338 (1993).

[4] K.A. Wang, A.M. Rao, P.C. Eklund, M.S. Dresselhaus, and G. Dresselhaus, "Observation of Higher-Order Infrared Modes in Solid C_{60} Films," *Physical Review B* **48(5)**, 11375 (1993).

[5] M. Martin, X. Du, J. Kwon, and L. Mihaly, "Observation and Assignment of Silent and Higher-Order Vibrations in the Infrared Transmission of C_{60} Crystals," *Physical Review B* **50(1)**, 173 (1994).

[6] M. Martin, J. Fabian, J. Godard, P. Bernier, J.M. Lambert, and L. Mihaly, "Vibrational Study of ^{13}C-enriched C_{60} Crystals," *Physical Review B* **51(5)**, 2844 (1995).

[7] P. Giannozzi and S. Baroni, "Vibrational and Dielectric Properties of C_{60} from Density-Functional Perturbation Theory," *Journal of Chemical Physics* **100(11)**, 8537 (1994).

[8] B. Chase, N. Herron, and E. Holler, "Vibrational Spectroscopy of C_{60} and C_{70} Temperature Dependent Studies," *Journal of Physical Chemistry* **96(11)**, 4262 (1992).

[9] R.A. Jishi, R.M. Mirie, and M.S. Dresselhaus, "Force-Constant Model for the Vibrational Modes in C_{60}," *Physical Review B* **45(23)**, 13685 (1992).

[10] J.L. Brousseau, K. Tian, S. Gauvin, R.M. Leblanc, and P. Delhaes, "Interfacial and Vibrational Properties of Thin Films of C_{60}," *Chemical Physics Letters* **202(6)**, 521 (1993).

[11] J. Heidberg, J. Elstner, W. Lassmann, and M. Folman, "Polarized FTIR - Spectra of C_{60} Layers and the Adsorbates of CO and CO_2 on C_{60}," *Journal of Electron Spectroscopy and Related Phenomena*, **64/65**, 883 (1993).

[12] M. Fastow, Y. Kozirovski, and M. Folman, "IR Spectra of CO_2 and N_2O Adsorbed on C_{60} and Other Carbon Allotropes - a Comparative Study," *Journal of Electron Spectroscopy and Related Phenomena* **64/65**, 843 (1993).

[13] M. Fastow, Y. Kozirovski, M. Folman, and J. Heidberg, "IR spectra of CO and NO Adsorbed on C_{60}," *Journal of Physical Chemistry* **96**, 6126 (1992).

[14] Y. Nagano, T. Kiyobayashi, and T. Nitta, "CO_2 Adsorption in C_{60} Solid," *Chemical Physics Letters* **217(3)**, 186 (1994).

[15] I.M.K. Ismail, and S.L. Rodgers, "Comparison Between Fullerene and Forms of Well-Known Carbon," *Carbon* **30(2)**, 229 (1992).

[16] M. Falk and P.F. Seto, "Infrared Spectra of Solid Carbon Dioxide," *Canadian Journal of Spectroscopy* **31(5)**, 134 (1986).

[17] a) H. Werner, T. Schedel-Niedrig, M. Wohlers, D. Herein, B. Herzog, R. Schlogl, M. Kell, A.M. Bradshaw, and J. Kirschner, "Reaction of Molecular Oxygen With C_{60}: Spectroscopic Studies," *Journal of the Chemical Society Faraday Transactions* **90(3)**, 403 (1994), b) H. Werner, D. Bublak, U Gobel, B. Henschke, W. Bensch, R. Schlogl, "Material Properties and Purity of C_{60}," *Angewandte Chemie: International Edition in English* **31(7)**, 868 (1992).

[18] L.H. Little, "Infrared Spectra of IR Species," 66-67 Academic Press, London (1966).

[19] A.M. Vassallo, L.S.K.. Pang, P.A. Cole-Clarke, and M.A. Wilson, "Emission FTIR Study of C_{60} Thermal Stability and Oxidation," *Journal of the American Chemical Society* **113**, 7820 (1991).

[20] R.S. Ruoff, D.S. Tse, R. Malhotra, and D.Lorents, "Solubility of C_{60} in a Variety of Solvents," *Journal of Physical Chemistry* **97**, 3379 (1993).

[21] J.C. Dobrowolski and M.H. Jamroz, "Infrared Evidence for CO_2 Electron Donor-Acceptor Complexes," *Journal of Molecular Structure* **275**, 211 (1992).

[22] A.M. Rao, P. Zhou, K. Wang, G. Hager, J. Holden, Y. Wang W.T. Lee, X. Bi, P.C. Ecklund, D.S. Cornett, M.A. Duncan, and I.J. Amster, "Photoinduced Polymerization of Solid C_{60} Films," *Science* **259**, 955 (1993).

[23] a) R.J. Lagow, J.J. Kampa, H. Wei, S.L. Battle, J.W. Genge, D.A. Laude, C.J. Harper, R. Bau, R.C. Stevens, J.F. Haw, and E. Munson, "Synthesis of Linear Acetylenic

Carbon: the *sp* Carbon Allotrope," *Science* **267**, 362 (1995), b) R.J. Lagow, University of Texas at Austin, Personal Communication (1995).

Chapter 5

Electron Impact Ionization and Dissociation of C_{60}

5.1 Introduction

For ion source applications, the ionization potential and cross section for ionization by electron impact play an important role in the ion production cost within the plasma. Since 1990, an abundance of work in the field of fullerene ionization and fragmentation has been conducted. Many investigators have reported on the ionization of C_{60} by electron impact [1]-[15]. Some of these reports have been on appearance potentials for various fullerene ions and fragment ions [4]-[15], while others have been for fullerene ionization cross sections [1,2,3].

C_{60} is remarkable because it readily forms both positive and negative ions, and long lived multiple ions — up to C_{60}^{6+} [16]. That these multiply charged species do not succumb to coulomb explosion is a testimony to their aromatic nature.

In the following pages, both predicted and experimentally determined values of the electron impact ionization cross sections of C_{60} are presented. Experiments with a time-of-flight (TOF) mass spectrometer used to determine fragmentation patterns and ion appearance potentials, as well as the ionization cross section, are described.

5.2 Estimates for the Ionization Cross Section of C_{60}

Two methods of estimating ionization cross sections of organic molecules have been applied to C_{60}. One of these methods correlates the ionization cross section with the number of carbon atoms in an organic molecule. The second method correlates the ionization cross section with molecular polarizability. A detailed study of both methods to estimate the ionization cross section of C_{60} was made by Rapp and Leifer [17].

5.2.1 Atomic Contributions to Molecular Ionization Cross Sections

Several investigators have measured the cross sections for large molecules (up to 10 carbon atoms) and analyzed these results in terms of additivity rules. Otvos and Stevenson were the first to postulate that in large molecules, the ionization cross sections can be estimated by means of an additivity principle [18] in which one sums the contributions from the valence electrons of the various atoms in a molecule. They tested this hypothesis by estimating the atomic contributions from an approximate estimate of their spatial distributions, and measuring the ionization cross sections for a number of molecules. Lampe, Field, and Franklin [19] made new ionization cross section measurements, and found results which differed from those of Otvos and Stevenson. Harrison, Jones, Gupta and Nagy [20] remeasured the ionization cross sections of the molecules in the previous studies, and measured the cross sections for quite a few additional molecules. Their results agree much more closely with Lampe, Field, and Franklin than with Otvos and Stevenson. Mann [21] improved upon the basic theoretical method of Otvos and Stevenson for estimating atomic contributions. Beran and Kevan [22] measured ionization cross sections for 62 carbonaceous molecules at 70 eV. They used the same method as Lampe, Field, and Franklin and Harrison *et al.*

Based on data for 18 hydrocarbons, Lampe, Field, and Franklin [19] found the contribution of a CH_2 group to the cross section of a molecule to be 2.6×10^{-16} cm^2. This value is renormalized to the cross section for argon measured by Rapp and Englander-Golden [16]. They assumed that the contribution of an H-atom to the cross section of a hydrocarbon is half that of H_2, and thus chose the value 0.5×10^{-16} cm^2 for H. They then derived the contribution of a C-atom to the cross section to have the renormalized value of 1.6×10^{-16} cm^2.

Harrison, Jones, Gupta and Nagy [20] studied a number of homologous series of organic molecules and found that when the cross sections were plotted as a function of the number of carbon atoms, each family could be fitted by a straight line, and the lines were all parallel. From the slopes of the lines, they concluded that the contribution of each additional CH_2 group to the renormalized cross section is 2.2×10^{-16} cm^2. Mann's study indicates that the cross section for C is approximately 4 times that of H, and therefore the value 2.2×10^{-16} cm^2 for the CH_2 group should be divided as (2) $H = 0.7\times10^{-16}$ cm^2 and $C = 1.5\times10^{-16}$ cm^2. It would therefore appear from this data that the best value for the contribution of a carbon atom to the ionization cross section of a large molecule is approximately $1.5\pm 0.2\times10^{-16}$ cm^2. Therefore, the peak ionization cross section of C_{60} may be approximately 90×10^{-16} cm^2.

5.2.2 Correlation With Polarizability

Beran and Kevan [22] correlated ionization cross sections with molecular polarizabilities. The correlation is based on the fact that both the polarizability and the ionization cross section are dependent upon the dipole moment matrix elements for the molecule. For hydrocarbons, a good correlation could be made as:

$$\sigma = 0.15\chi_m \tag{5.1}$$

where the ionization cross section is σ in units of 10^{-16} cm^2, and the molecular polarizability χ_m is in units of 10^{-25} cm^3. This correlation is similar to the one proposed by Lampe, Field, and Franklin [19] who gave the relation as:

$$\sigma = 0.18\chi_m \tag{5.2}$$

for ionization cross sections at 70 eV.

However, Harrison *et al.* [20] note that the correlation with polarizability is only accurate within a homologous series of molecules, and the slope of the cross section-polarizability line is dependent upon this series. Therefore, it is questionable as to which family, if any, C_{60} is most closely related for the application of this correlation.

The polarizability of C_{60} was theoretically predicted by Fowler *et al.* [24]. The most advanced calculation yielded a value of χ_m=655$\times10^{-25}$ cm^3. The estimated ionization cross section based on this polarizability is 98$\times10^{-16}$ cm^2. More recently, C_{60} polarizability has been measured experimentally [25]-[27]. Though these values vary somewhat, they converge upon a polarizability closer to 850$\times10^{-25}$ cm^3 (see Appendix C). This value would imply a cross section for C_{60} of 128$\times10^{-16}$ cm^2.

5.3 Experimental

There are several advantages to using a time-of-flight (TOF) mass spectrometer for this study. One is that the transmission efficiency of the apparatus can be made independent of the particle charge-to-mass ratio in a well designed system [28]. Another is that a TOF system can record all ion intensities simultaneously, such that changes in the ion source conditions do not affect the relative intensity of ions with different charge-to-mass ratios. TOF mass spectrometers are also relatively inexpensive and simple to construct. Disadvantages of TOF systems include poor resolution of high mass-to-charge ratio species, and an inability to accurately analyze ions which possess large initial kinetic energy.

5.3.1 Apparatus

A crossed electron beam - molecular beam collision geometry was employed for the study of fullerene ion formation. A fullerene mix containing approximately 80% C_{60} and 20% C_{70} was heated in a stainless steel crucible. Fullerene vapor effused from a pinhole in the top of the crucible. Most of the spectra were obtained at a crucible temperature of 673 K. A magnetically-collimated electron gun was used to produce an electron beam with an energy variable between 3 and 1000 eV. The uncertainty in the electron energy was 0.5 eV. The electron beam was pulsed with a Wavetek model 801 pulse generator at 5 kHz with a pulse width of 0.5 μs. The pulsed electron beam was crossed perpendicularly to the effusing molecular beam; resulting ions were extracted from the collision region perpendicular to both the electron and molecular beams. The ion extraction grid was biased between -22 and -28 V relative to ground to establish an extraction field. This field was pulsed for 1 μs duration such that the environment around the collision region was field-free during the electron beam pulse. The ion extraction grid was the entrance to the gold-coated copper 0.4 m flight tube of a time-of-flight mass spectrometer which was biased to −310 V. After passing through the field-free region of the flight tube, ions were detected by a spiraltron biased to −3 kV relative to ground potential. Ion flight-times were on the order of tens of microseconds. The spiraltron converted detected ions to electrical pulses which were amplified and used as the stop signal for a Time-to-Pulse-Height Converter (TPHC) (EG&G model 567 TAC/SCA). The start signal was supplied by the electron beam pulse. Thus, the ion time-of-flight was measured by the TPHC. The TPHC supplied a signal proportional to the total time of flight and any delay to an EG&G Ortec pulse height analyzer (PHA), or multichannel scalar (MCS) bus in an IBM compatible computer. Figures 5.1, 5.2, and 5.3 show a schematic diagram, an electrical diagram, and a photograph of the collision region of the apparatus, respectively. The vacuum was in the low 10^{-7} Torr range during data collection, with a base pressure of approximately 6×10^{-8} Torr in the absence of test gases. Pumping was accomplished with a Balzers model TPH 1500 turbomolecular pump.

The filament current for the electron gun was 2.2 to 2.3 A. This typically supplied a steady-state focussed electron beam current of about 6 μA detected at a Faraday cup connected to a Keithley model 610B electrometer. Although the potentials on the focussing lenses of the electron gun were adjustable to allow a relatively constant beam current with changing electron energy, this quantity still varied somewhat, as did the electron beam focus. The variation of electron beam focus as a function of electron energy is shown in Figure 5.4. The faraday collector current refers to that current passing through the cup aperture, while the cup current refers to the current impinging on the faraday cup

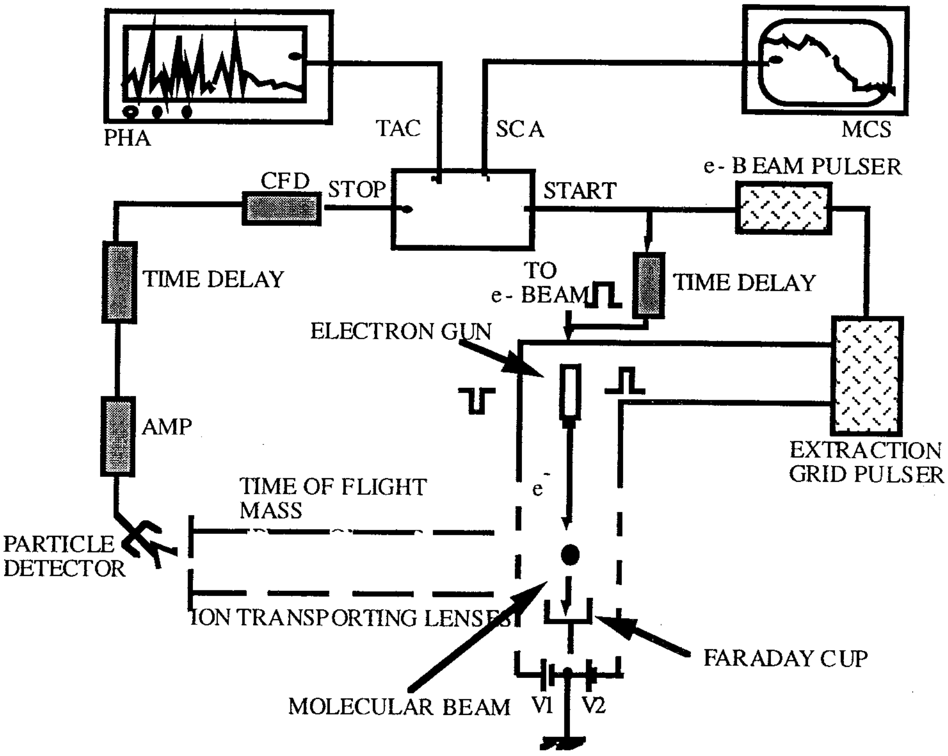

Figure 5.1: Experimental apparatus for the determination of ionization and dissociative ionization cross sections. A molecular beam is crossed at 90 degrees with an electron beam. The resulting ions are extracted perpendicular to both beams and analyzed in the time-of-flight mass spectrometer.

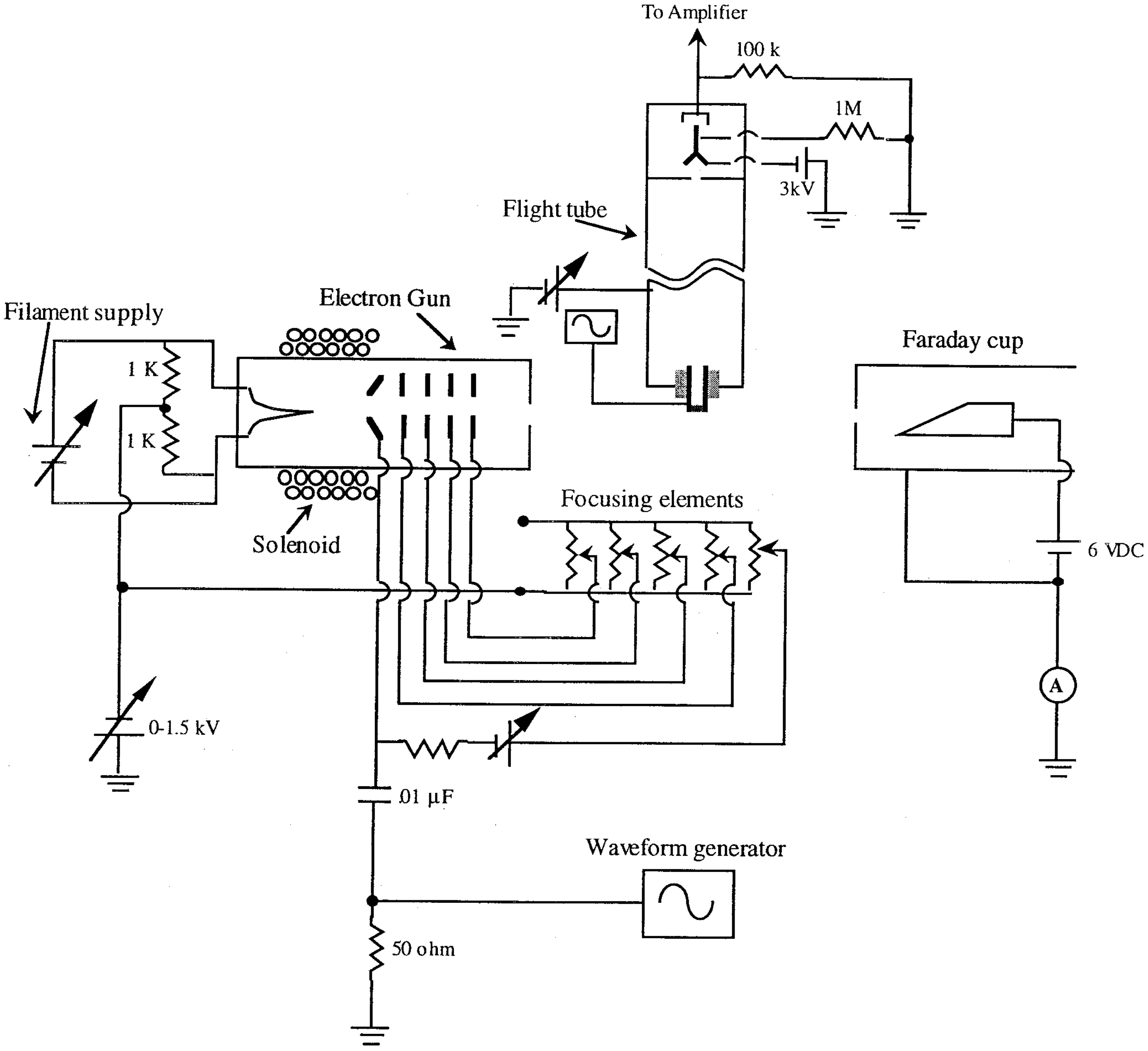

Figure 5.2: Electrical diagram of the time-of-flight mass spectrometer.

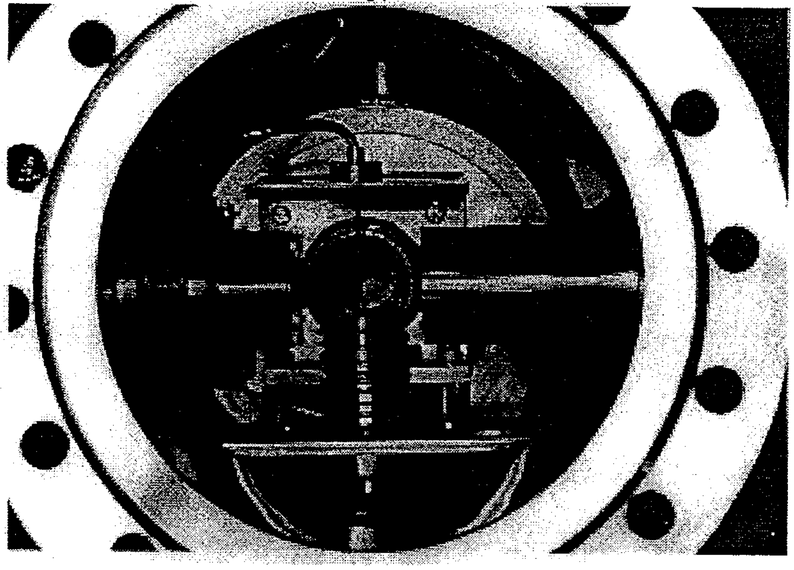

Figure 5.3: A view of the mass time-of-flight mass spectrometer collision region. The electron gun is at the left, a faraday cup at the right, effusive cell at the bottom, and ion repeller plate at the rear. A tube inlet for a test gas is seen extending down from the top.

casing. It was necessary to perform electron gun calibrations to ascertain the amount of ion peak variation due to this effect. The mass resolution of the apparatus is dependent upon several factors. Resolution increases as the size of the electron-molecule collision region decreases. This is due to the narrowing of the spread in flight times resulting from various path lengths for ions created in different portions of the collision region. Thus, at higher electron energies, resolution is improved because of better electron beam focusing. The length of the flight tube is also very important; longer flight tubes result in longer particle time-of-flight, thus giving larger separation between arrival times of different mass-to-charge-ratio species. Flight tube and extraction grid voltages affect ion trajectories; the voltages are varied to maximize the ion current detected at the spiraltron. Other factors that decrease spectral resolution [29] are space charge effects, inhomogeneous electric fields,

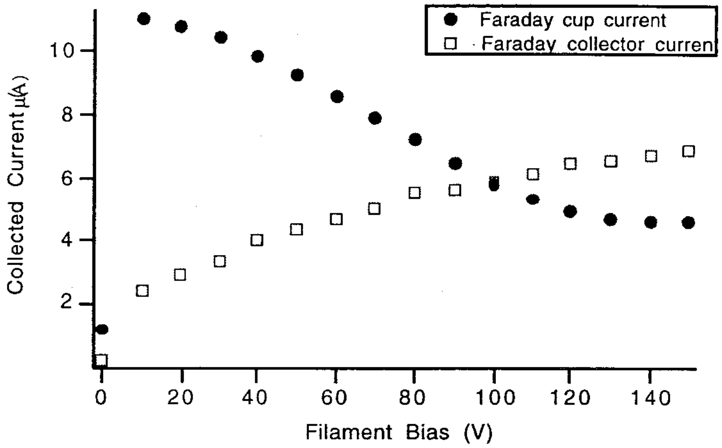

Figure 5.4: Faraday cup current as a function of electron energy.

poor electron beam pulse characteristics, and the initial distribution of ion velocities. The highest mass resolution ($M/\Delta M$) attainable with this apparatus at large mass under the operating conditions described above was approximately 70. This was high enough to distinguish increments of single carbon atoms (12 amu), but is by no means high resolution.

5.3.2 Cracking Patterns

Cracking patterns (plots of intensities of ionic fragments as a function of their masses) of C_{60} were observed at various electron impact energies. Because the PHA is multichannel in energy, but single channel in time, it is used to determine the relative intensities of all of the ions created. Multiple ions of C_{60} through C_{60}^{4+} were evident in the spectra. Only even numbered fragments were observed (C_{58}, C_{56}, C_{54}, etc...) at electron energies above 70 eV. It has been reported by Foltin *et al.* [8] that fragmentation starts in the energy range above 40 eV. An ion engine operating with C_{60} propellant would likely use primary electrons with energies between 20 and 30 eV, making fragmentation from a single-collision event unlikely.

Figures 5.5 to 5.7 shows fullerene mass spectra at electron impact energies of 40 to 300 eV. Double and triple fullerene ions are evident in the spectra. The mass spectra show that the process of dissociative ionization is favored for multiply charged fullerenes over the singly ionized species. This is especially evident at electron energies greater than 100 eV. It is notable that the tail portion of the C_{60} peak increases with higher electron energy. Because there is no structure evident in this region indicative of fragmented C_{70} molecules, it is possible that delayed ionization of C_{60} is occurring.

Delayed ionization of C_{60} on the microsecond timescale has been observed by several researchers [30]-[33]. Though some uncertainty exists over whether the delayed ionization results from thermionic emission or long-lived electronic excitation [33], Gallogly and coworkers [30] performed detailed time-of-flight measurements that showed excited neutrals were being field ionized in the detector region of their apparatus. Because the field strength near the detector was not very large, this evidence supports the notion that excitation of long-lived Rydberg states, and not vibrational excitation is responsible. They found that the excited states leading to delayed ionization had an appearance potential of 32 eV.

5.3.3 Ionization Function Curves

When the data from the spiraltron amplifier was routed to the MCS, one ion species was chosen at a time. The variation of the peak height (ion intensity) with the energy of the ionizing electrons was observed. A plot of this data is called the ionization function curve.

Though ionization function curves provide relative cross sections for ionization, they must be normalized to provide absolute cross sections. The absolute ionization cross section

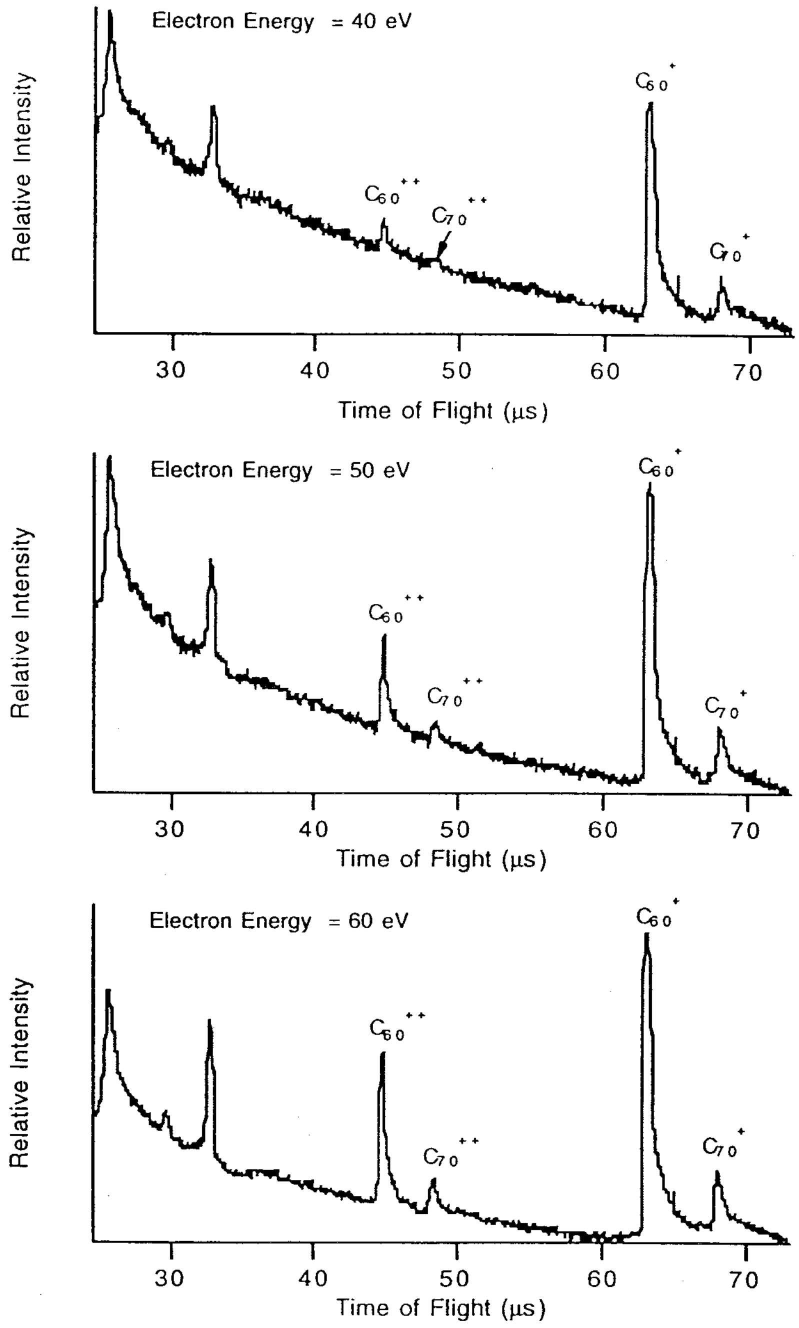

Figure 5.5: Cracking patterns of mixed fullerenes for electron impact energies from 40 to 60 eV.

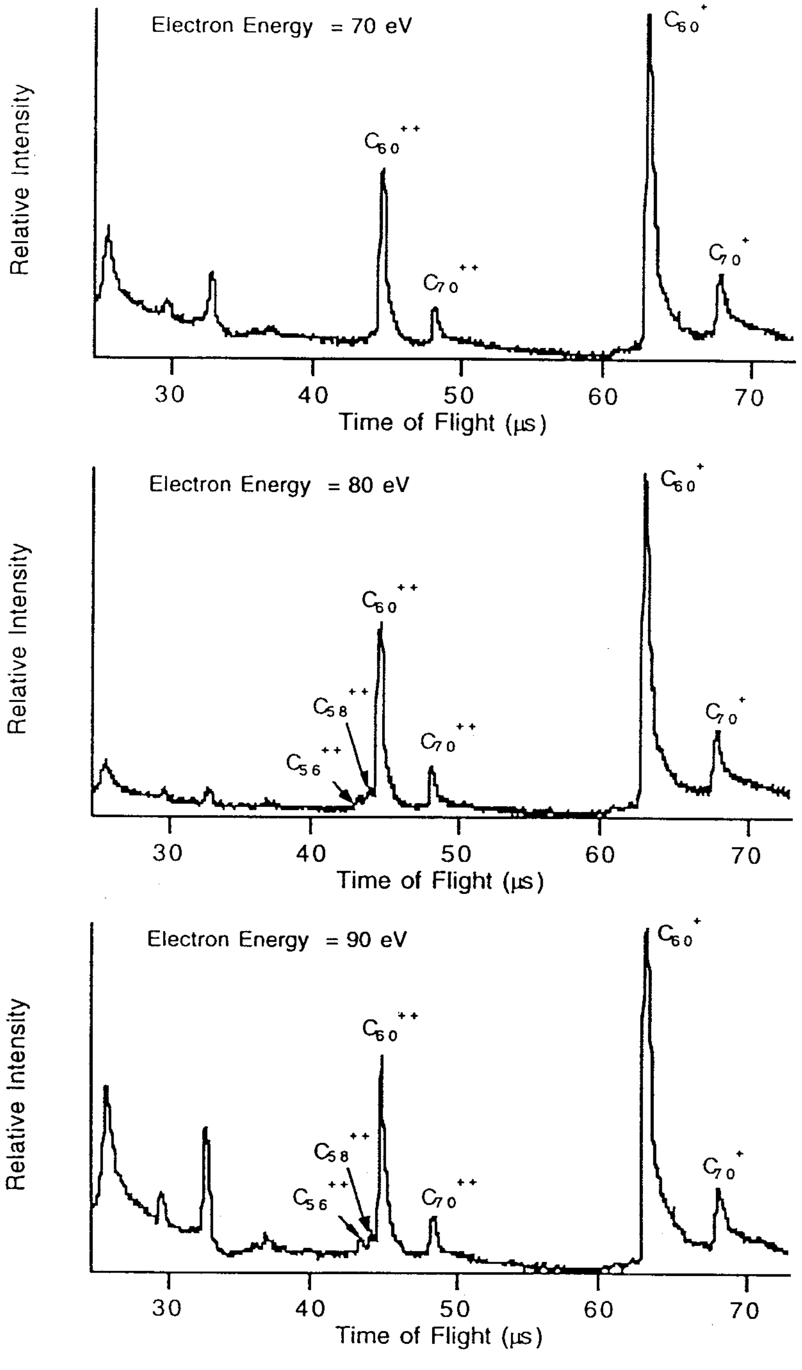

Figure 5.6: Cracking patterns of mixed fullerenes for electron impact energies from 70 to 90 eV.

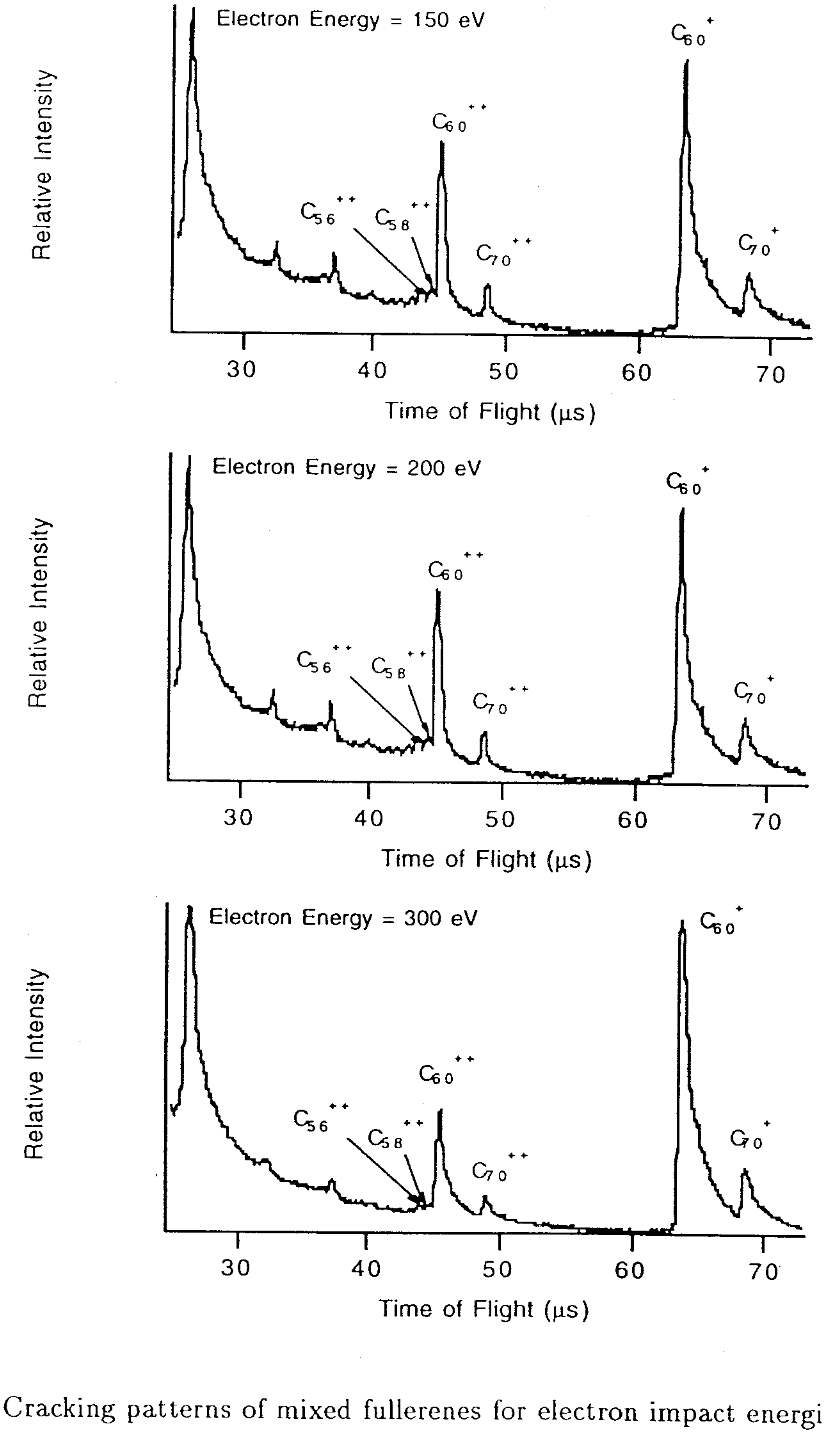

Figure 5.7: Cracking patterns of mixed fullerenes for electron impact energies from 150 to 300 eV.

is related to the ionization function curve by [34]

$$I(E_0) = K(M)\sigma(E_0) \int_v \rho(\mathbf{r}) \cdot f_e(\mathbf{r}, E_0) \cdot \Delta\Omega(\mathbf{r}) d\mathbf{r}, \tag{5.3}$$

where $I(E_0)$ is the number of ions detected per second for incident electron energy E_0, $K(m)$ is an ion-mass-dependent factor which is a function of the transmission of ions through the extraction grids, ion optics, and detection efficiency of the charged particle detector, and $\rho(\mathbf{r})$ and $f_e(\mathbf{r}, E_0)$ are the target density and spatial electron flux distribution, respectively. The solid angle of detection for a collision point located at $\mathbf{r}$ within the collision region of the molecular and electron beams is denoted by $\Delta\Omega(\mathbf{r})$.

It is very difficult to obtain the values needed to solve Equation 5.3. Instead, the standard technique is to calibrate the mass spectrometer with a material of known cross section. The absolute cross section for ionization is then found from [34]

$$\sigma_u(E_0) = \sigma_s(E_0) \frac{I_u(E_0)}{I_s(E_0)} \left(\frac{m_s}{m_u}\right)^{1/2} \frac{F_s}{F_u} \frac{K(m_s)}{K(m_u)}. \tag{5.4}$$

where E_0 is the kinetic energy of the incident electrons, $\sigma_u(E_0)$ and $\sigma_s(E_0)$ are the cross sections for ionization of the species m_u and m_s respectively, $K(m_u)$ and $K(m_s)$ are the mass-dependent transmission and detection efficiencies of the apparatus, and F_u and F_s are the flow rates of the two gas species.

Sai Baba and coworkers [1] were the first to report the absolute ionization cross section of C_{60}^+ by employing the calibration technique described above using silver atoms. They report a C_{60} electron-impact ionization cross section of $(53.5 \pm 5.6) \times 10^{-16}$ cm^2 at 38 eV electron energy. Normalization of their ionization function curve to this point yields a peak cross section at 55 eV of $(60.2 \pm 5.6) \times 10^{-16}$ cm^2. Lezius *et al.* [3] also measured the ionization function curve of C_{60} and normalized their data to the point at 38 eV published by Sai

Baba *et al.*, resulting in a peak cross section at 55 eV electron energy of approximately 65×10^{-16} cm^2.

Scheier *et al.* used a modified additivity rule [35] to normalize the cross section of C_{60}. This latter method yielded a value of 58.8 10^{-20} m^2 [2], in good agreement with the data of Sai Baba *et al.* However, their peak cross section was found to occur at 50 eV electron energy.

Normalization of the data obtained here to Sai Baba's yields a peak cross section of 59.8×10^{-16} cm^2 occurring at 52 eV. The shape of the ionization curve is compared to that of Scheier *et al.* [2] and Sai Baba *et al.* [1] in Figure 5.8. The relative ionization function curve for C_{60}^{++} is shown in Figure 5.9.

These peak ionization cross section values are significantly lower than those estimated by both the additivity rule and the polarizability correlation discussed earlier. Part of this poor correlation may arise from choosing cross section contributions from carbon atoms at 70 eV. It is apparent that the ionization function curve for C_{60} peaks at an electron impact energy of 20 eV lower than this. It is probable that the cross section for single ionization of C_{60} peaks at a lower value because fragmentation processes begin to play a significant role at the higher (greater than 45 eV [8]) electron energies. Harrison et al. [20] noted long ago that in cases where an appreciable number of collisions leads to excitation rather than ionization, the additivity rule breaks down. They also warned that application of either an additivity rule or correlation with polarizability was only valid within a homologous series. The fullerene family cannot easily be placed in one of these series.

It should be cautioned that at present, the work of Sai Baba *et al.* provides the *only* experimentally determined normalization point for the C_{60} ionization function curve. It has not yet been duplicated. In addition, the modified additivity rule [35] employed by Scheier *et al.* significantly underestimates the cross section of many molecules to which it is applied. Therefore, future studies may show the peak cross section for ionization of C_{60} by electron impact to be different than the values discussed here.

Some debate has arisen over the shape of the C_{60} ionization function curve. Sai Baba showed a kink in the curve at approximately 30 eV. Lezius *et al.* [3] and Scheier et al. [2] observed only a smoothly increasing curve, and no resonance structures in the 30 eV region. Gallogly *et al.* [30] also display a kink in their C_{60} ionization function curve aquired in a study of delayed ionization. Only a smoothly increasing function near the 32 eV region of the ionization function curve is observed in the data presented here. Two possible explainations of the structure observed by both Sai Baba *et al.* and Gallogly *et al.* are that either electron gun characteristics resulted in the peak shape, or that excited states of C_{60} participate in the ionization process.

5.3.4 Appearance Potentials

The first ionization potential of C_{60} has been measured by Lichtenberger *et al.* [4] to be 7.6±0.2 eV, and by Zimmerman [5] to be 7.61±0.1 eV. The second ionization potential has been determined by charge transfer bracketing [6] to be 9.7±0.2 eV. More recently, Lifshitz [7] has reported a value for the second ionization potential of C_{60} measured by charge stripping as 12.25±0.5 eV.

To calibrate the electron beam energy for the determination of appearance potentials for fullerene ions, the ionization function curve of H_2O^+ (a contaminant in the vacuum system) was used. The experimentally determined appearance potential was compared to the known

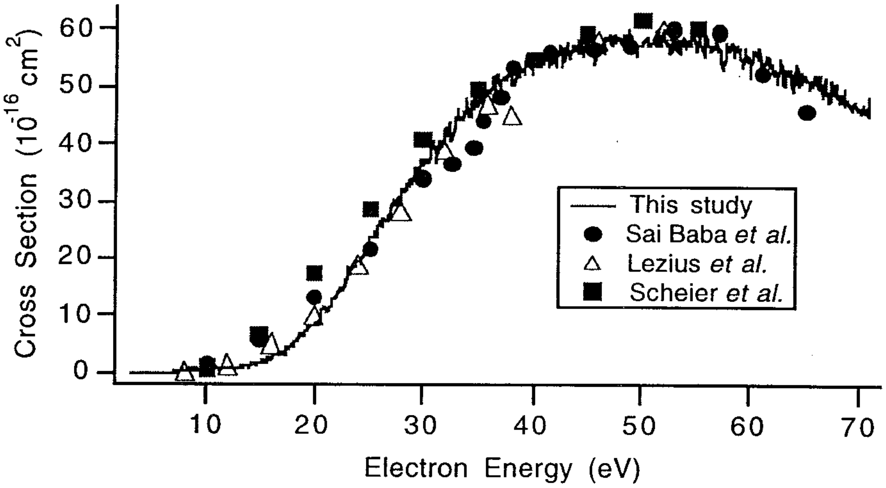

Figure 5.8: Ionization function curve for the formation of C_{60}^+ by electron impact ionization. The curve is normalized to the data of Sai Baba et al. [1], and is shown along with data of References [1,2,3].

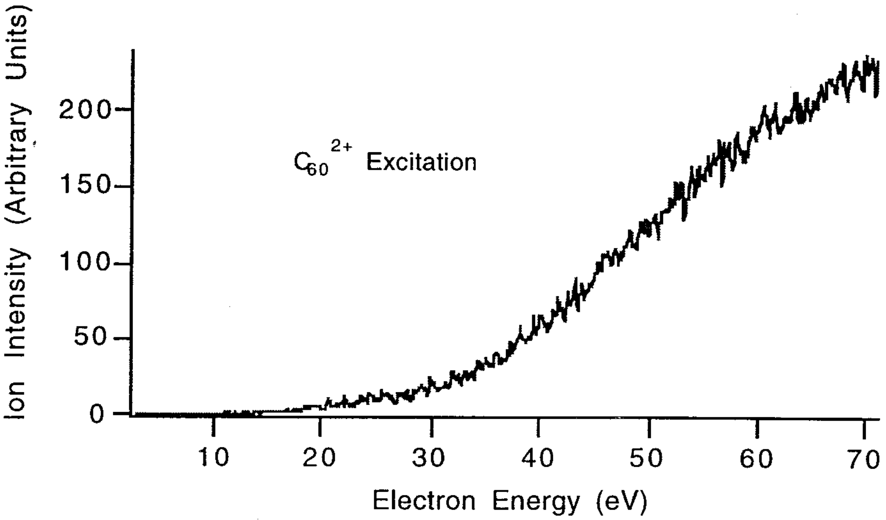

Figure 5.9: Ionization function curve for the formation of C_{60}^{++} by electron impact ionization.

value of 12.612±0.01 [36] for H_2O^+, and a correction factor was obtained. This correction factor was then applied to the appearance potentials found for C_{60}^+ and C_{60}^{2+}, yielding values of 7.8±0.5 and 16.4±0.5 eV, respectively. Though the value for singly ionized C_{60} agrees well with others reported in the literature [5,4,9], it is evident that the double ionization potential via electron impact is significantly lower than the value of 19.0 ± 0.03 eV [11] reported for the species by photoionization.

Table 5.1 shows appearance potentials reported for the ionization processes

$$C_{60} + e^- \rightarrow C_{60}^+ + 2e^-, \tag{5.5}$$

$$C_{60} + e^- \rightarrow C_{60}^{2+} + 3e^-, \tag{5.6}$$

and

$$C_{60}^+ + e^- \rightarrow C_{60}^{2+} + 2e^-. \tag{5.7}$$

5.4 Conclusions

Cracking patterns, appearance potentials, and ionization function curves for C_{60}^+ and C_{60}^{2+} were measured. The findings of this research attest to the high stability of C_{60} and resistance to fragmentation by electron impact, especially at electron energies below 70 eV. The results are similar to those reported elsewhere in the literature. Interesting results for the determination of the appearance potential for C_{60}^{2+} were obtained, while the appearance potential found for C_{60}^+ is well accepted. Comparison of the ionization function curve found for C_{60}^+ does not show a kink in the 32 eV region like that reported by Sai Baba *et al.* [1], but rather a smoothly increasing function.

Ref	C_{60}^{+}/C_{60}	C_{60}^{2+}/C_{60}	C_{60}^{2+}/C_{60}^{+}	Method
[5]	7.61±0.11	—	—	Charge-transfer bracketing
[4]	7.61±0.02	—	—	Photo-electron, gas phase target
[6]	—	—	9.7±0.2	Charge-transfer bracketing
[7]	—	—	12.25	Deduced from charge-stripping reaction
[9]	7.54±0.04	—	—	Photoionization
[1]	8.5±0.5	—	—	Electron impact
[12]	7.57±0.01	—	—	Photoionization
[14]	—	—	11.9	Charge stripping
[15]	—	—	8.5±0.5	Charge stripping
[11]	—	19.0±0.03	—	Photoionization
Present	7.8±0.5	16.4±0.5	—	Electron impact

Table 5.1: Experimentally determined appearance energies of C_{60}^{+} and C_{60}^{2+} in eV.

The results of these experiments show that the peak ionization cross section of C_{60} is an order of magnitude larger than that of xenon, implying that the ion production cost for C_{60} ions in a plasma thruster may be lower than that of xenon. In addition, the resilience against fragmentation demonstrated by C_{60} in the electron energy range of interest for electric thrusters (20 to 30 eV) is encouraging.

References

[1] M. Sai Baba, T. Narasimhan, R. Balasubramanian, and C. Mathews, a) "Appearance Potential and Electron Impact Ionisation Cross-Section of C_{60}," *International Journal of Mass Spectrometry and Ion Processes* **114**, R1 (1992), b) "Shape of the Ionisation Cross Section Function for $C_{60} + e \rightarrow C_{60}^{+} + 2e$ from Threshold to Maximum: Reply to Comment by Scheier et al.," *International Journal of Mass Spectrometry and Ion Processes* **130**, L5 (1994).

[2] P. Scheier, M. Lezius, B. Dünser, R. Robl, B. Schiestl, and T. Märk, "Comment on the Shape of the Ionization Cross Section Function for $C_{60} + e \rightarrow C_{60}^{+} + 2e$ from Threshold to Maximum," *International Journal of Mass Spectrometry and Ion Processes* **125**, R17 (1993).

[3] M. Lezius, P. Scheier, M. Foltin, B. Dünser, T. Rauth, V. Akimov, W. Krätschmer, and T. Märk, "Interaction of Free Electrons with C_{60}: Ionization and Attachment Reactions," *International Journal of Mass Spectroscopy and Ion Processes* **129**, 49 (1993).

[4] D. Lichtenberger, K. Nebesny, C. Ray, D. Huffman, and L. Lamb, "Valence and Core Photoelectron Spectroscopy of C_{60}, Buckminsterfullerene," *Chemical Physics Letters*

176(2), 203 (1991).

[5] J. Zimmerman, J. Eyler, S. Bach, and S. McElvany, "Magic Number Carbon Clusters: Ionization Potentials and Selective Reactivity," *Journal of Chemical Physics* **94(5)**, 3556 (1991).

[6] S. McElvany, M. Ross, and J. Callahan, "First and Second Ionization Potentials, Reactions, and Surface Collisions of C_{60} and Related Clusters," *Materials Research Society Symposium Proceedings* **206**, 697 (1991).

[7] C. Lifshitz, M. Iraqi, T. Peres, and J. Fischer, "Charge Stripping C_{60}^{+}," *Rapid Communications in Mass Spectrometry* **5**, 238 (1991).

[8] M. Foltin, M. Lezius, P. Scheier, and T. Märk, "On the Unimolecular Fragmentation of C_{60}^{+} Fullerene Ions — the Comparison of Measured and Calculated Breakdown Patterns," *Journal of Chemical Physics* **98(12)**, 9624 (1993).

[9] I. Hertel, H. Steger, J. deVries, B. Weissner, C. Menzel, B. Kamke, and W. Kamke, "Giant Plasmon Excitation in Free C_{60} and C_{70} Molecules Studied by Photoionization," *Physical Review Letters* **68(6)**, 784 (1992).

[10] R. Völpel, G. Hofmann, M. Steidl, M. Stenke, M. Schlapp, R. Trassl, and E. Salzborn, "Ionization and Fragmentation of Fullerene Ions by Electron Impact," *Physical Review Letters* **71(21)**, 3439 (1993).

[11] H. Steger, J. de Vries, B. Kamke, W. Kamke, and T. Drewello, "Direct Double Ionization of C_{60} and C_{70} Fullerenes Using Synchrotron Radiation," *Chemical Physics Letters* **194(4-6)**, 452 (1992).

[12] R. Yoo, B. Ruscic, and J. Berkowitz, "Vacuum Ultraviolet Photoionization Mass-Spectrometric Study of C_{60}," *Journal of Chemical Physics* **96(2)**, 911 (1992).

[13] S. Srivastava, G. Jong, S.D. Leifer, and W.A. Saunders, "Ionization of C_{60} (Buckminsterfullerene) by Electron Impact," *Rapid Communications in Mass Spectrometry* **7**, 610 (1993).

[14] K. Caldwell, D. Giblin, and M. Gross, "High Energy Collisions of Fullerene Radical Cations with Target Gases — Capture of the Target Gas and Charge Stripping of C_{60}^{+}, C_{70}^{+}, and C_{84}^{+}," *Journal of the American Chemical Society* **114(10)**, 3743 (1992).

[15] D. Mathur, P. Grino, and A. Brenton, "Charge Stripping of C_{60}^{+} - A New Value for the Double Ionization-Energy of Buckminsterfullerene," *Rapid Communications in Mass Spectrometry* **6**, 484 (1992).

[16] B. Walsch, C. Cocke, R. Völpel, and E. Salzborn, "Electron-Capture from C_{60} by Slow Multiply-Charged Ions," *Physical Review Letters* **72(10)**, 1439 (1994).

[17] D. Rapp and S. Leifer, "Effect of the Use of C_{60} as a Propellant in Ion Thrusters," *JPL Report* **D-10169**, Pasadena, CA, (1992).

[18] J. Otvos and D. Stevenson, "Cross Sections of Molecules for Ionization by Electrons," *Journal of the American Chemical Society* **78**, 546 (1956).

[19] F. Lampe, J. Franklin, and F. Field, "Cross Sections for Ionization by Electrons," *Journal of the American Chemical Society* **79**, 6129 (1957).

[20] A. Harrison, E. Jones, S. Gupta, and G. Nagy, "Total Cross Sections for Ionization by Electron Impact," *Canadian Journal of Chemistry* **44**, 1967 (1966).

[21] J. Mann, "Ionization Cross Sections of the Elements Calculated from Mean-Square Radii of Atomic Orbital," *Journal of Chemical Physics* **46**, 1646 (1967).

[22] L. Beran and L. Kevan, "Molecular Ionization Cross Sections at 70 eV," *Journal of Physical Chemistry* **75**, 3866 (1969).

[23] D. Rapp and P. Englander-Golden, "Total Cross Sections for Ionization and Attachment in Gases by Electron Impact," *Journal of Chemical Physics* **43(5)**, 1464 (1965).

[24] P. Fowler, P. Lazzeretti, and R. Zanasi, "Electric and Magnetic Properties of the Aromatic Sixty-Carbon Cage," *Chemical Physics Letters* **165**, 79 (1990).

[25] S.L. Ren, Y. Wang, A.M. Rao, E. McRae, J.M. Holden, T. Hager, K. Wang, W. Lee, H.F. Ni, J. Selegue, and P.C. Eklund, "Ellipsometric Determination of the Optical Constants of C_{60} (Buckminsterfullerene) Films," *Applied Physics Letters* **59(21)**, 2678 (1991).

[26] G. Guizzetti, F. Marabelli, M. Patrini, V. Capozzi, G.F. Lorusso, A. Minafra, M. Manfredini, and P. Milani, "Optical Properties of Fullerite Thin Films in the 0.4 to 32 eV Energy Range," *Physica Status Solidi (b)* **183**, 267 (1994).

[27] A. Hebard, R. Haddon, R. Fleming, and A. Korton, "Deposition and Characterization of Fullerene Films," *Applied Physics Letters* **59(17)**, 2109 (1991).

[28] S. Srivastava, "Ion Formation by Electron Impact," Course notes, University of Southern California, (1991).

[29] R. Opsal, K. Owens, and J. Reilly, "Resolution in the Linear Time-of-Flight Mass Spectrometer," *Analytical Chemistry* **57**, 1884 (1985).

[30] E. Gallogly, Y. Bao, K. Han, H. Lin, and W. Jackson, "Electron Impact Excitation of Delayed Ionization of C_{60} — Evidence for Rybderg States," *Journal of Physical Chemistry* **98**, 3121 (1994).

[31] C. Yeretzian and R. Whetten, "Delayed Emission of Electrons from C_{60} Following Energetic Impact Against Graphite," *Zeitschrift fur Physik D* **24(2)**, 199 (1992).

[32] E. Campbell, G. Ulmer, and I. Hertel, "Delayed Ionization of C_{60} and C_{70}," *Physical Review Letters* **67(15)**, 1986 (1991).

[33] P. Wurz and K. Lykke, "Delayed Electron Emission from Photoexcited C_{60}," *Journal of Chemical Physics* **95(9)**, 7008 (1991).

[34] E. Krishnakumar, and S. Srivastava, "Ionisation Cross Sections of Rare-Gas Atoms by Electron Impact," *Journal of Physics B* **21**, 1055 (1988).

[35] D. Margreiter, H. Deutsch, M. Schmidt, and T. Märk, "Electron Impact Ionization Cross Sections of Molecules," *International Journal of Mass Spectroscopy and Ion Processes* **100**, 157 (1990).

[36] S. Lias, J. Bartmess, J. Liebman, J. Holmes, R. Levin, and W. Mallard, "Gas Phase Ion and Neutral Chemistry," *Journal of Physical Chemistry Reference Data* **17(S1)**, 621 (1988).

Chapter 6

Ion Thruster Experiments

6.1 Introduction

Since 1991, three groups [1]-[3] have reported on the development of ion thrusters which utilize fullerenes as a propellant. Anderson and Fitzgerald [1], and Hruby *et al.* [2] both successfully sustained DC fullerene plasma discharges using thoriated tungsten filament cathode ion sources. Anderson and Fitzgerald were able to extract beam currents between 2 and 3 mA from their device with a net accelerating voltage of 1.9 kV and a minimum discharge voltage of 22 VDC. They confirmed the presence of fullerene ions by mass spectral analysis of the extracted ion beam. Hruby *et al.* [2] detected fullerene material deposited on optical surfaces using Fourier transform infrared (FTIR) spectroscopy. Both of these groups reported substantial erosion of the filament cathodes used in their devices that ultimately resulted in cathode failure. The presence of a significant quantity of toluene-insoluble carbonaceous material was observed in the effusion cell by both groups after heating.

Hruby *et al.* [2] carried out tests of fullerene material compatibility with stainless steel, molybdenum, alumina, boron nitride, aluminum nitride, and quartz. They reported that no reaction of the fullerenes occurred with any of these materials, but chose quartz for their discharge chamber with molybdenum and stainless steels grids. Anderson and Fitzgerald [1] used both graphite and stainless steel sources and stainless steel grids. In both sources, notable degradation of the propellant molecules at high temperature was confirmed by FTIR spectroscopic analysis of the powder remaining in the effusive cell and on the walls of the discharge chamber. However, mass spectral analysis of the ion beam did not indicate the presence of C_2 fragments which would be expected from collisionally dissociated fullerenes [4].

Horak and Gibson [5] operated a commercially available Kaufman ion source with fullerenes for ion assisted deposition applications. They were able to sustain a discharge for 30 minutes while extracting a 50-100 $\mu A/cm^2$ beam of fullerene ions. They reported that approximately 10% of the initial mass of C_{60} was recovered from the discharge chamber as a mixture of graphitic carbon and fullerene.

Takegahara and Nakayama [3] have reported an unsuccessful attempt to establish an RF-generated plasma using fullerenes. They found that their quartz discharge chamber wall temperature was too low, resulting in condensation of the fullerene propellant. Takegahara and Nakayama obtained FTIR absorption spectra of their C_{60} powder both before evaporation and after condensation. If normalized, their spectra indicate a loss of material similar to that observed by Hruby *et al.* and Anderson and Fitzgerald.

D.H. Yu *et al.* [6] investigated the formation and fragmentation of positive fullerene ions created in an electron-impact ion source. The electron energy in the ion source was 50 eV. Fullerene ions were then accelerated to 30 keV and introduced to a hydrogen or argon gas collision chamber where they underwent collisionally-induced dissociation. Unimolecular dissociation rate constants for the process of fragmentation via removal of even-numbered carbon fragments were obtained.

Gruen *et al.* [7] created fullerene plasmas for materials applications. They used a fullerene/argon/hydrogen mixture in a 500 W microwave plasma discharge to collisonally induce dissociation of the carbon molecules for use as diamond film precursors. Optical spectroscopy of their plasma showed strong C_2 emission.

A negative C_{60} plasma source was developed by Sato and coworkers [8] for materials processing applications. Fullerene molecules were introduced into a low-temperature potassium plasma produced by contact ionization and confined by a strong, axial magnetic field. Singly-charged negative C_{60} ions were observed.

For materials processing applications where a negative ion source could be used, C_{60}^- plasmas could provide a viable source of gas-phase carbon without the presence of hydrogen. C_{60} vapor has been shown to be a useful precursor for the formation of silicon carbide nanostructructures which had been difficult to produce by etching techniques [9]. At the temperatures used for the silicon carbide film growth, the fullerenes did not react with a silicon dioxide layer used to provide a mask.

Although there have now been many reports of fullerene ion sources used for either the study of fullerene physical properties or materials processing applications, none of these sources have been designed to minimize fullerene fragmentation or maximize efficiency of ion production. These design requirements are important for C_{60} thruster applications were the utilized fraction of fullerene molecules must be maximized. Because of the thermal problems encountered in DC fullerene thruster operation and discussed in Chapter 3, another method of fullerene ionization was pursued for this study.

6.2 RF Discharge Chamber Experiments

6.2.1 Apparatus

To avoid the presence of high temperature surfaces other than the extraction grids, an RF discharge chamber similar to that of Takegahara and Nakayama [3] was constructed. An Eni Power Systems 13.56 MHz RF power generator (model 600A) and impedance matching circuit to reduce reflective RF losses from the engine were used. A schematic diagram and a photograph of the RF thruster assembly are shown in Figures 6.1 and 6.2, respectively. The discharge chamber consists of a 7.0 cm high, 7.0 cm diameter cylindrical quartz vessel with an extraction grid system and a quartz crucible containing fullerene propellant flanged to opposite ends. An RF coil wrapped around the outside of the quartz vessel induces an azimuthal electric AC field inside the chamber. The fullerene plasma is maintained inductively, eliminating the need for hot electrode surfaces inside the discharge chamber. Ignition of the discharge can be obtained with the aid of electrons attracted from the neutralizer filament into the discharge chamber by temporarily applying a positive voltage to the accelerator grid. The RF field further accelerates the electrons inside the discharge chamber, leading to breakdown. Because of the difficulties encountered by Takegahara and Nakayama [3] in obtaining high wall temperatures to prevent condensation of fullerene vapor, a resistively heated coil was used to maintain discharge wall temperatures above 723 K. Vacuum system pressure was in the 10^{-6} Torr range during these experiments.

The thruster was equipped with an optics system consisting of stainless steel screen and accelerator grids. The grids were spaced 1.27 mm apart and had 331 matching 2.4

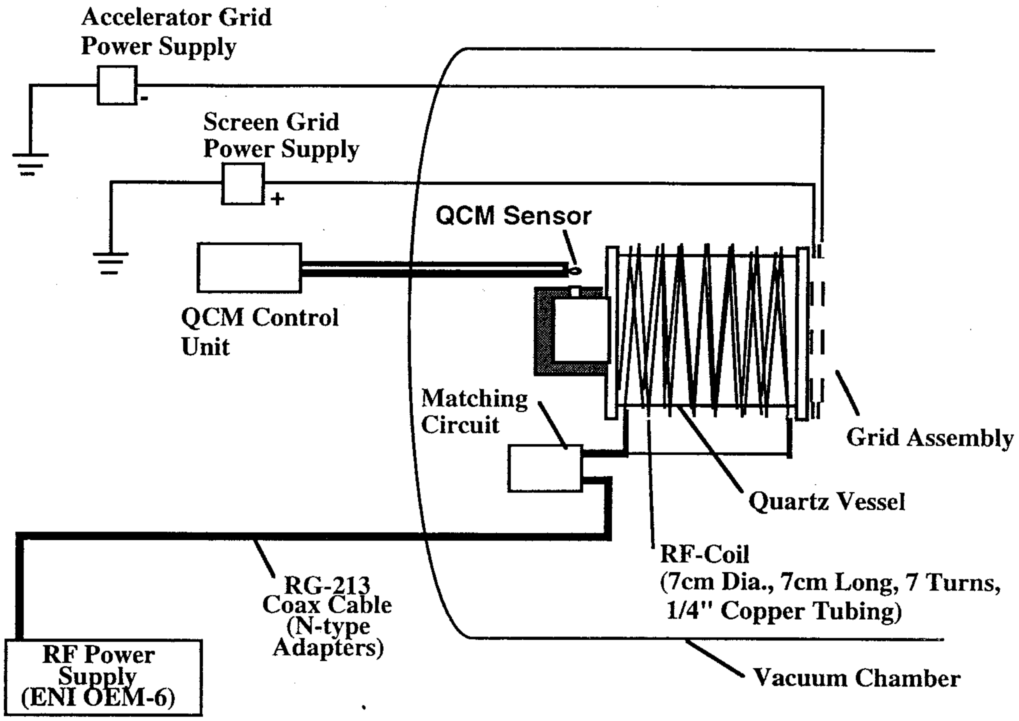

Figure 6.1: Schematic diagram of fullerene RF thruster apparatus. Pictured is the quartz discharge chamber inside an RF coil. A crucible for fullerene vaporization is attached to the upstream side of the disharge chamber. A quartz-crystal-microbalance is used to determine fullerene flow rates. The assembly is housed inside a 90 cm by 150 cm vacuum chamber evacuated to the 10^{-6} Torr range.

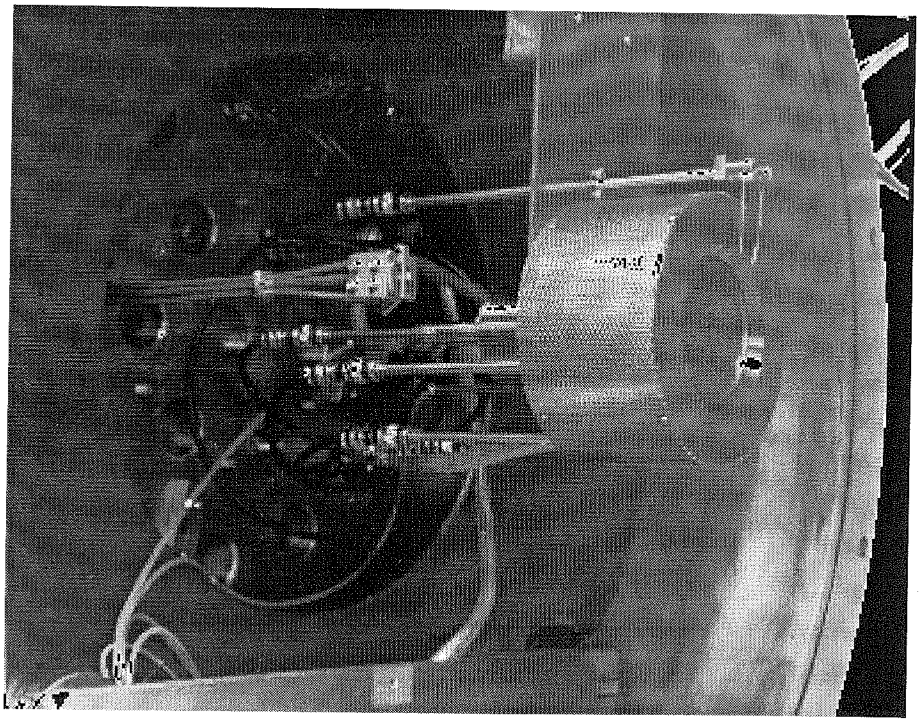

Figure 6.2: Picture of the RF fullerene ion thruster mounted in the vacuum facility. A tungsten filament neutralizer can be seen in front of the accelerator grid. A view of the thruster coil is obscured by the presence of a stainless steel ground screen.

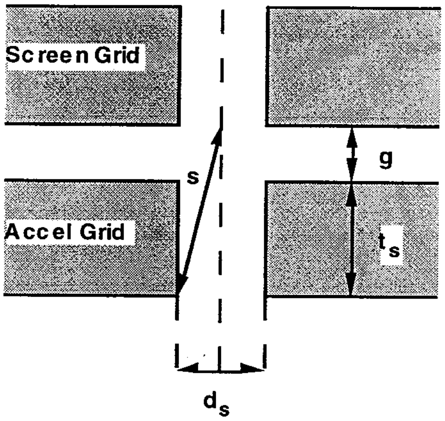

Figure 6.3: Diagram showing the effective grid spacing resulting from finite grid thickness.

mm diameter holes. Both grids were approximately 2 mm thick. Thus, the open-area-fraction of the grids was 0.385. The space-charge-limited current density for these grids was calculated to be 31 mA for C_{60} and 73 mA for xenon. This calculation used an effective grid spacing $s = \sqrt{(d_s/2)^2 + (t_s + g)^2}$ (see Figure 6.3) to provide a more accurate determination of space-charge-limited current density than would be obtained by using only the grid-gap. In the figure, d_s is the grid hole diameter, t_s is the grid thickness, and g is the grid gap.

Flow Measurements

An Inficon model XTM/2 quartz crystal micro-balance (QCM) was used to measure real-time fullerene mass flow rates supplied by a quartz crucible to the RF ion engine. The crucible consists of a 6 mm diameter tube fused to a coaxial 25 mm diameter tube in which fullerene powder is placed. The center tube is used to introduce other test gases such as xenon and argon into the discharge chamber. The flanged end of the crucible attaches to the upstream end of the discharge chamber. A dam blocks the bottom half of the crucible to prevent fullerene spillage. The mass flow rate was estimated by siphoning a fraction of

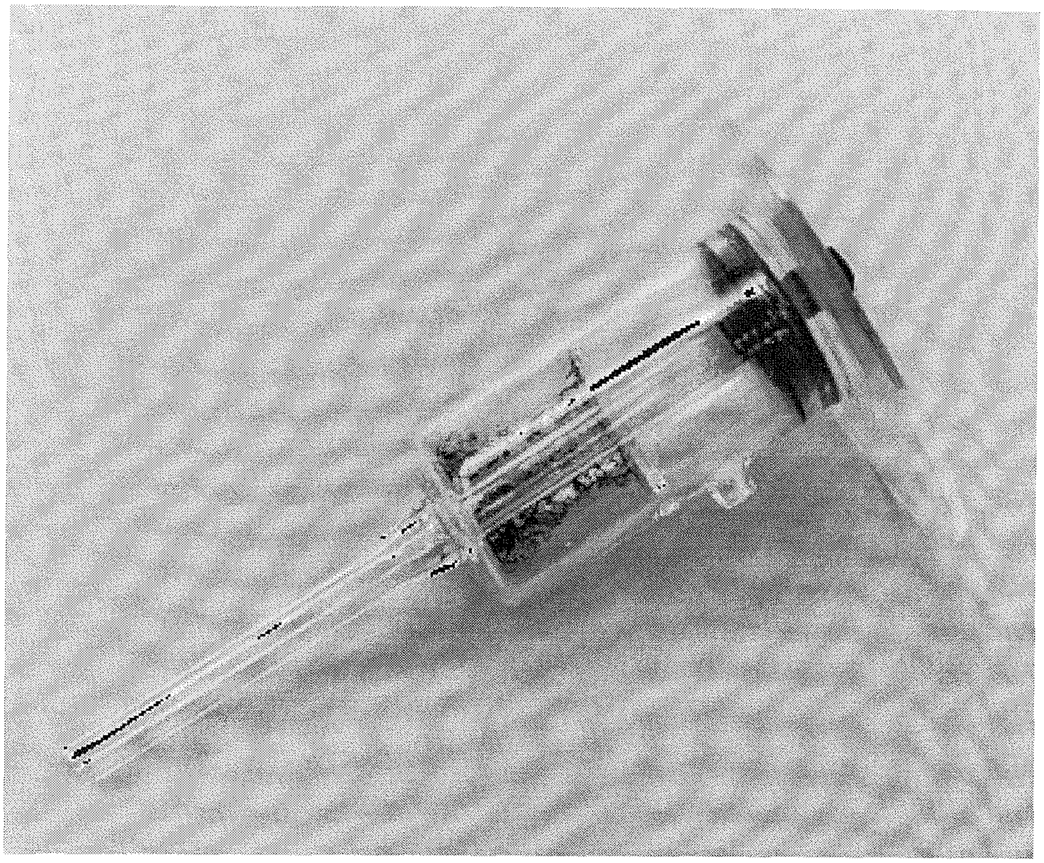

Figure 6.4: Quartz crucible used for sublimation of fullerenes into the plasma discharge chamber. The tube along the crucible axis allowed other test gases such as xenon and argon to be introduced into the thruster as well. The crucible attaches to the upstream end of the discharge chamber. The material at the flanged-end of the crucible is condensed fullerene. The material behind the quartz dam is amorphous and graphitic carbon residue.

the flow from a small hole in the crucible. This flow was directed toward the QCM sensor which was located approximately 70 mm away from the crucible. Figure 6.4 shows the quartz crucible used in these experiments. The material at the flanged-end of the crucible is condensed fullerene. The material behind the quartz dam is amorphous and graphitic carbon residue.

Temperatures were calibrated using thermocouples mounted inside the crucible and between the heater wire and crucible wall. The temperature on the inside of the crucible was approximately 40 to 50 K lower than the temperature measured between the outside of the crucible and the heating coil.

Because the geometry of the experimental apparatus does not change during the experiment, it is assumed that the fraction of the flow impinging on the QCM remains constant as the flow rate and temperature vary. The QCM is water cooled and the temperature of the QCM holder was found to be below 298 K during all experiments.

The calibration constant for total flow rate was determined by weighing the fullerene-filled crucible before and after heating to find the total mass of evaporated material. This quantity was then divided by the total accumulated mass on the qcm crystal to obtain the calibration constant C where

$$C = \frac{\Delta M}{f \int_t \dot{m}_{qcm} dt} \tag{6.1}$$

where ΔM is the total mass sublimated from the crucible, and f is the fraction of flow $\dot{m}_{qcm}$ striking the qcm. Note that this calibration technique assumes that the fraction of fullerene flow from the hole facing the qcm is small compared to the total flow into the discharge chamber, as the actual mass flow rate to the discharge chamber is

$$\dot{m}_{RF} = \dot{m}_{qcm}(Cf - 1). \tag{6.2}$$

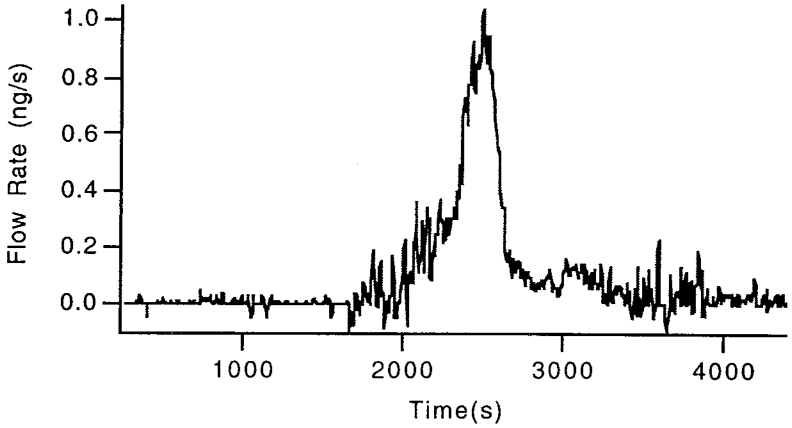

Figure 6.5: Fullerene flow rate recorded by the quartz crystal microbalance.

Instead, a flow rate of $\dot{m}_{RF} = Cf\dot{m}_{qcm}$ was assumed. The flow rate and total deposited fullerene mass for this calibration is shown in Figures 6.5 and 6.6, respectively.

Beam Diagnostics

An E×B mass spectrometer, also known as a Wien filter [10], was used to display peaks of all of the species present in the ion beam. E×B probes are useful for discriminating ions which have the same kinetic energy but different charge-to-mass ratios.

In an E×B probe, a region with orthogonal electric and magnetic fields constrains charged particles of a particular velocity to experience equal and opposite forces through interaction with the two fields; these particles travel in a straight line. The mass spectrum may be scanned by varying the electric field in the probe. Probe mass resolution is given by [11]

$$M/\Delta M = \sqrt{\frac{2q}{M\Delta V}}\frac{BZ_f^2L}{16s(Z_f + L)}, \tag{6.3}$$

where M is the mass of the particle, q is the charge, Z_f is the length of the E×B region, L is

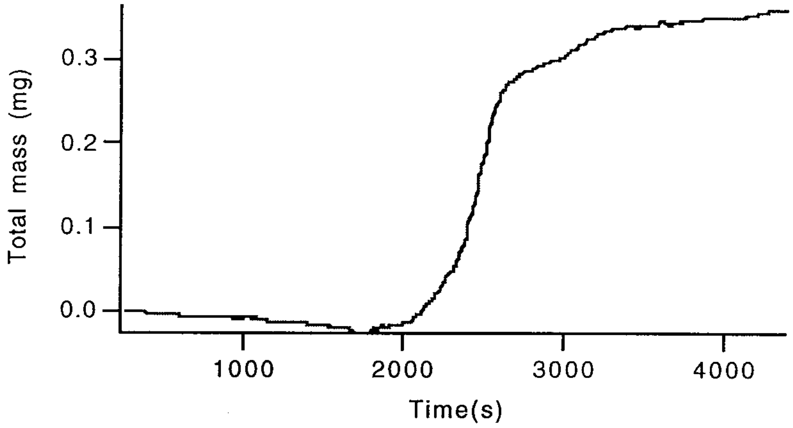

Figure 6.6: Total accumulated fullerene mass on the quartz crystal microbalance as a function of time.

the length of the collimator, ΔV is the potential through which the particles are accelerated prior to entering the probe, B is the magnetic field strength, and s is the slit width. The resolution was 5.1 for C_{60}. Figure 6.7 shows an E×B probe trace of the mass spectrum of ions extracted from the DC fullerene discharge of Anderson and Fitzgerald [1]. The magnetic field strength at the probe centerline was approximately 1100 Gauss. The gap between the two parallel plates used to establish the electric field was 3.25 cm wide. The E×B region was 11.8 cm long and the entrance slit to the device was 1 mm wide by 1.7 cm long.

6.2.2 Results and Discussion

The RF ion engine was first operated using xenon as the source gas. Figure 6.8 shows the extracted beam current as a function of RF power for total and net accelerating voltages of 2.5 and 1.5 kV, respectively. The two curves shown correspond to flow rates of 12.6 and 8.6

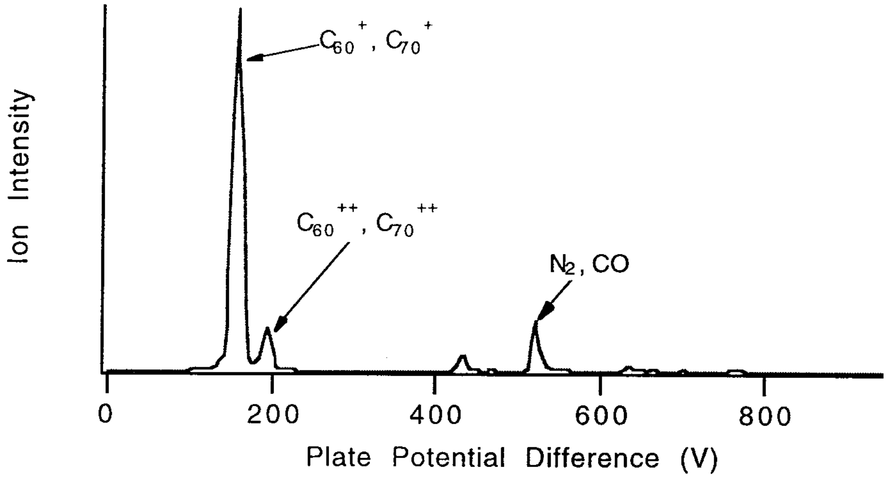

Figure 6.7: Mass spectrum of beam ions extracted from a DC fullerene discharge chamber taken with an E×B probe.

mg/min. The maximum extracted ion current was approximately 40 mA. The beam-ion energy cost was found to be approximately 1400 eV/ion. Higher efficiency could be achieved for a smaller surface-to-volume ratio discharge chamber. However, the high ion production cost found here results from poor grid design and large ($\tilde{3}0\%$) RF power losses in the structure. When C_{60} was added to the xenon flow, fullerene ions were extracted. However, when the ratio of fullerene to xenon neutrals exceeded 1:16, the plasma extinguished. This result led to suspicion that C_{60} anion formation was responsible for quenching the plasma.

One difference between C_{60} and noble gas propellants is that C_{60} has a large cross-section for negative ion formation, even at electron energies as high as 14 eV [12]-[14]. Due to the large cross-section for anion formation, electron attachment can dominate over positive ion formation for a low energy electron group. If this occurs, the C_{60} behaves as an electron scavenger and the discharge can be quenched. The electron energy distribution in a typical

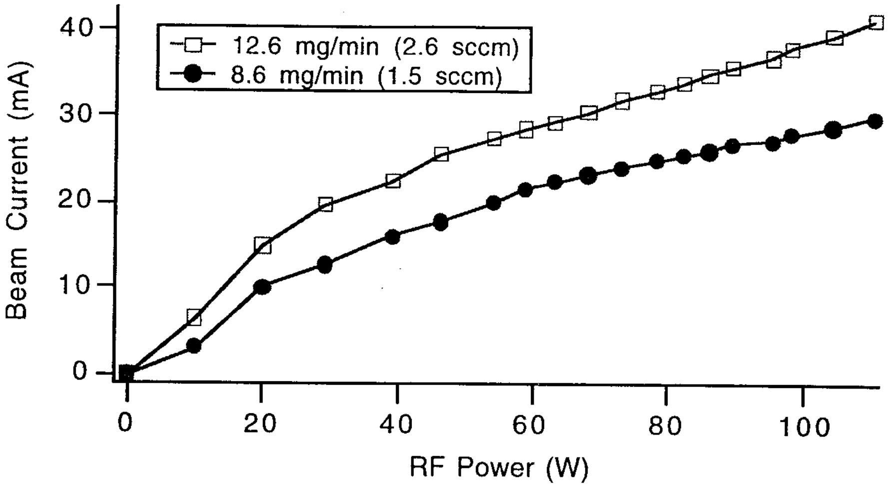

Figure 6.8: Beam current as a function of RF power for xenon plasma discharge. The two curves correspond to different xenon flow rates into the discharge chamber.

electron bombardment discharge has a Maxwellian group and a primary electron group with energies corresponding to the discharge voltage. Therefore, it is of interest to estimate both the C_{60} anion and cation formation rates at various electron temperatures.

To estimate the ion production rates in a plasma, peak intensities for positive and negative ion production shown in the literature [15,14] were used to obtain rate factors for ion production $< \sigma v >$. It was assumed that the electrons used to aquire these data have a monoenergetic distribution. The rate factor for ion production resulting from collisions with the Maxwellian electron group in the plasma is

$$< \sigma v >= \frac{\int_0^\infty \sigma v dn}{\int_0^\infty dn}. \tag{6.4}$$

The differential form of Maxwell's law of the distribution of velocities is given by

$$dn = \frac{2\pi n\sqrt{E}}{(\pi k_B T)^{3/2}} \exp(-E/k_B T) dE, \tag{6.5}$$

so that the denominator of Equation 6.4 is just a constant:

$$\int_0^\infty \frac{2\pi n\sqrt{E}}{(\pi k_B T)^{3/2}} \exp(-E/k_B T)dE = \int_0^\infty dn = constant. \tag{6.6}$$

Simplifying Equation 6.4 yields

$$< \sigma v >= A \int_0^\infty \sigma E \exp(-E/k_B T)dE \tag{6.7}$$

where $(2\pi n\sqrt{2/m})/([\pi k_B T]^{3/2} \int_0^\infty dn) = A$.

By substituting $\sqrt{E} < \sigma\sqrt{E} >$ for σE in Equation 6.7, ratefactors were determined using cross section data for negative fullerene ion formation from Reference [14] and the cross section for C_{60}^+ formation shown in Chapter 5 normalized to the data of Sai Baba *et al.*. The curves are shown in Figure 6.9. Ionization curves for xenon were obtained from Reference [16]. It is evident that negative fullerene ion production rates exceed those of positive ion production at electron energies below approximately 10 eV. By placing a filament cathode in the discharge chamber via the quartz tube normally used for gas flow, it was possible to operate the device as a DC discharge chamber. A rhenium filament was used for this purpose. To see whether negative ions were being produced, the filament was biased below screen grid potential to provide electrons of 5-10 eV energy and fullerene vapor was introduced into the discharge chamber. The accelerating grids were biased to extract negatively charged particles, and directed the beam to the entrance of the E×B probe. A current of approximately 20 pA was detected when the probe was set to detect 720 amu particles, confirming the presence of C_{60}^-.

In an effort to increase the average electron energy in the plasma, a DC axial magnetic field was applied along the thruster axis to achieve an electron-cyclotron resonance condition with the RF field. To achieve the cyclotron frequency $(qB/2\pi m)$ of 13.56 MHz, an axial

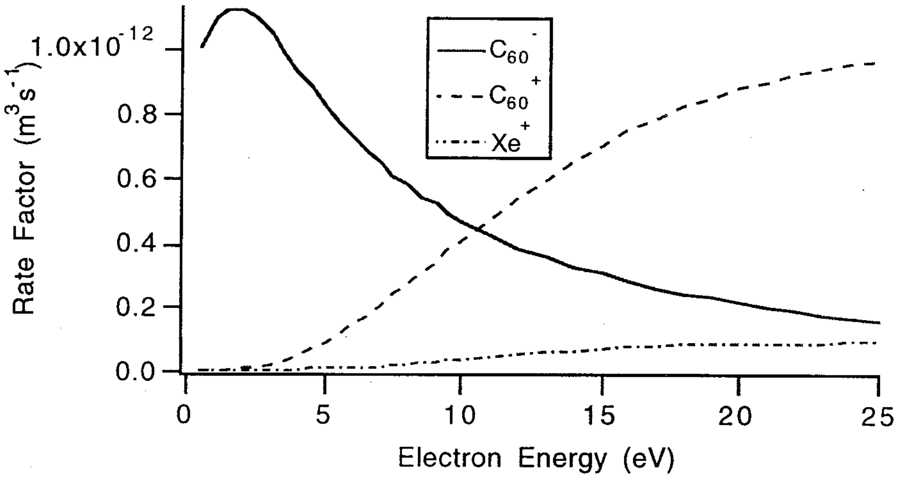

Figure 6.9: Rate factors for the production of xenon ions, and C_{60} anions and cations. It is apparent that the negative ion production rate exceeds that of positive ions at electron temperatures below 10 eV.

magnetic field strength of approximately 5 Gauss was applied. Figure 6.10 shows plots of xenon current extracted from the discharge as a function of magnetic field intensity. The curves clearly show maxima corresponding to the resonance condition. However, it has still not been possible to initiate or sustain a predominantly fullerene plasma using the RF discharge chamber.

6.3 Conclusions

Though the pursuit of a DC fullerene ion thruster was originally abandoned to avoid the presence of high temperature electrode surfaces, an RF fullerene ion thruster has been difficult to operate. This difficulty results from the tendency of C_{60} to form negative ions at low electron energy. High energy electrons must be produced by exciting electrons from the

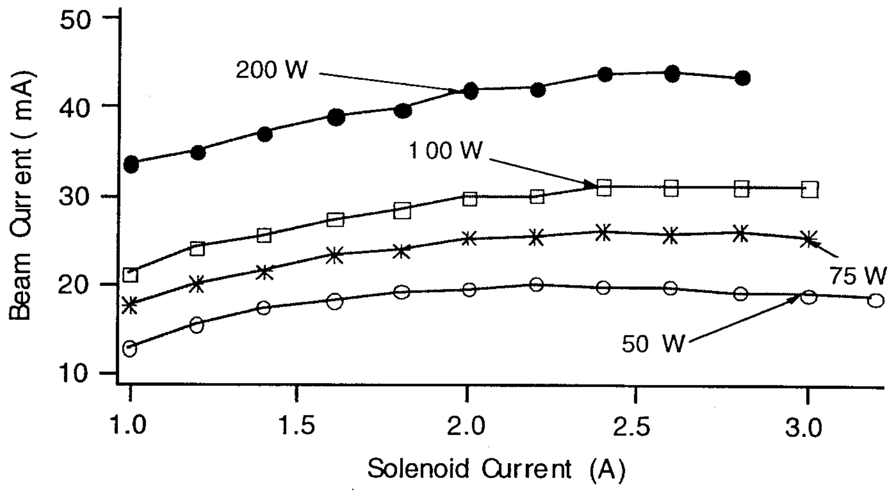

Figure 6.10: Beam current as a function of solenoid magnet current in a xenon RF discharge.

thermalized population in an RF source. However, there is no steady supply of high energy electrons when the Maxwellian electron population is depleted by fullerene anion formation. As a result, RF fullerene plasma discharges quench. Though it is probable that there is a regime of operation where positive ion production may dominate in an fullerene RF ion engine, the average electron energy required for this regime is rather high and may result in higher unrecoverable losses due to excitation and fragmentation of the C_{60} molecules than would occur at lower electron temperatures. It appears to be more favorable to form a fullerene plasma with a steady source of high energy electrons. This may be accomplished by a variety of methods, including photoionization, the use of a cold cathode source, or an electron gun configuration where electron are injected into the discharge without propellant flow around the cathode. Field ionization may also be plausible if fullerene molecules can be sufficiently excited prior to ionization.

The initial tests conducted with filament cathode fullerene ion thrusters demonstrated the successful ionization and acceleration of C_{60}^{+}. Because the problems encountered in those tests resulted from thermal disintegration of fullerenes and not ionization, the feasiblity of fullerene ion propulsion remains intact. Successful development of fullerene ion thrusters hinges on the identification of the most efficient means of producing positive fullerene ions without introducing high temperature surfaces to the discharge chamber.

References

[1] J. Anderson, D. Fitzgerald, "Experimental Investigation of Fullerene Propellant for Ion Propulsion," **IEPC-93-033**, Seattle, Washington, September, (1993).

[2] Hruby V., Martinez-Sanchez M., Bates S., Lorents D., "A High Thrust Density, C_{60} Cluster Ion Thruster," *25th AIAA Plasmadynamics and Lasers Conference* **AIAA 94-2466**, Colorado Springs, Colorado, June, (1994).

[3] H. Takegahara, Y. Nakayama, "C_{60} Molecule as a Propellant for Electric Propulsion," *23rd International Electric Propulsion Conference* **IEPC-93-032**, Seattle, Washington, September (1993).

[4] S. O'Brien, J. Heath, R. Curl, and R. Smalley, " Photophysics of Buckminsterfullerene and Other Carbon Cluster Ions," *Journal of Chemical Physics* **88**, 220 (1988).

[5] P. Horak and U. Gibson, "Broad Fullerene-Ion Beam Generation and Bombardment Effects," *Applied Physics Letters* **65(8)**, 968 (1994).

[6] D. Yu, L. Andersen, C. Brink, and P. Hvelplund, "Formation and Fragmentation of C_n^+ Clusters Produced from a C_{60}/C_{60} Mixture in an Electron-Impact Ion Source," *Zeitschrift fur Physik D* **29**, 53 (1994).

[7] D. Gruen, S. Liu, A. Krauss, and X. Pan, "Buckyball Microwave Plasmas: Fragmentation and Diamond Film Growth," *Journal of Applied Physics* **75(3)**, 1758 (1994).

[8] N. Sato, T Mieno, T. Hirata, Y. Yagi, R. Hatakeyama, and S. Iizuka, "Production of C_{60} Plasma," *Physics of Plasmas* **1(10)**, 3480 (1994).

[9] A. Hamza, M. Balooch, and M. Moalem, "Growth of Silicon Carbide Films Via C_{60} Precursors," *Surface Science* **317(3)**, L1129 (1994).

[10] J. Moore, C. Davis, and M. Coplan, "Building Scientific Apparatus," Addison-Wesley Publishing Company, Inc., 333 (1989).

[11] John R. Anderson, Jet Propulsion Laboratory, Personal Communication, (1995).

[12] M. Lezius, P. Scheier, M. Foltin, B. Dünser, T. Rauth, V. Akimov, W. Krätschmer, and T. Märk, "Interaction of Free Electrons with C_{60}: Ionization and Attachment Reactions," *International Journal of Mass Spectrometry and Ion Processes* **129**, 49 (1993).

[13] M. Lezius, P. Scheier, and T. Märk, "Free Electron Attachment to C_{60} and C_{70}," *Chemical Physics Letters* **203(2,3)**, 232 (1993).

[14] T. Jaffke, E. Illenberger, M. Lezius, S. Matejcik, D. Smith, and T. Märk, "Formation of C_{60}^- and C_{70}^- by Free Electron Capture. Activation Energy and Effect of the Internal Energy on Lifetime," *Chemical Physics Letters* **226**, 213 (1994).

[15] M. Sai Baba, T. Narasimhan, R. Balasubramanian, and C. Mathews, a) "Appearance Potential and Electron Impact Ionisation Cross-Section of C_{60}," *International Journal of Mass Spectrometry and Ion Processes* **114**, R1 (1992).

[16] D. Rapp and P. Englander-Golden, "Total Cross Sections for Ionization and Attachment in Gases by Electron Impact," *Journal of Chemical Physics* **43(5)**, 1464 (1965).

Chapter 7

Summary and Conclusions

7.1 Review of Results and Conclusions

The purpose of this research has been to study those properties of fullerene molecules that may impact the feasibility of their use as an ion thruster propellant. While some limitations have been identified, most of the findings of this research indicate that no fundamental barriers exist to the development of a C_{60} ion thruster. There are two fundamental requirements for the development of this thruster: (1) a narrow operating temperature range must be observed to avoid thermal decomposition of the molecules and to prevent fullerene condensation, and (2) a continuous supply of primary electrons must be introduced to or produced in the plasma for positive C_{60} ion production to be sustained.

Although filament cathode plasma sources have produced fullerene ions beams, the devices ultimately failed because of cathode damage [1,2]. Also, amorphous and graphitic carbon residue was found in both the effusive cells which provided the fullerene vapor and the discharge chambers. These findings prompted an investigation of fullerene thermal stability.

Fullerene thermal decomposition was studied by heating powdered C_{60}/C_{70} samples *in vacuo* to temperatures between 873 and 1273 K. The treated samples were dissolved in various solvents and examined by UV-visible absorption spectroscopy. By fitting the decay curves of fullerene concentration to an exponential function, decay constants were obtained and used for an Arrhenius plot. It was found that the activation energy for thermal disintegration of C_{60} is significantly lower than that predicted by molecular dynamics simulations. Thus, the first requirement stated above was established.

The second requirement was determined by performing experiments with an RF plasma. The RF plasma research was initiated to avoid the presence of high temperature surfaces. Though a plasma could be sustained with a mixture of xenon and C_{60}, it was quenched when the ratio of fullerene to xenon number density exceeded 1:16. It is believed that this occurred because the fullerene negative ion production rate exceeded that of positive ions at low electron energy. However, the filament cathode plasma sources successfully sustained fullerene discharges because a steady supply of primary electrons was provided.

Careful storage and treatment of C_{60} will be necessary to assure its purity. It does tenaciously hold solvents and adsorb gases. However, the affinity of C_{60} for CO_2 is not nearly so large as had been anticipated from early infrared spectral evidence [3]. This conclusion was reached by examining infrared spectra of fullerene in solution as well as the solid state. Features that had been attributed to CO_2 stretch vibrations were shown to result from combination modes of C_{60}. Deliberate adsorption of CO_2 on C_{60} showed new features at different wavenumbers than the combination modes. The reason for the relatively high intensity of many combination and silent modes of C_{60} remains a mystery.

Samples enriched with ^{13}C have shown that symmetry lowering by isotopic substitution is not the cause [4,5]. Despite the orientational disorder in solid C_{60}, crystal field effects remain the primary candidate.

Electron impact ionization experiments conducted with a time-of-flight mass spectrometer demonstrated that fullerenes possess a high resistance to collisionally induced fragmentation below 40 eV — an energy that would cause dissociation of many other molecules. Although the electron impact ionization experiments reported here were limited in resolution by the energy spread of the electron beam, the appearance potential for single ionization determined for C_{60} agrees well with other reports. Double ionization, even within the uncertainty of these experiments, shows a lower appearance potential than had been reported elsewhere [6]. The ionization cross section curve for C_{60}^{+} is similar to that seen in other published studies, and shows that peak ionization occurs at lower electron energies than are typically found for atomic species. This probably occurs because fragmentation processes appear at the higher electron energies.

7.2 Recommendations for Future Work

Some of the properties of fullerene molecules that affect ion thruster performance have not been addressed here. One of these is the total inelastic collision cross section of C_{60}. Inelastic collisions resulting in excitation of C_{60} lead to unrecoverable losses in a plasma discharge. There have been several investigations of fullerenes by electron energy loss spectroscopy [7]-[11], but the total, integrated inelastic collision cross section has not been reported.

Studies of sputter erosion by fullerene ion bombardment are critical to determine potential thruster life limitations. There is the possibility that fullerene ions will demonstrate reduced erosion rates compared to that caused by xenon ion bombardment. This suggestion stems from the observation that fullerene ions colliding with surfaces deposit only a fraction of their incident kinetic energy in the surface, while the remainder is distributed among recoil and internal vibrational modes of the fullerene molecules [12]. However, sputter erosion resulting from bombardment by C_2 fragments could pose a serious problem.

For the successful implementation of a fullerene ion thruster, several key engineering issues must be addressed. The first of these is the ionization mechanism. Use of cold cathode sources or photoionization techniques are plausible. A noble gas hollow cathode system physically isolated from the discharge chamber may also be an alternative.

In the ion engines constructed to test fullerene ion production and acceleration, the propellant was introduced to the discharge chamber as a vapor following sublimation from an effusive cell affixed to the discharge chamber. This method is impractical for long-duration fullerene ion engine tests because of the limited propellant storage volume in the effusive cell. A more practical method for introducing C_{60} propellant into the thruster is necessary.

The issue of fullerene ion beam neutralization also has not been adequately addressed. Use of a noble gas neutralizer cathode assembly may be required. Alternatively, beam neutralization may be achieved through the use of field emission cathodes.

The discovery of the fullerenes and other large covalently bonded carbon nanostructures has led to an exciting new branch of chemistry that will undoubtably result in myriad applications. When commercially viable applications of fullerenes do emerge, C_{60} production could easily be scaled up to produce large quatities of the material inexpensively. Whether the most successful applications of fullerenes are as pharmaceuticals, semiconductors, superconductors, or ion engine propellants, there are still innumerable studies to be made of their physical and chemical properties. Buckyballs are full of surprises.

References

[1] J. Anderson, D. Fitzgerald, "Experimental Investigation of Fullerene Propellant for Ion Propulsion," **IEPC-93-033**, Seattle, Washington, September (1993).

[2] V. Hruby, M. Martinez-Sanchez, S. Bates, D. Lorents, "A High Thrust Density, C_{60} Cluster Ion Thruster," *25th AIAA Plasmadynamics and Lasers Conference* **AIAA 94-2466**, Colorado Springs, Colorado, June, (1994).

[3] S. Leifer and M. Anderson, "Fourier Transform Infrared Spectral Studies of C_{60}: Combination Modes and Contamination Features Resolved," *Submitted to Physical Review B*, April (1995).

[4] M. Martin, J. Fabian, J. Godard, P. Bernier, J.M. Lambert, and L. Mihaly, "Vibrational Study of ^{13}C-Enriched C_{60} Crystals, " *Physical Review B* **51(5)**, 2844 (1995).

[5] A. Rosenberg and C. Kendziora, "Effect of ^{13}C Isotopic Substitution on the Raman Spectrum of C_{60}," *Physcial Review B* **51(14)**, 9321 (1995).

[6] S. Srivastava, G. Jong, S.D. Leifer, and W.A. Saunders, "Ionization of C_{60} (Buckminsterfullerene) by Electron Impact," *Rapid Communications in Mass Spectrometry* **7**, 610 (1993).

[7] S. Wang, S. Trajmar, and M. Khakoo, "Low Energy Electron-Impact Spectroscopy of C_{60} Buckminsterfullerene Molecule," *Journal of Physics B* **26(20)**, 3639 (1993).

[8] P. Hansen, P. Fallon, and W. Krätschmer, "An EELS Study of Fullerite – C_{60}/C_{70}," *Chemical Physics Letters* **181(4)**, 367 (1991).

[9] H. Cohen, E. Kolodney, T. Maniv, and M. Folman, "A Comparative Reflection Electron Energy Loss Study of C_{60} and Graphite," *Solid State Communications* **81(2)**, 183 (1992).

[10] J. Keller and M. Coplan, "Electron Energy Loss Spectroscopy of C_{60}," *Chemical Physics Letters* **193(1-3)**, 89 (1992).

[11] R. Kuzuo, M. Terauchi, M. Tanaka, Y. Saito, and H. Shinohara, "High-Resolution Electron Energy-Loss Spectra of Solid C_{60}," *Japanese Journal of Applied Physics* **30(10B)**, L1817 (1991).

[12] R. Beck, P. St. John, M. Alvarez, F. Diederich, and R. Whetten, "Resilience of All-Carbon Molecules C_{60}, C_{70}, and C_{84}: A Surface Scattering Time-of-Flight Investigation," *Journal of Physical Chemistry* **95(21)**, 8402 (1991).

Appendix A

Thermal Decomposition Data

The following data were taken to deduce the thermal stability of fullerenes C_{60} and C_{70}. The 'Mass' column indicates the mass of the fullerene sample placed in the quartz ampoule, and 'Composition' indicates whether the sample was pure C_{60}, pure C_{70}, or mixed fullerenes. The temperature and duration for which the vacuum-sealed ampoules were heated in the furnace are written in the 'Temperature' and 'Time' columns, respectively. The solvent used and peaks monitored are shown in the 'Solvent' and 'Peak' columns. The amount of remaining fullerene detected is shown in the column labeled A cc/mg for absorbance·volume/sample mass.

Trial	Mass(mg)	Composition	Temperature(K)	Time(min)	Solvent	peak(nm)	A cc/mg
5-15-94							
1	9.5	C_{60}/C_{70}	—	—	330/270		219
2	13.0	C_{60}/C_{70}	1073	360	CH_2Cl_2	330/270	21.5/70.7
3	10.0	C_{60}/C_{70}	1073	180	CH_2Cl_2	330/270	32.0/110.0
4	10.5	C_{60}/C_{70}	1073	60	CH_2Cl_2	330/270	45.7/156.0
5	13.4	C_{60}/C_{70}	1073	20	CH_2Cl_2	330/270	61.2/213.0
5-16							
1	11.1	C_{60}/C_{70}			CH_2Cl_2	270	128
2	11.6	C_{60}/C_{70}			CH_2Cl_2	270	143
3	11.0	C_{60}/C_{70}	—	—	CH_2Cl_2	270	127
4	10.4	C_{60}/C_{70}	—	—	CH_2Cl_2	270	111
5	10.8	C_{60}/C_{70}			$C_6H_5CH_3$	330	66.6
5-17 no.1							
1	11.2	C_{60}/C_{70}, He	—	—	$C_6H_5CH_3$	330	75.0
2	9.2	C_{60}/C_{70}, He	1073	180	$C_6H_5CH_3$	330	30.4
3	10.6	C_{60}/C_{70}, He	1073	60	$C_6H_5CH_3$	330	40.0
4	8.3	C_{60}/C_{70}, He	1073	20	$C_6H_5CH_3$	330	53.0
5	8.8	C_{60}/C_{70}, He	1073	360	$C_6H_5CH_3$	330	15.9
5-17 no.2							
1	9.4	C_{60}/C_{70}, He	1473	180	$C_6H_5CH_3$	—	—
2	9.1	C_{60}/C_{70}, He	1473	360	$C_6H_5CH_3$	—	—
3	13.3	C_{60}/C_{70}, He	1473	20	$C_6H_5CH_3$	—	—
4	11.2	C_{60}/C_{70}, He	1473	60	$C_6H_5CH_3$	—	—
5	10.9	C_{60}/C_{70}, He	—	—	$C_6H_5CH_3$	—	—
5-19							
2	9.0	C_{60}	—	—	CH_2Cl_2	330	64.4
3	10.1	C_{60}	—	—	$C_6H_5CH_3$	330	71.3

Table A.1: Fullerene samples prepared for material compatibility and thermal stability tests

Trial	Mass(mg)	Composition	Temperature(K)	Time(min)	Solvent	peak(nm)	A cc/mg
5-20							
1	8.1	C_{70}	—	—	CH_2Cl_2	380	212.3
2	8.6	C_{70}	—	—	CH_2Cl_2	380	148.8
3	9.5	C_{70}	—	—	CH_2Cl_2	380	138.9
4a	10.4	C_{70}	1073	180	CH_2Cl_2	380	125
5	9.5	C_{70}	1073	360	CH_2Cl_2	380	105
5-24							
1	9.8	C_{60}/C_{70}, M	1073	60	CH_2Cl_2	270	165
2	11.2	C_{60}/C_{70}, Ta	1073	60	CH_2Cl_2	—	—
3	10.5	C_{60}/C_{70}, W	1073	60	CH_2Cl_2	270	78.1
4	11.3	C_{60}/C_{70}, SS	1073	60	CH_2Cl_2	270	95.6
5	9.9	C_{60}/C_{70}	1073	60	CH_2Cl_2	270	107.1
5-25 no.1							
1	11.6	C_{60}/C_{70}, SS	1273	60	$C_6H_5CH_3$		
2	12.0	C_{60}/C_{70}, SS	873	120	$C_6H_5CH_3$	330	72.6
5-25 no.2							
1	9.6	C_{60}/C_{70}	—	—	$C_6H_5CH_3$	—	—
2	9.9	C_{60}/C_{70}	1273	60	$C_6H_5CH_3$		77.1
3	9.7	C_{60}/C_{70}	—	—	$C_6H_5CH_3$		74.7
4	10.5	C_{60}/C_{70}	873	60	$C_6H_5CH_3$		76.3
5	9.5	C_{60}/C_{70}	—	—	$C_6H_5CH_3$	see below	
5-27							
1	14.6	C_{60}/C_{70}	untreated	—	CH_2Cl_2	270	156
5-25 #5							
1	9.5	C_{60}/C_{70}	—	—	$C_6H_5CH_3$		80.6
2	9.5	C_{60}/C_{70}	—	—	$C_6H_5CH_3$		83.0
3	9.5	C_{60}/C_{70}	—	—	$C_6H_5CH_3$		80.6
4	9.5	C_{60}/C_{70}	—	—	$C_6H_5CH_3$		75.7
5	9.5	C_{60}/C_{70}	—	—	$C_6H_5CH_3$		75.7
6	9.5	C_{60}/C_{70}	—	—	$C_6H_5CH_3$		80.6

Fullerene samples prepared for material compatibility and thermal stability tests

Trial	Mass(mg)	Composition	Temperature(K)	Time(min)	Solvent	peak(nm)	A cc/mg
6-7 no.1							
1	9.9	C_{60}/C_{70}	—	—	$C_6H_5CH_3$	330	75.7
2	10.8	C_{60}/C_{70}	1073	20	$C_6H_5CH_3$	330	61.1
3	9.1	C_{60}/C_{70}	1073	60	$C_6H_5CH_3$	330	44.2
4	9.7	C_{60}/C_{70}	1073	180	$C_6H_5CH_3$	330	39.2
5	9.6	C_{60}/C_{70}	1173	60	$C_6H_5CH_3$	330	8.2
6-7 no. 2							
4	9.2	C_{60}/C_{70}	973	60	$C_6H_5CH_3$		77.0
5	9.8	C_{60}/C_{70}	873	360	$C_6H_5CH_3$		80.1
6-7 no. 3							
2	10.2	C_{60}/C_{70}	1173	5	$C_6H_5CH_3$	330	41.5
3	9.7	C_{60}/C_{70}	1173	10	$C_6H_5CH_3$	330	14.9

Fullerene samples prepared for material compatibility and thermal stability tests

Appendix B

Infrared Spectra of Fullerenes

The following data are the spectra and peak locations of all features in the vibrational spectrum of C_{60} and C_{70}. All data are given in wavenumbers (cm^{-1}). The pure C_{60} was obtained from the Department of Chemistry of the University of Southern California at Los Los Angeles. Term, LTD. supplied the pure C_{70}. For diffuse reflectance Fourier transform infrared measurements of powder samples from 4000 to 550 cm^{-1}, an Analect Rfx-40 FTIR spectrometer with a MCT (Hg-Cd-Te) LN cooled detector was used. The spectrometer was equiped with a biconical diffuse reflectance accessory. The 4.0 cm^{-1} resolution spectra were collected with 256 coadded scans relative to a powdered KBr standard.

This Study	Ref. A	Ref. A	Ref. B	This Study	Ref. A	Ref. A	Ref. B
	(theory)	(experiment)			(theory)	(experiment)	
577	575.8	575.8	575	1182	1182.9	1182.9	1182
613			609	1213	1207.5	1213.3	1214
656			668	1242	1243.0	1242.2	1242
692				1269			1260
700				1308	1303.0	1306.8	1308
713	711.0	712.1	712	1375	1369.0	1375.2	1376
727			739	1387	1381.0	1375.2	1394
771		770.9	775	1429	1429.2	1429.2	1429
804	799.0	808.5	796	1462	1458.5	1462.0	1470
825	828.5	822.9	827	1495	1490.5	1495.7	1497
899	909.0	907.8	911	1539	1538.5	1538.1	1539
962	963.5	961.7		1560			1563
1028	1020.5	1015.7	1020	1572	1566.0	1570.1	1572
1043			1039	1608	1607.0	1607.5	1612
1080			1080	1653			
1101	1101.0	1099.6	1100	1670			1671
1165	1166.0	1164.1	1168				

Table B.1: Peak locations in the C_{60} infrared spectrum. Data are given in wavenumbers (cm^{-1}). The references are A) K.A. Wang, A.M. Rao, P.C. Eklund, M.S. Dresselhaus, and G. Dresselhaus, *Physical Review B* **48(5)**, 11375 (1993), and B) M. Martin, X. Du, J. Kwon, and L. Mihaly, *Physical Review B* **50(1)**, 173 (1994).

This Study	Ref. A (theory)	Ref. A (experiment)	Ref. B
1701			
1718	1727.4		1720
1734			
1747	1745.0	1746.3	1747
1780	1781.0	1779.1	1782
1792	1789.0	1789.7	1792
1817	1817.5	1815.7	1818
1853	1849.5	1851.4	1854
1874	1871.0	1874.5	1876
1934	1933.3	1934.3	1938
1976	1976.0	1976.7	1979
2015	2012.5	2016.2	2016
2048			2048
2077	2071.0	2075.0	2079
2098	2096.0	2097.2	2099
2121	2120.0	2120.3	2123
2137	2140.2	2134.8	2137
2175	2175.0	2174.3	2176
2191	2191.0	2189.7	2195
2235	2227.5	2234.1	2235
2274	2273.5	2271.7	2275
2291	2287.5	2290.0	2293
2328	2326.0	2326.6	2328
2349	2350.5	2346.8	2350
2389	2385.5	2388.3	2393
2418	2411.0	2417.2	2409
2461	2460.5	2456.7	2462
2526	2530.2	2527.1	2530
2559	2557.0	2558.9	2563
2603			2608
2677	2677.5	2675.5	
2737	2736.5	2735.3	2740
2812	2811.5	2809.5	2814
2848	2855.7	2845.2	

Peak locations in the C_{60} infrared spectrum. Data are given in wavenumbers (cm^{-1}). The references are A) K.A. Wang, A.M. Rao, P.C. Eklund, M.S. Dresselhaus, and G. Dresselhaus, *Physical Review B* **48(5)**, 11375 (1993), and B) M. Martin, X. Du, J. Kwon, and L. Mihaly, *Physical Review B* **50(1)**, 173 (1994).

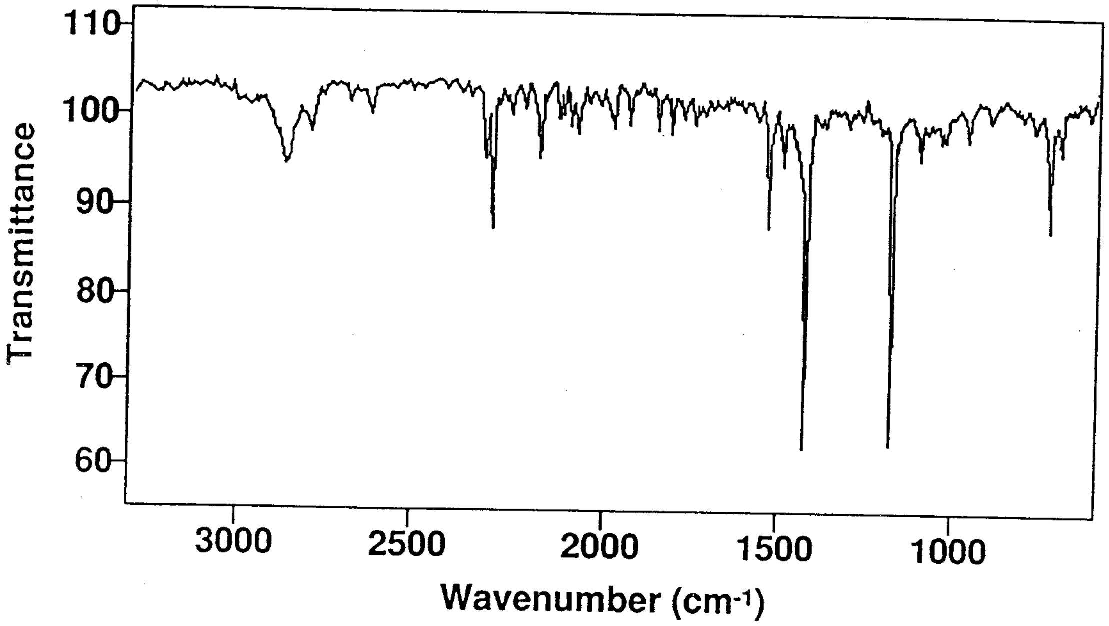

Figure B.1: Diffuse reflectance Fourier transform infrared spectrum of pure C_{60} powder.

C_{70} Infrared Peaks in wavenumbers (cm^{-1})					
577	922	1203	1562	1923	2218
609	931	1217	1585	1965	2237
642	937	1224	1620	1982	2266
675	947	1252	1628	2002	2278
696	976	1277	1639	2015	2306
712	987	1290	1649	2025	2330
727	1001	1321	1689	2040	2343
739	1014	1373	1711	2052	2395
766	1032	1383	1720	2081	2414
795	1061	1415	1739	2089	2432
812	1070	1433	1757	2098	2657
835	1086	1462	1770	2108	2688
849	1103	1477	1784	2117	2767
868	1134	1489	1805	2141	2798
879	1151	1512	1843	2162	2846
897	1160	1529	1855	2177	2862
904	1176	1533	1871	2193	2918
	1194		1888		2949

Table B.2: Peak locations in the C_{70} infrared spectrum. Data are given in wavenumbers (cm^{-1}).

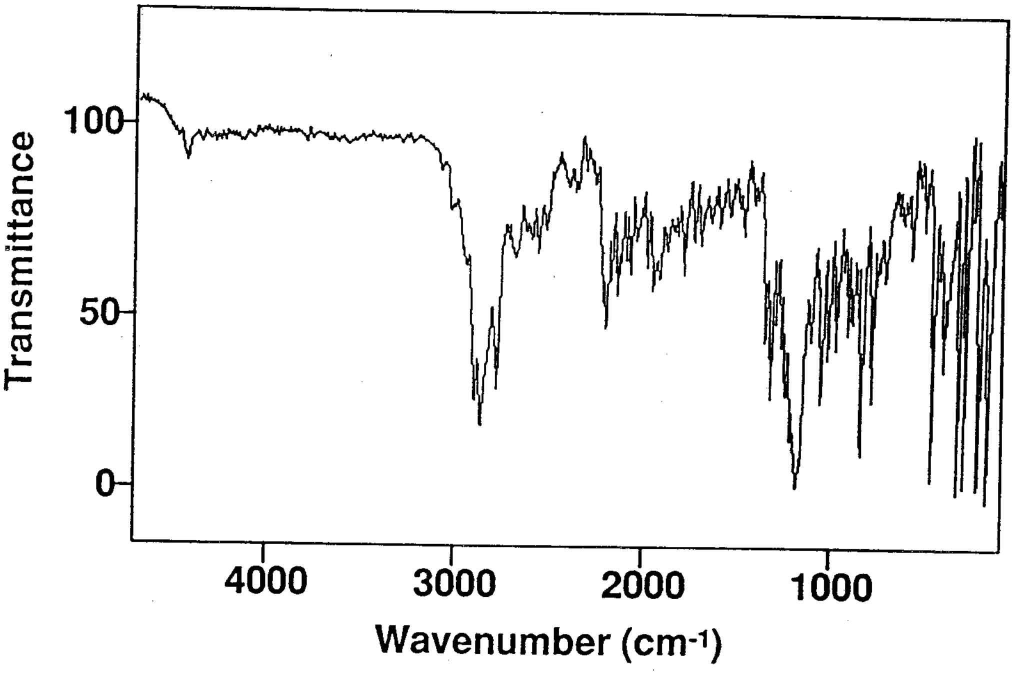

Figure B.2: Diffuse reflectance Fourier transform infrared spectrum of pure C_{70} powder.

I_h	A_g	F_{1g}	F_{2g}	G_g	H_g	A_u	F_{1u}	F_{2u}	G_u	H_u
A_g	A_g	F_{1g}	F_{2g}	G_g	H_g	A_u	F_{1u}	F_{2u}	G_u	H_u
F_{1g}	F_{1g}	$H_g+A_g+F_{1g}$	G_g+H_g	$G_g+H_g+F_{2g}$	$G_g+H_g+F_{1g}$ $+F_{2g}$	F_{1u}	$A_u+H_u+F_{1u}$	H_u+G_u	$H_u+G_u+F_{2g}$	$H_u+G_u+F_{1u}$ $+F_{2u}$
F_{2g}	F_{2g}	G_g+H_g	$A_g+H_g+F_{2g}$	$G_g+H_g+F_{1g}$	$G_g+H_g+F_{1g}$ $+F_{2g}$	F_{2u}	H_u+G_u	$A_u+H_u+F_{2u}$	$G_u+H_u+F_{1u}$	$H_u+G_u+F_{1u}$ $+F_{2u}$
G_g	G_g	$H_g+G_g+F_{2g}$	$H_g+G_g+F_{1g}$	$A_g+F_{1g}+F_{2g}$ $+G_g+H_g$	$G_g+2H_g+F_{1g}$ $+F_{2g}$	G_u	$H_u+G_u+F_{2u}$	$H_u+G_u+F_{1u}$	$A_u+G_u+H_u$ $+F_{1u}+F_{2u}$	$G_u+2H_u+F_{1u}$ $+F_{2u}$
H_g	H_g	$H_g+G_g+F_{1g}$ $+F_{2g}$	$H_g+G_g+F_{1g}$ $+F_{2g}$	$G_g+2H_g+F_{1g}$ $+F_{2g}$	$A_g+2G_g+2H_g$ $+F_{1g}+F_{2g}$	H_u	$H_u+G_u+F_{1u}$ $+F_{2u}$	$H_u+G_u+F_{1u}$ $+F_{2u}$	$G_u+2H_u+F_{1u}$ $+F_{2u}$	$A_u+2G_u+2H_u$ $+F_{1u}+F_{2u}$
A_u	A_u	F_{1u}	F_{2u}	G_u	H_u	A_g	F_{1g}	F_{2g}	G_g	H_g
F_{1u}	F_{1u}	$A_u+H_u+F_{1u}$	H_u+G_u	$H_u+G_u+F_{2u}$	$H_u+G_u+F_{1u}$ $+F_{2u}$	F_{1g}	$A_g+H_g+F_{1g}$	G_g+H_g	$H_g+G_g+F_{2g}$	$G_g+H_g+F_{1g}$ $+F_{2g}$
F_{2u}	F_{2u}	H_u+G_u	$A_u+H_u+F_{2u}$	$H_u+G_u+F_{1u}$	$H_u+G_u+F_{1u}$ $+F_{2u}$	F_{2g}	G_g+H_g	$A_g+H_g+F_{2g}$	$H_g+G_g+F_{1g}$	$H_g+G_g+F_{1g}$ $+F_{2g}$
G_u	G_u	$G_u+H_u+F_{2g}$	$G_u+H_u+F_{1u}$	$A_u+G_u+H_u$ $+F_{1u}+F_{2u}$	$G_u+2H_u+F_{1u}$ $+F_{2u}$	G_g	$H_g+G_g+F_{2g}$	$G_g+H_g+F_{1g}$	$A_g+H_g+G_g$ $+F_{1g}+F_{2g}$	$G_g+2\mathrm{Hg}+F_{1g}$ $+F_{2g}$
H_u	H_u	$G_u+H_u+F_{1u}$ $+F_{2u}$	$G_u+H_u+F_{1u}$ $+F_{2u}$	$G_u+2H_u+F_{1u}$ $+F_{2u}$	$A_u+2G_u+2H_u$ $+F_{1u}+F_{2u}$	H_g	$H_g+G_g+F_{1g}$ $+F_{2g}$	$H_g+G_g+F_{1g}$ $+F_{2g}$	$G_g+2H_g+F_{1g}$ $+F_{2g}$	$A_g+2G_g+2H_g$ $+F_{1g}+F_{2g}$

Table B.3: Direct product table for the icosahedral group, I_h.

Appendix C

Polarizability of C_{60}

C.1 Introduction

There have been several reports of the polarizability of C_{60} determined by both experimental [1]-[4] and theoretical [4]-[9] methods. These values are summarized in Table C.1.

In attempts to predict the ionization cross section of C_{60}, one method applied was to correlate the polarizability of the molecule with cross section. Because some variation existed between reported values, experiments to determine the polarizability of C_{60} were performed.

C.2 Polarizability Determination

Experiment

The measurement technique involved observing interference fringes formed in a Mach-Zehnder interferometer when one of the light paths intersected a cuvette containing a C_{60} solution. Toluene was used as the solvent for pure C_{60} obtained from MER Corporation.

By varying the concentration of C_{60} in the cuvette, a shift of fringes could be observed. The light source was a Helium-Neon laser (632 *nm*). The source wavelength is just above an absorption peak of C_{60}, hence the imaginary part of the index of refraction was negligible, ensuring an accurate determination of the dielectric constant. The interference fringes were focused on a photodiode. Output from the photodiode was routed to a lock-in amplifier. A reference signal to the lock-in amplifier was provided by a chopper positioned in front of the laser source.

The number of fringes F observed corresponds to the index of refraction of the C_{60} by:

$$n_{final} = n_{initial} + F\frac{\lambda_0}{d} \tag{C.1}$$

where d is the path length through the cuvette (1.0 cm), λ_0 is the source wavelength, and $n_{initial}$ and n_{final} are the initial and final indices of refraction of the C_{60} solution, respectively.

The Clausius-Mossotti relation was then used to relate the determined dielectric constant to the polarizability of C_{60}:

$$\frac{(n^2-1)}{(n^2+2)} = \frac{4\pi}{3}\sum_i \alpha_i N_i. \tag{C.2}$$

Here, n is the index of refraction, and α_i and N_i are the polarizability and number density of the ith component respectively. Rearranging Equation C.2 and letting $\alpha_i N_i = z_i$ yields

$$n = \sqrt{\frac{3+8\pi\sum_i z_i}{3-4\pi\sum_i z_i}}. \tag{C.3}$$

The Clausius-Mossotti relation is only valid in solids that possess crystal structures which satisfy the Lorentz relation [10]

$$E_{local} = E + \frac{1}{3\varepsilon_0}P, \tag{C.4}$$

where E_{local} is the total local field at a cubic site, E is the macroscopic field acting on a particle in a cubic site, and P is the polarization. This relation is satisfied by anisotripic media as well as cubic crystals. Because of the coexisting hexagonal-closest-packed and face-centered-cubic phases of fullerene crystals and the large number of crystal defects that are found in van der Waals crystals, it was believed that the experiment would yield more reliable data if performed with C_{60} dissolved in a liquid. Gas-phase polarizability measurements may be even more accurate, but are difficult to perform because of the high temperatures required to obtain a dense vapor.

Results

There was a large spread in the data taken by the method described above. This spread resulted from the technique being sensitive to changes in various conditions. First, evaporation of solvent from the cuvette was not prevented for the duration of each trial which lasted 25 minutes. Second, vibrations in components of the apparatus sometimes caused an unitentional fringe shift. The vibrations were caused by a motor-driven stirrer which was used to insure uniform concentration.

Figure C.1 shows interference fringe data from a trial of this experiment. The averaged data yield a C_{60} polarizability of $85.8 \pm 11.6 \times 10^{-24}\text{cm}^3$.

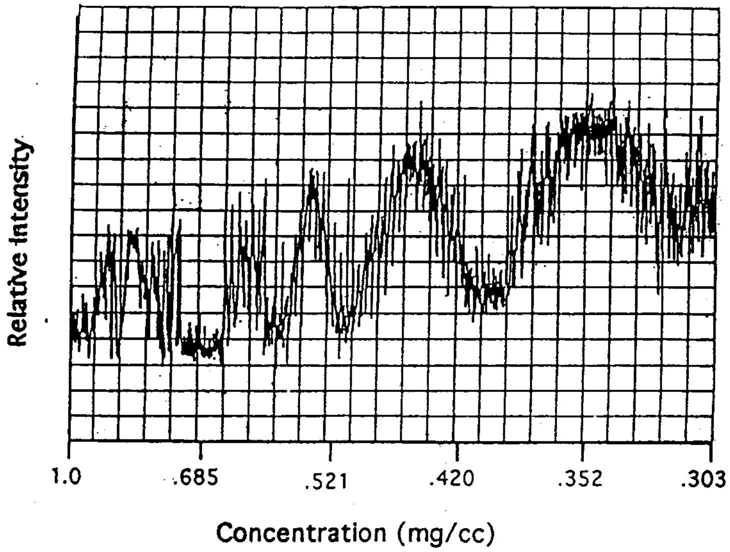

Figure C.1: Interference fringe shift resulting from a change in C_{60} solution concentration.

Experimental		Theoretical	
Reference	Polarizability ($\times 10^{-24}$ cm^3)	Reference	Polarizability ($\times 10^{-24}$ cm^3)
[1]	79.0	[9]	60.75
[2]	77.3	[7]	390
[3]	83.5	[6]	78.8
[4, and references therein]	84.9	[8]	79.5
This work	85.8±11.6	[5]	65.5
		[4]	82.7

Table C.1: Theoretically and experimentally determined polarizability of C_{60}. The experimental values are derived from measured optical constants and the Clausius-Mossotti relation. A density of 1.68 g/cc was used for solid C_{60}.

References

[1] S.L. Ren, Y. Wang, A.M. Rao, E. McRae, J.M. Holden, T. Hager, K. Wang, W. Lee, H.F. Ni, J. Selegue, and P.C. Eklund, "Ellipsometric Determination of the Optical Constants of C_{60} (Buckminsterfullerene) Films," *Applied Physics Letters* **59(21)**, 2678 (1991).

[2] G. Guizzetti, F. Marabelli, M. Patrini, V. Capozzi, G.F. Lorusso, A. Minafra, M. Manfredini, and P. Milani,"Optical Properties of Fullerite Thin Films in the 0.4 to 32 eV Energy Range," *Physica Status Solidi (b)* **183**, 267 (1994).

[3] A. Hebard, R. Haddon, R. Fleming, and A. Korton, "Deposition and Characterization of Fullerene Films," *Applied Physics Letters* **59(17)**, 2109 (1991).

[4] A. Quong and M. Pederson, "Density-Functional-Based Linear and Nonlinear Polarizabilities of Fullerene and Benzene Molecules," *Physical Review B* **46(19)**, 12906 (1992).

[5] P. Fowler, P. Lazzeretti, and R. Zanasi, "Electric and Magnetic Properties of the Aromatic Sixty-Carbon Cage," *Chemical Physics Letters* **165**, 79 (1990).

[6] H. Weiss, R. Ahlrichs, and M. Häser, "A Direct Algorithm for Self-Consistent-Field Linear Response Theory and Application to C_{60}: Excitation Energies, Oscillator Strengths,

and Frequency-Dependent Polarizabilites," *Journal of Chemical Physics* **99(2)**, 1262 (1993).

[7] R. Knize, "Polarizability of a Free Electron Gas Confined to a Spherical Shell," *Optics Communications* **106**, 95 (1994).

[8] D. Östling, P. Apell, and A. Rosén, "Theory for Collective Resonances of the C_{60} Molecules," *Europhysics Letters* **21(5)**, 539 (1993).

[9] B. Shanker and J. Applequist, "Polarizabilities of Fullerenes C_{20} Through C_{240} from Atom Monopole-Dipole Interaction Theory," *Journal of Physical Chemistry* **98**, 6486 (1994).

[10] C. Kittel, "Introduction to Solid State Physics," Sixth Edition, 368, John Wiley and Sons, Inc., New York (1986).